



Deposited via The University of Leeds.

White Rose Research Online URL for this paper:

<https://eprints.whiterose.ac.uk/id/eprint/207036/>

Version: Accepted Version

Article:

Wheeler, J., Piazzolo, S., Prior, D.J. et al. (2023) Using crystal-lattice distortion data for geological investigations: the weighted Burgers vector method. *Journal of Structural Geology*, 179. 105040. ISSN: 0191-8141

<https://doi.org/10.1016/j.jsg.2023.105040>

© 2023 Elsevier Ltd. This manuscript version is made available under the CC-BY-NC-ND 4.0 license <http://creativecommons.org/licenses/by-nc-nd/4.0/>. This is an author produced version of an article, published in the *Journal of Structural Geology*. Uploaded in accordance with the publisher's self-archiving policy.

Reuse

This article is distributed under the terms of the Creative Commons Attribution-NonCommercial-NoDerivs (CC BY-NC-ND) licence. This licence only allows you to download this work and share it with others as long as you credit the authors, but you can't change the article in any way or use it commercially. More information and the full terms of the licence here: <https://creativecommons.org/licenses/>

Takedown

If you consider content in White Rose Research Online to be in breach of UK law, please notify us by emailing eprints@whiterose.ac.uk including the URL of the record and the reason for the withdrawal request.

Journal of Structural Geology

Using crystal-lattice distortion data for geological investigations: the weighted Burgers vector method --Manuscript Draft--

Manuscript Number:	SG-D-22-00329R2
Article Type:	Original article
Keywords:	Electron backscatter diffraction; Geometrically Necessary Dislocations; slip systems; Intracrystalline Distortion; Weighted Burgers Vector
Corresponding Author:	John Wheeler, PhD University of Liverpool UNITED KINGDOM
First Author:	John Wheeler, PhD
Order of Authors:	John Wheeler, PhD Sandra Piazzolo, PhD David J Prior, PhD Patrick W Trimby, PhD Jacob A Tielke
Abstract:	<p>Distorted crystals carry useful information on processes involved in their formation, deformation and growth. The distortions are accommodated by geometrically necessary dislocations, and therefore characterising those dislocations is an informative task, to assist in, for example, deducing the slip systems that produced the dislocations. Electron backscatter diffraction (EBSD) allows detailed quantification of distorted crystals and we summarise here a method for extracting information on dislocations from such data. The weighted Burgers vector (WBV) method calculates a vector at each point on an EBSD map, or an average over a region. The vector is a weighted average of the Burgers vectors of dislocation lines intersecting the map surface. It is weighted towards dislocation lines at a high angle to the map but that can be accounted for in interpretation. The method is fast and does not involve specific assumptions about dislocation types; it assumes only that elastic strains have little effect on the calculation. It can be used, with care, to analyse subgrain walls (sharp orientation changes) as well as gradational orientation changes within individual grains. There are four linked parts to this contribution.</p> <p>We describe the mathematical background to the WBV and then how it is modified to deal with spaced, discrete orientation measurements.</p> <p>EBSD orientation data have angular errors, and so does the WBV. We present a new analysis of these angular errors, showing there is a trade-off between directional accuracy and area sampled. Angular errors can now be accounted for during testing of hypotheses about dislocation types.</p> <p>We present new studies on olivine and plagioclase to illustrate how to use the method.</p> <p>We discuss published studies on ice and titanite to further illustrate the method.</p> <p>We note that the methods discussed here are applicable to any crystalline material</p>

	encompassing minerals (including ice), metals and ceramics.
Suggested Reviewers:	<p>Manish A Mamtani Professor, Indian Institute of Technology Kharagpur mamtani@gg.iitkgp.ac.in Reviewed previous version. EBSD + TEM expert</p>
	<p>Elena A Miranda Professor, California State University Northridge elena.miranda@csun.edu EBSD expert</p>
	<p>Virginia Gail Toy Professor, Johannes Gutenberg University Mainz virginia.toy@uni-mainz.de EBSD expert</p>
	<p>Andrew Cross Assistant Scientist, Woods Hole Oceanographic Institution across@whoi.edu EBSD expert</p>
	<p>Luca Menegon Professor, University of Oslo luca.menegon@geo.uio.no EBSD expert</p>
Response to Reviewers:	

- The Weighted Burgers Vector method gives constraints on dislocations in minerals
- It uses EBSD data and makes no prior assumptions about dislocation types
- Angular errors are reduced by analysing larger regions of maps
- Applications to olivine and plagioclase are discussed

Declaration of interests

The authors declare that they have no known competing financial interests or personal relationships that could have appeared to influence the work reported in this paper.

The authors declare the following financial interests/personal relationships which may be considered as potential competing interests:

John Wheeler reports a relationship with Oxford Instruments Nanoanalysis that includes: consulting or advisory. The lead author assisted Oxford Instruments Nanoanalysis with development of a commercial version of the WBV algorithm. This was commercialisation of Intellectual Property developed at University of Liverpool, so OINA paid a sum to UoL. Co-author Trimby facilitated developing the relationship between OINA and UoL. The manuscript comprises ideas developed in collaboration prior to this commercialisation.

Credit author statement

John Wheeler: Conceptualization, Software, Writing - Original Draft, Visualization; **Sandra Piaolo:** Conceptualization, Writing – Review and Editing; **David Prior:** Conceptualization, Writing – Review and Editing; **Patrick Trimby:** Conceptualization, Resources, Writing – Review and Editing; **Jake Tielke:** Resources, Writing – Review and Editing.

Hi Virginia

Many thanks for taking charge of the final stage of review. Our replies bulleted.

I did try to ask the previous reviewers to check what you've done, but they didn't have time, so I did it. I am satisfied that you've addressed most of their recommendations in the revision aside from a few nagging things - which is why I'm requesting minor revisions. I invite you to resubmit your manuscript after addressing my final comments below. Please resubmit your revised manuscript by Feb 03, 2024. And this time please use track changes?

- Thanks for your help, and once again apologies for not tracking changes previously. As well as Editor's suggested edits we made 3 other changes.
- 1. A paper just out confirms and goes beyond our prediction that high angular resolution EBSD data lead to WBV calculations with lower errors, so we cited this on li 789-793.
- 2. We don't include that paper in Table 1 because it opens up a whole new discussion, but we added to the caption to make clear the assumption behind our α_{95} estimates.
- 3. Acknowledged you, including doing more than just the usual editorial role.

Here are your specific suggestions and our responses.

L98. Jiang lacks a year.

- Done

L102-118. Is it possible to more explicitly state that basically you are reconsidering the original WBV idea in context of the ways it has been used, and abused, in the 14 years since your original publication (2009), with the ultimate goal of ensuring that it, and other methods of measuring distortion, are more realistically employed in future studies?

- Rephrased and done. We still need the four subdivisions since reviewers were confused as the aims appeared mixed up.

L124. remove one extra right parenthese

- Done

L210. one reason(s) - delete s.

- Done

L211 'it is convenient to use units of (μm)-1). Could you say 'we recommend using the convenient units of "per-micron"'

- Now 214. Done

Q: Lines 179: **i.e.** "there should be no large orientation variations around the loop" – what would this look like? What is "large"? How would a reader know if they had this problem? A: We cannot provide comprehensive information on misorientations above which boundaries are disorganised; the user must decide.

VT: Yes, but at this stage in the text you say that you will explain later how to recognise or deal with the effect of a large orientation gradient, but I can't really work out where you mean. Why not state here "as explained in Section XXX"?

- new li 232. 228-238 rewritten, hopefully clearer

L275. Half sentence 'In a later section...'. Did you miss something else here or should you just delete these words?

- new 280. Deleted

Q: Line 226: The angle theta should be labeled within Figure 2a—if the sentence calling out 2a mentions theta, this would help integrate the figure with the text. It would be helpful to also label x and y direction in the yellow map surfaces in Figure 2. A: Figure 2 end,

VT: Did you do anything in response to this comment? I can't see changes of this nature to the figure.

- The referee was referring to OLD Fig. 2 now Fig. 3. It wasn't done but is fixed now. Caption modified.

L312-313. You could also say that a disorientation angle “has no absolute sign”?

- Done

Q: L295: “So, although eqn. (4) still applies, it is not particularly helpful”: Equation 4 would have to be evaluated between two points with a finite separation, in which case it's just as helpful as evaluating it around a loop enclosing a finite area (notwithstanding nuances of noise levels), so I'm not sure this sentence is quite right; does it need rephrasing? A: The sentence is correct because in this section it is based on the orientation being a mathematical function of position, and gradients are defined using partial differentiation. We make discussion of spaced measurement points a separate and later section, and such issues are discussed around new Fig. 6.

VT: I think it's useful if you explicitly state which later section this topic is further discussed in.

- New line 365-373 etc. This triggered a rewrite as well as referring forwards to section 2.3.2, and there (li 463) referring back.

L834. ‘Do you mean ‘Crystalscape is for academic use only.’

- We weren't sure if you were suggesting removal of mentioning Aztec Crystal. But we think this should be in there so the reader understands the choices available. Slightly rephrased.

John Wheeler
13 Dec 2023

For submission to Journal of Structural Geology

Using crystal-lattice distortion data for geological investigations: the weighted Burgers vector method

J. Wheeler¹, S. Piazzolo², D. J. Prior³, P. W. Trimby⁴ and J. A. Tielke⁵

¹Department of Earth, Ocean, and Ecological Sciences, University of Liverpool, 4 Brownlow Street, Liverpool, L69 3GP, UK

²University of Leeds, School of Earth & Environment, Leeds LS2 9JT, UK

³Department of Geology, University of Otago, Dunedin, New Zealand

⁴Oxford Instruments Nanoanalysis, High Wycombe, Bucks, England

⁵Lamont-Doherty Earth Observatory of Columbia University, Palisades, NY, USA

Abstract

Distorted crystals carry useful information on processes involved in their formation, deformation and growth. The distortions are accommodated by geometrically necessary dislocations, and therefore characterising those dislocations is an informative task, to assist in, for example, deducing the slip systems that produced the dislocations. Electron backscatter diffraction (EBSD) allows detailed quantification of distorted crystals and we summarise here a method for extracting information on dislocations from such data. The weighted Burgers vector (WBV) method calculates a vector at each point on an EBSD map, or an average over a region. The vector is a weighted average of the Burgers vectors of dislocation lines intersecting the map surface. It is weighted towards dislocation lines at a high angle to the map but that can be accounted for in interpretation. The method is fast and does not involve specific assumptions about dislocation types; it assumes only that elastic strains have little effect on the calculation. It can be used, with care, to analyse subgrain walls (sharp orientation changes) as well as gradational orientation changes within individual grains. There are four linked parts to this contribution.

1. We describe the mathematical background to the WBV and then how it is modified to deal with spaced, discrete orientation measurements.
2. EBSD orientation data have angular errors, and so does the WBV. We present a new analysis of these angular errors, showing there is a trade-off between directional accuracy and area sampled. Angular errors can now be accounted for during testing of hypotheses about dislocation types.
3. We present new studies on olivine and plagioclase to illustrate how to use the method.
4. We discuss published studies on ice and titanite to further illustrate the method.

We note that the methods discussed here are applicable to any crystalline material encompassing minerals (including ice), metals and ceramics.

Keywords

Electron Backscatter Diffraction; Geometrically Necessary Dislocations; Slip Systems; Intracrystalline Distortion; weighted Burgers vector; Olivine; Plagioclase; Ice; Titanite

39 1. Introduction

40 Microstructures are crucial indicators of processes that have affected rocks. Dislocations
41 provide evidence for how and under what conditions individual grains have deformed or they
42 may be growth defects indicating growth conditions. Regardless of their origin dislocations
43 give rise to *distortion* in a crystal lattice on some scale, and we advocate use of this word as a
44 non-genetic description of their geometric effects. If dislocations are due to deformation their
45 Burgers vectors may help constrain the style or conditions of deformation. Individual
46 dislocations give a lattice extra energy, so the density of dislocations is needed to estimate
47 this on a volumetric basis. This plastic strain energy provides a driving force for
48 recrystallization in deformed rocks (Drury & Urai 1990). TEM is the standard method to
49 image individual dislocations, a procedure that can be laborious and will characterise just a
50 tiny fraction of the microstructure, leaving doubts as to how representative it is. In contrast
51 intracrystalline distortions may be optically visible and can be quickly characterised by
52 EBSD mapping over large regions. Such distortions, regardless of cause, must be
53 accommodated by geometrically necessary dislocations (GNDs) (Ashby 1970) and hence
54 give indirect information on dislocation content.

55 The GND concept complements the statistically stored dislocation (SSD) concept. The
56 dislocations involved are not fundamentally different types; instead, these are scale dependent
57 ideas. Lattice curvature over a particular length scale is by definition accommodated by
58 GNDs *at that scale*. Over that length scale there may be other dislocations for example of
59 opposite signs, that cancel out each other's local curvature effects (though still contribute to
60 plastic strain energy and other relevant properties): these are SSDs. Zooming in to a smaller
61 length scale may reveal local lattice curvatures related to what were classified as SSDs. At
62 this smaller length scale some SSDs are now GNDs. If one examines lattice curvature on the
63 atomic scale, all dislocations would be classified as GNDs. In relation to EBSD, the relevant
64 length scale is the step size. So lattice curvature shown on EBSD maps relates to GNDs on
65 the scale of the step size. SSDs will, by definition, not leave a fingerprint on the curvature. A
66 smaller step size will reveal more GNDs. Very small step sizes can reveal individual
67 dislocations (<https://www.ebsd.com/ois-ebsd-system/dislocation-density-analysis>).

68 It would be useful to constrain *directional* (lines, Burgers vectors) and *magnitude* (dislocation
69 density) GND information from EBSD data: examples of approaches follow. If distortion is
70 due to deformation by dislocation motion it can in principle be used to constrain active slip
71 systems (hence deformation conditions) using directional information. Based on geometric
72 assumptions alone, such studies have often focussed on subgrain walls (in essence, localised
73 sharp distortions). For example Lloyd (2002) argues that subgrain walls traces and
74 misorientation axes in quartz can be used to deduce slip systems, though assumptions about
75 "pure" tilt or twist nature of boundaries are needed. Wieser et al. (2020) applied a modified
76 approach to olivine, incorporating subgrain wall traces with information from the method of
77 Wheeler et al. (2009). The latter, the weighted Burgers vector (WBV) method, is what we
78 discuss in this contribution. In minerals with multiple slip systems, distortion cannot be
79 uniquely linked to slip systems using geometry alone. Calculations can then be made
80 assuming that the net dislocation energy is minimised with respect to all possible
81 combinations of dislocation lines and Burgers vectors for example in quartz (Wallis et al.
82 2019b). Distortion magnitudes can be quantified using for example "local misorientation"
83 though the link to actual dislocation densities is not straightforward to make. For example

84 Timms et al. (2012) use local misorientation maps to give an overview of the heterogeneous
85 distortion in shocked zircon crystals.

86 If distortion is due to growth, or is postulated to be, then purely geometric analyses can be
87 applied as they would be to deformed crystals but any extra assumptions must be evaluated
88 with care. Spruzeniece et al. (2017) quantified crystal distortions in KBr-KCl solid solution
89 grown in a stress-free environment: these are due to growth not deformation. Gardner et al.
90 (2021) examined natural distorted albite and showed that some subgrain walls contain
91 dislocations with Burgers vectors with $\langle 010 \rangle$ components. There are no known slip systems
92 with such Burgers vectors, so the subgrain walls were diagnosed as growth defects.

93 The methods in these and many other papers using EBSD to analyse distortions include
94 various assumptions, both in manual processes (e.g. selecting straight segments of boundary
95 traces) and in automatic calculations (e.g. assumptions about allowed slip systems and
96 dislocation energy minimisation). It is generally not clear how errors in EBSD orientation
97 measurements affect deductions: specifically, here we address *angular* errors although
98 *magnitude* errors are relevant (e.g. Jiang et al. (2013)). Some methods are slow if they are
99 manual or compute intensive, a relevant consideration in terms of time versus benefit.
100 Methods using boundary trace analysis cannot be applied to smooth, distributed distortions
101 because there are no discrete boundaries. Overall, the methods to date have diverse strengths
102 and weaknesses.

103 Our overall aim here is to review and extend the WBV method for extracting information on
104 GNDs from EBSD data, based on our experience of how it has been used since first
105 publication in 2009. By clarifying and enhancing the insights it can give we hope to
106 encourage its use in future studies. There are four linked aims.

- 107 1. A description of the theoretical basis based on existing understanding (sections 2.1-
108 2.3) but using new illustrative models. We explain the method using model distorted
109 crystals, with mathematical details in Supplementary Information. We discuss how
110 the method applies to smoothly curved lattices and to subgrain walls (where GNDs
111 are collected into surfaces of negligible width). The aim here is to ensure users of the
112 method understand its advantages and limitations.
- 113 2. New analysis of the errors (specifically angular errors) inherent in the calculation, so
114 that hypotheses about microstructural evolution can be tested robustly (section 2.4).
- 115 3. New examples of application of the method (sections 3.1 olivine and 3.2 plagioclase)
116 to assist in understanding how it works in practice.
- 117 4. Review of implications for previous studies in section 3.5 (Table 1), with some detail
118 in 3.3 ice and 3.4 titanite.

119 Finally, we discuss this method in relation to others used to analyse intracrystalline distortion
120 and suggest future developments. We note that the methods discussed here are applicable to
121 any crystalline material encompassing minerals (including ice), metals and ceramics.

122 **2. The WBV method: background and error analysis**

123 The method gives information on combinations of GND Burgers vectors and GND densities,
124 so we now discuss these two concepts. Imagine a closed loop joining atoms (or unit cells)
125 around a dislocation in “sample coordinates” (Fig. 1a, c). Now move the atoms to the
126 positions they would have in an undistorted crystal: the Burgers vector is the gap opened up

127 in the previously closed loop (red arrows in Fig. 1b, d) in “crystal coordinates”). It can be
 128 described in crystal coordinates (hence dimensionless, for example [100] for the edge and
 129 [001] for the screw) or in sample coordinates (dimensions of length; direction depends on
 130 sample orientation). Dislocation density is a phrase that is used in different ways. It may refer
 131 to the total line length of SSDs in a unit volume. Not all of these give rise to lattice curvature
 132 so here we consider only the total line length of GNDs per unit volume. We illustrate the
 133 basic ideas using a 2D model first.

Fig. 1. a) A closed loop around an edge dislocation in sample space, view down along the dislocation line. b) The same path traced out in crystal coordinates, showing a gap that is the definition of the Burgers vector (red) of the dislocation within the loop. c), d) The same for a screw dislocation; the dislocation line is parallel to the Burgers vector.

134

135 2.1. Concepts in 2D

136 GND density relates to lattice curvature and a 2D description illustrates this most simply,
 137 where there is no distortion in the z or [001] direction. We show here how curvature relates to
 138 single then multiple dislocation populations. Figure 2 shows lattice orientations in a 2D
 139 model which can, at each point, be described by a single number (angle θ of a particular
 140 lattice direction anticlockwise from a reference direction). In 2D all dislocations have edge
 141 character and in the Figure the Burgers vectors are defined as one atomic spacing so $\mathbf{b} =$
 142 [100]. The four frames show increasing dislocation density ρ , defined in 2D as the number of
 143 dislocations per unit area, and the corresponding increase in lattice curvature. The irregular
 144 spacing of dislocations means this model is an approximate illustration but provides a basis
 145 for understanding.

146

Figure 2. Visualization of the link between GND density (chosen here as edge dislocations all the same sign) and lattice curvature. The crystallographic “z” direction [001] is chosen as out of the page so the dislocations illustrated have line vector [001] and Burgers vector [100]. Angle θ , dependent on position, shows orientation of a lattice direction relative to a reference direction (thick line).

147

148 EBSD measurements do not pick out individual atoms but provide orientation θ as a defined
 149 function of position (in 2D, $\theta(x, y)$); that is what we must work with. Lattice curvature is
 150 defined by variations in θ in the x and/or y directions. The lattice curvature is then a vector

$$151 \quad \boldsymbol{\kappa} = - \left(\frac{\partial \theta}{\partial x}, \frac{\partial \theta}{\partial y} \right) \quad (1)$$

152 (see Appendix 2.1 for details). There is one key assumption made when using the WBV
 153 method: that elastic strains have a relatively small effect. If EBSD records lattice curvature,
 154 then that could in principle be caused by elastic strain. As EBSD cannot generally image
 155 individual dislocations, an EBSD map of (for example) Fig. 2 could look identical to a map
 156 of a perfect lattice with no GNDs, elastically bent. However, as was argued in Wheeler et al.
 157 (2009), in the microstructures we have studied, curvature is often localized along sub-grain

158 walls and we cannot conceive of elastic strain being localized in this way. Secondly, we
 159 would expect elastic bending in a wide variety of orientations in a polycrystal, giving rise to a
 160 wide variety of (illusory) WBVs. Instead, we see systematic patterns as exhibited in the case
 161 studies we present here, and in most of the published studies (Table 1). Wallis et al. (2019a)
 162 find that “often the rotation gradients are larger than the elastic strain gradients ... in which
 163 case, the elastic strain gradients can be neglected”.

164 From now on we will assume no elastic strains and, in that case, κ relates to a single
 165 population of GNDs by

$$166 \quad \kappa = \rho \mathbf{b}$$

167 that incorporates the fact that in sample coordinates, \mathbf{b} may vary even if it is a single
 168 crystallographic direction. Considering just the magnitudes, we can write this as

$$169 \quad (\text{curvature}) = (\text{dislocation density}) \times (\text{Burgers vector length})$$

170 which is a starting point for understanding the link between curvature and dislocation density.
 171 If there is more than one type of dislocation (each with different Burgers vectors and
 172 densities)

$$173 \quad \kappa = \sum_N \rho^{(N)} \mathbf{b}^{(N)} \quad (2)$$

174 where ρ and \mathbf{b} are the density and Burgers vectors *for each type* (superscript N) of
 175 dislocation. If there were just 2 types of dislocation, this equation would yield their densities
 176 uniquely. If more than 2 types are present then the densities are non-unique, but the equation
 177 still provides constraints. Such issues are relevant for 3D which we now discuss.

178 2.2. Concepts in 3D

179 In 3D we require three numbers to define a lattice orientation (e.g. conventionally three Euler
 180 angles, although other representations are available), and we have three directions in which to
 181 evaluate gradients, there are 9 gradients to consider. Nye (1953) showed how curvature is
 182 then a second rank tensor, but a more direct link to dislocation density (line length per unit
 183 volume in 3D) is established via a tensor α (which now carries his name), also a function of
 184 orientation gradients. This links to dislocation density as follows.

$$185 \quad \alpha_{i\gamma} = \sum_N \rho^{(N)} b_i^{(N)} l_\gamma^{(N)} \quad (3)$$

186 where ρ , \mathbf{b} and \mathbf{l} are the density, Burgers vector and unit line vector for each type (labelled N)
 187 of dislocation. Note the close resemblance to eqn 2, but with the extension to include
 188 dislocation line vectors. When there are many types of dislocation, there may be multiple
 189 combinations giving a particular Nye tensor. Note the following.

- 190 • This has to be written in terms of vectors and tensors, since the situation is 3D.
- 191 • Such equations are best written using index notation which makes explicit whether
 192 vectors are expressed in crystal coordinates (Latin subscript for b_i) or sample coordinates
 193 (Greek subscript for l_γ), for reasons explained in Wheeler et al. (2009) and Das et al.
 194 (2018).
- 195 • α is sometimes called “dislocation density” but must be distinguished from other uses of
 196 the same phrase.

197 Determining the full Nye tensor requires orientation gradients in all three directions.
 198 Although there are GND studies using 3D EBSD from serial focussed ion beam milling e.g.
 199 (Kalácska et al. 2020, Konijnenberg et al. 2015) these are challenging and generally EBSD is
 200 conducted on 2D sections. Wheeler et al. (2009) showed that relevant (though incomplete)
 201 information could still be extracted from a 2D map. Specifically, of the 9 components of the
 202 Nye tensor, a 3-component vector can be calculated. The vector is a sum of Burgers vectors
 203 of GNDs, *weighted* by the actual dislocation density of each type of GND and by the angle
 204 between the dislocation lines and the map. Lines at a high angle to the map are favoured
 205 because the mathematics involves multiplying the true density by $\sin(\text{angle between}$
 206 $\text{dislocation line and map})$. The phrase “weighted Burgers vector” (WBV) was used, to make
 207 clear that this vector is a weighted “sample” of the Nye tensor.

$$208 \quad W_i = \alpha_{i3} = \sum_N \rho^{(N)} b_i^{(N)} l_3^{(N)} = \sum_N \left[\rho^{(N)} l_3^{(N)} \right] b_i^{(N)} \quad (4)$$

209 where \mathbf{W} is the WBV, and the subscript “3” refers to the z direction, perpendicular to the
 210 map, so l_3 is the component of a dislocation line vector perpendicular to the map: it varies
 211 from 0 (lines parallel to map) to 1 (lines perpendicular to map). The terms in square brackets
 212 are scalars, so note that the WBV is a linear combination of Burgers vectors – this is one
 213 reason why it is a useful quantity. The WBV has units of $(\text{length})^{-1}$ and we recommend using
 214 the convenient unit of $(\mu\text{m})^{-1}$. We denote its magnitude as W . It can be expressed in crystal
 215 coordinates as in eqn (4), or in sample coordinates by calculating $\mathbf{h}\mathbf{W}$ where \mathbf{h} is the
 216 orientation tensor (a function of Euler angles). It might appear that this will give a non-
 217 unique answer for the vector in sample coordinates, since \mathbf{W} has symmetric variants in
 218 crystal coordinates, but Appendix 1 shows this is not the case – there is a unique WBV in
 219 sample coordinates.

220 There are two approaches to calculating \mathbf{W} , differential and integral. The differential method
 221 involves evaluating local gradients in \mathbf{h} around the point at which \mathbf{W} is required. Since that
 222 point has a specific orientation, \mathbf{W} can be expressed in crystal or sample coordinates. The
 223 integral method involves integrating round a closed loop on the map to obtain the *net* or
 224 *average* Burgers vector content of the GND lines intersecting the map inside the loop,
 225 expressed in crystal coordinates. The mathematics in essence defines the loop in sample
 226 coordinates (c.f. Fig. 1a) black arrows), transforms each loop segment (black arrow) into
 227 crystal coordinates (c.f. Fig. 1b) black arrows), and sums up the segments in crystal
 228 coordinates to give the net Burgers vector (red arrow). For the calculation to be meaningful
 229 there should be no “high angle” grain boundaries (HAGBs) (which do not usually have
 230 organised dislocation substructures) intersected by the loop. If the loop crosses HAGBs then
 231 the calculation will still return a vector, but that will not give clear information on
 232 dislocations. There is no systematic knowledge of or agreement on what constitutes an
 233 HAGB and we usually pick 5 degrees as a maximum angle, discussed further in section 2.2.5.
 234 Unlike the differential method, there is no strict way to express the vector in sample
 235 coordinates because orientation varies around and within the loop and the result of the
 236 integral method is not linked to any specific point within the loop. However, if the loop does
 237 not include HAGBs then orientation variations in the loop are small and the orientation at, for
 238 example, the loop centroid could be used to convert from crystal to sample coordinates.

239 If the orientation \mathbf{h} is a defined mathematical function of position, then the methods are
 240 identical (they are related by Stokes' theorem). In practice \mathbf{h} is defined at discrete
 241 measurement points, e.g. on a square grid. The differential method then involves numerical
 242 estimation of orientation gradients, with some flexibility in terms of the number of points
 243 used. The integral method involves numerical integration around the closed loop. As we will
 244 show later (section 2.3), the methods have different advantages in practice.

245 2.2.1. WBV, lattice vectors and Burgers vectors

246 In this section we discuss the links between WBV and Burgers vectors and show how there
 247 may be unique or non-unique relationships. In the approach we describe here, the
 248 “differential” values of WBV are usually expressed in units of $(\mu\text{m})^{-1}$. In crystal coordinates
 249 \mathbf{W} can be decomposed into lattice basis vectors \mathbf{L} if needed

$$250 \quad \mathbf{W} = K_1\mathbf{L}_1 + K_2\mathbf{L}_2 + K_3\mathbf{L}_3 \quad (5)$$

251 where the coefficients K are in units of $(\text{length})^{-2}$. These coefficients *resemble* dislocation
 252 densities but are in general different. This decomposition relates to the GND types and
 253 densities and is unique but further assumptions are needed to express it in terms of the
 254 Burgers vectors of actual slip systems. For example, in olivine, slips systems have Burgers
 255 vectors that are either [100] or [001]. If we find that \mathbf{W} is parallel to [203] and we know the
 256 distortion is due to crystal plasticity then we can deduce that it shows a combination of slip
 257 systems with [100] and [001] Burgers vectors. The magnitude of \mathbf{W} parallel to [100] would
 258 then, in accord with eqn. (4), be a weighted sum of the dislocation densities of all types of
 259 dislocation with [100] Burgers vectors. In anhydrite, also orthorhombic, slip systems can
 260 involve [001], [1-1-2] and [11-2] Burgers vectors (Hildyard et al. 2009). There is a unique
 261 way to express the three components of \mathbf{W} in terms of those three vectors, if those vectors are
 262 linearly independent: in this example [203] = 7[001] + [1-1-2] + [11-2]. However, many
 263 crystals have more than three Burgers vectors for possible slip systems, especially in more
 264 symmetric crystals counting all symmetric variants. For example, in a trigonal phase such as
 265 calcite, there will be at least 3 Burgers vectors in the basal plane. Any two of these can be
 266 combined to give the basal plane component of \mathbf{W} , so the decomposition is non-unique. \mathbf{W}
 267 still carries valuable information on the relative contributions of dislocations with basal and
 268 non-basal Burgers vectors (Chauve et al. 2017). Our philosophy here is that the methods give
 269 the value of \mathbf{W} , and if further assumptions are required (in terms of expected slip systems,
 270 relative energies etc.) these should be made on a case-by-case basis. The K coefficients can
 271 be related to GND densities using further information such as the specific Burgers vectors of
 272 GNDs.

273 Except for angular errors which are discussed later, it is crucial to note that the WBV cannot
 274 generate “phantom” directions: it must be the weighted average of Burgers vectors that are
 275 actually present in the microstructure. For example, regardless of mineral symmetry, if \mathbf{W} is
 276 [203] then *at least one* of the GND types involved *must* have Burgers vector with an [001]
 277 component, though not necessarily parallel to [001]. Similarly, *at least one* of the GND types
 278 involved *must* have Burgers vector with an [100] component. \mathbf{W} could be decomposed as
 279 $2[100] + 3[001]$, or $2[101] + 1[001]$, or $3[101] - 1[001]$ or even simply $1[203]$ if [203] is a
 280 known Burgers vector.

281 We next illustrate how to visualise and interpret the WBV, using models for a smoothly tilted
 282 lattice and a smoothly twisted lattice (for illustration, distortions are much larger than those
 283 found in real crystals). We then address a tilt subgrain wall, describing some issues that are
 284 specific to sharp changes in orientation. The models have no variation of orientation in the z
 285 direction and the Nye tensors can be calculated fully (Appendix 2).

286

Figure 3. Basic WBV concepts illustrated with model tilted and twisted crystals. a), b) 3D views of model tilted and twisted crystals, planes are colour coded in accord with IPF key (inset) for plane normal. Pale yellow of semi-transparent rectangles indicates the map plane though not the shape, with x and y marked for subsequent maps. c), d) Misorientation relative to top-left corner for tilt and twist models. In c) misorientation is around the [001] axis that points out of the page. In d) misorientation is around the [010] axis, running left-right, with linearly increasing gradient of twist angle to right. e), f) WBV magnitude (in μm^{-1}) colour coded for each model. In e) actual vector directions shown as white arrows; in f) WBV directions point directly into page so are not shown. The boxes are example integration loops with the net WBV indicated as K coefficients in $(\mu\text{m})^{-2}$. g), h) WBV direction colour coded for each model. i) 3D view of semi-transparent WBV magnitude map for tilt model (as in (e)), with edge dislocations lines shown schematically: parallel to [010] and colour coded in accord with their [100] Burgers vectors. j) 3D view of semi-transparent WBV direction map for twist model (as in (h)), with two sets of screw dislocations lines shown schematically: blue parallel to [100], red parallel to [001]. For visual clarity the dislocations are shown as if in walls, but the distortion gradient is smooth. Note how the “weighting” towards dislocation lines perpendicular to the map causes variation in WBV direction (as in f) although the relative density of the two types of dislocation is uniform in 3D.

287

288 2.2.2. Smoothly tilted crystal

289 This model is similar to Fig 2, with a 3D view shown in Fig. 3a). The lattice is misoriented
 290 relative to the y-axis by an angle θ (zero along the y-axis and < 0 to the right), Fig. 3c). The
 291 misorientation axis is [001] that points out of the page. The centre of curvature is beyond the
 292 bottom left of the map (Fig. 3c)). If r is the distance to this centre, it is the radius of curvature
 293 of the lattice and in sample coordinates

$$294 \quad \mathbf{W} = \frac{1}{r}(\cos \theta, \sin \theta, 0)$$

295 and in crystal coordinates,

$$296 \quad \mathbf{W} = \frac{1}{r}(1, 0, 0) \tag{6}$$

297 The magnitude of W is shown in Fig. 3e), increasing towards the centre of curvature in
 298 accord with eqn. (6). The WBV is a vector that can be represented in sample or crystal space:
 299 these require different methods for visualising direction. In sample space WBVs can be
 300 displayed as arrows on a map as in Fig. 3e). The direction in crystal coordinates is colour
 301 coded (as in any other sort of IPF map) in Fig. 3g), with the IPF colour scheme inset. Since
 302 \mathbf{W} is everywhere parallel to [100] we see a single colour. The rectangle is an integral loop

303 labelled with its net Burgers vector content in units of $(\mu\text{m})^{-2}$; note only the first [100]
 304 component is non-zero.

305 Multiple decompositions of \mathbf{W} are possible, but the simplest is a single population of edge
 306 dislocations with lines parallel to [001], Burgers vectors parallel to [100] and density

$$307 \frac{1}{ar}$$

308 where a is the length of [100]. Fig. 3i) shows a 3D view of that model. If this were not a
 309 model, all the map and WBV data could be in accord with other interpretations, for example
 310 dislocation lines not parallel to z . However, *any* interpretation must involve dislocations with
 311 Burgers vectors with a [100] component: the WBV calculation cannot generate “phantom”
 312 components (see above).

313 2.2.3. Smoothly twisted crystal

314 This model illustrates the importance of understanding the “weighting” or stereological bias
 315 in the WBV calculation. In Fig. 3b) the twist is defined by misorientation by angle θ around
 316 the [010] axis, with $\frac{d\theta}{dx}$ increasing to the right. Fig. 3d) shows the misorientation, defined as
 317 the *minimum* angle (with no absolute sign) required to rotate a lattice back to a reference
 318 orientation, relative to the top-left corner. Because this is olivine, symmetry dictates that the
 319 misorientation reaches a maximum at 90 degrees then decreases rightwards even though the
 320 lattice is more twisted to the right and the angle θ used for calculations increases
 321 monotonically. In sample coordinates
 322 (appendix 2.2) we have

$$324 \mathbf{W} = \frac{d\theta}{dx} (0, 0, -1)$$

325 In crystal coordinates

$$326 \mathbf{W} = \frac{d\theta}{dx} (\sin \theta, 0, -\cos \theta) . \quad (7)$$

327 The magnitude of \mathbf{W} is simply $\frac{d\theta}{dx}$ and increases linearly to the right because θ is quadratic in
 328 x (Fig. 3f)). WBV arrows in sample coordinates are not shown for the twist example because
 329 they all point vertically out of the map. Despite the fact that individual dislocation lines and
 330 Burgers vectors are clearly not vertical, the WBV components parallel to the map cancel out
 331 because we are adding weighted contributions. In crystal coordinates the direction of \mathbf{W}
 332 varies sinusoidally with θ (Fig. 3h)). The rectangle is an integral loop labelled with its net
 333 Burgers vector content in units of $(\mu\text{m})^{-2}$; note both [100] and [001] components are non-
 334 zero, in agreement with the presence of blues and purples within the loop. The variation in
 335 WBV direction across the map could be interpreted to mean that different types of dislocation
 336 predominate in different parts of the model. This is not the case: it is a stereological effect
 337 and needs careful explanation now because such effects must be borne in mind in any study.

338 Multiple decompositions of \mathbf{W} are possible, but the simplest is as a sum of contributions from
 339 screw dislocations parallel to [100] with a density of

$$340 \frac{1}{a} \frac{d\theta}{dx}$$

341 and screw dislocations parallel to [001] with a density of

342 $\frac{1}{c} \frac{d\theta}{dx}$.

343 This decomposition is shown in Fig. 3j). The screw dislocation lines are coloured using the
 344 IPF colour scheme for screw dislocation *line direction* (as in Fig. 3g)) but since these are
 345 screw dislocations the colours also indicate Burgers vector directions. Consider the model
 346 near the left hand end where θ is small. Blue dislocations, with [100] line vectors, are almost
 347 parallel to the map. This means the WBV calculation does not “sample” them and the IPF
 348 colour (Fig. 3h)) is dominated by red [001]. As the lattice is more twisted passing to the right,
 349 [100] lines are at higher and higher angles to the map. Hence the WBV IPF map is more
 350 dominated by blue. At a position near the right-hand side of the map, [001] lines are parallel
 351 to the maps so are not sampled at all; the IPF map is blue. As θ increases beyond 90 degrees
 352 we see an influence of [001] reappear. This is an example of the “weighting” towards
 353 dislocation lines at a high angle to the map.

354 The twist structure illuminates some fundamental aspects of WBV. The displays are entirely
 355 in accord with eqn. (7) and the WBV provides a weighted “subset” of the full dislocation
 356 population. If we were to examine another map at right angles to the one considered (but still
 357 containing the twist rotation axis) this second map would show a preponderance of [100]
 358 vectors at the left end, with more [001] passing to the right – it would look quite different.

359 2.2.4. Model of subgrain tilt wall

360 Many microstructures contain subgrain walls that, although populated by GNDs, have in
 361 essence zero width and hence zero volume. This means that dislocation density, defined as
 362 line length per unit volume, is infinite. Similarly, a sharp change in orientation means the
 363 lattice curvature is infinite. So, although eqn. (4) still applies, it is not particularly helpful. In
 364 contrast the integral method is helpful because it still yields finite values when the loop
 365 crosses a subgrain wall. For any particular subgrain wall the net Burgers vector content **B**
 366 depends only the length of subgrain wall intersected by the loop, and not on the loop area. In
 367 this paper we use a vector **B/A** with units of (length)⁻¹ to characterise the GND content of any
 368 loop. For a subgrain wall, then, the magnitude of **B/A** is strongly influenced by loop area.
 369 Fig. 4 shows three loops, each intersecting the same length of subgrain wall and having the
 370 same value of **B**. The areas differ and so the magnitudes of **B/A** differ; however, the *direction*
 371 of **B/A** is not influenced by A and carries useful GND information. The advantage of the
 372 integral method for analysing subgrain walls persists when we consider spaced measurement
 373 points (section 2.3.2).

Fig. 4. Numerical aspects in of subgrain wall analysis - a sharp boundary indicated by green line, misorientation 5.6° around [001], crystal directions shown on either side with exaggerated misorientation for clarity. The 3 white boxes are used as loops to indicate the average dislocation density using the integral method (inset numbers for each box): they have relative lengths 1, 2 and 3.

374

375 So far we have assumed that all the analysed distortions are due to GNDs, but for sufficiently
 376 high angle boundaries this will not be the case. We discuss this in detail next.

377 2.2.5 “High angle” boundaries and boundary dislocation content

378

379 When can boundaries be regarded as made of GNDs? Questions emerge for high angle grain
380 boundaries (HAGBs) where basic geometry proves that dislocations with specific Burgers
381 vectors must be close together and may not be recognisable as discrete entities. White (1976)
382 states “The limit is reached when dislocations are so closely spaced that they lose their
383 individual identity and when this happens the boundary is no longer a low angle sub-grain
384 boundary but a high angle, mobile, grain boundary. If a spacing of 2.5 nm (five lattice
385 spacings) is taken as the minimum distance before core interference ... then a low angle
386 boundary becomes a grain boundary when the misorientation is about 10° ”. Trimby et al.
387 (1998) state “Without detailed TEM [Transmission Electron Microscopy] studies the nature
388 of a boundary can only be constrained from the nature of the misorientation across it”: here
389 “constrained” does not mean “fully described”. They continue “In many studies an arbitrary
390 misorientation value is assigned, above which boundaries are assumed to be grain boundaries
391 and below which they are assumed to be subgrain walls although, in some cases (e.g. quartz),
392 this value corresponds to the necessary misorientation for the overlap of dislocation cores.
393 Typical values are 10° for quartz (White 1976), 15° or more for halite (Guillopé & Poirier
394 1979) and 15° for olivine (Poirier & Nicolas 1975)”. Two decades later there is still a lack of
395 clarity regarding such angles, but we discuss some relevant work next.

396

397 Shigematsu et al. (2006) coupled TEM to EBSD and showed that in quartz boundaries
398 dislocation substructures were lost somewhere between 9° and 17° , with one 13.5° boundary
399 still having dislocations (beyond the angular limit of 10° mentioned above). Mamtani et al.
400 (2020) image dislocations near HAGBs in magnetite using TEM as do Zhang et al. (2020) in
401 a Pd-10%Au alloy. So, HAGBs are not always disorganised. Kuhr and Farkas (2019) used
402 molecular dynamics models of an FCC polycrystal and found dislocations present in some
403 HAGBs. Twin boundaries may have dislocations e.g. p 79 of (Sutton & Balluffi 1995) but if
404 the twin plane is perfectly oriented there are none. An attempt to apply the WBV calculation
405 would yield an enormous and illusory dislocation density. Some HAGBs have lattices in
406 direct contact (Marquardt & Faul 2018), others may have amorphous films nm thick (Wirth
407 1996). In summary, HAGBs have diverse characteristics. We cannot address that diversity
408 here; nor can other methods of using EBSD data to deduce dislocation information. We
409 simply assert that our calculation is interpreted assuming that the lattice curvature is due to
410 the presence of GNDs. There is no single “cut-off” HAGB angle beyond which the GND
411 assumption is invalid. For this reason, in the algorithms we have created the user chooses the
412 HAGB angle above which calculations are excluded. The WBV method may in future
413 provide useful information about HAGB structure, but further research is required.

414

415 Our models up to this point are based on algebraic descriptions of distorted lattices (see
416 Appendix 2). We next address the finite number of measurement points that comprise an
417 actual EBSD map, and their consequences for gradient and WBV calculations (section 2.3).
418 We then explore the errors in orientation and their consequences for those calculations
419 (section 2.4).

420 2.3. Numerical aspects of analysing spaced EBSD measurement points

421 Orientation data to be analysed are not mathematical functions of position but discrete
422 measurements at scattered measurement points (hereafter, simply “points” for brevity). The
423 calculation methods therefore involve numerical approximations to the gradients and
424 integrals of the underlying theory, and the differential and integral methods have different

425 advantages in practice. The points in the studies we describe are on square grids, but there is
426 no reason why the method should not be extended to hexagonal or other grids.

427 2.3.1. Differential method

428 The differential method uses gradients in orientation in the x and y map directions to
429 calculate the WBV. A numerical estimation of gradients uses 2 or more orientation
430 measurements and the distances between the points. We call the cluster of points used a
431 “stencil” (Fig. 5a)). Here each measurement point is represented by a square with a side equal
432 to the step size, so a stencil is illustrated as a cluster of squares. For flexibility our software
433 allows for different stencil sizes; the differential method calculates a “best fit” lattice
434 curvature using the orientations at each point in the stencil. Using larger stencils reduces
435 errors in calculation (discussed later), but at the same time “smears out” microstructural
436 details on the scale of the stencil. In published works the $P = 9$ stencil has usually been used;
437 we discuss the effects of stencil size in the section on accuracy below.

Figure 5. Stencils, orientation gradients and errors relevant for WBV. a) “Stencils” are arrangements of nearby measurement points (shown here as squares) used for numerical calculation of orientation gradients at the central point (coloured). Shown are example stencils of area 3, 5, 9 and 21. b) Illustration of effects of orientation errors. Blue graph shows a low but uniform orientation gradient (in 1D) with errors imposed. Red lines show the large effects of errors on estimating gradients over a short segment (analogous to using a small stencil). Note the estimate may even have the wrong sign. Orange line shows the improved precision using a longer segment (analogous to using a larger stencil as in a)). Inset illustrates consequent angular error in WBV direction (in 2D). The actual WBV is shown as middle arrow but with error ε (related to the gradient error) so WBV values might fall in the circle. Outer arrows illustrate the range of directions and hence the angular error δ that would arise due to these errors. c) as in b), with the same errors imposed, but for a larger orientation gradient. The errors in slope are the same as in b) but are *proportionately* less. The error ε in WBV is the same as in b) and the size of the error circle is the same for both. However, the angular error δ is smaller in c) because the WBV is longer.

438

439 In section 2.2.4 we pointed out that if a subgrain wall is considered as having zero width, it
440 will have infinite dislocation density. Because of this numerical differentiation creates
441 numerical artefacts as it uses spaced measurement points. The algorithm cannot distinguish a
442 sharp orientation change between two points from a smooth orientation gradient between
443 those points. A consequence is that if a subgrain wall is present, the apparent WBV
444 magnitude will be finite and depend on step size, so should be interpreted with care. In
445 practice we find that narrow “swathes” of high W are common on calculated W maps and are
446 likely to be subgrain walls. In this case the magnitude W must be interpreted with care but the
447 WBV direction still contains information on the Burgers vectors of the GNDs in the subgrain
448 wall. The 3 boxes in Fig. 6 indicate the calculated W values for a sharp orientation boundary,
449 using the differential method using stencils with areas 9, 13 and 21. Note how the dislocation
450 density is smeared out more for larger stencils, and has apparently lower values.

Fig. 6. Numerical aspects in of subgrain wall analysis - a sharp orientation boundary indicated by green line – using the differential method. The 3 black boxes show regions in which W has been calculated using stencils of size 9 (top), 13 and 21. Compare Fig. 4 which uses the integral method on the same boundary.

451

452 *2.3.2. Integral method*

453 The integral method involves integrating the orientation tensor around a closed loop in the
 454 map plane, directly giving the net Burgers vector sum for all the dislocation lines threading
 455 through that loop. The details of numerical integration are given in Supplementary
 456 Information 1.2. Publications to date have restricted loop shapes to rectangles, though there is
 457 no fundamental difficulty in implementing other shapes and this has been done in a
 458 commercial version of the algorithm in the Oxford Instruments Aztec system. The result of
 459 integration is a vector \mathbf{B} with dimensions of length. We divide this by the loop area A to get a
 460 vector in $(\text{length})^{-1}$ which is more easily compared to results of the differential method.
 461 Algebraically, the vector \mathbf{B}/A must equal the average W value in the loop (eqn. (6)).
 462 Numerically, the “best fit” algorithm used in the differential method means the methods may
 463 give slightly different results; for subgrain walls the integral method remains advantageous
 464 (c.f. section 2.2.4).

465 In Wheeler et al. (2009) the integral method was presented as an exploratory tool in which
 466 the user drew rectangular loops and the WBV was reported as a lattice vector (e.g. Fig 3e,
 467 f)). More recently a method of systematically “tiling” the map with square loops, and
 468 applying the integral method to each loop was used in Fig. 8c of Timms et al. (2019). The
 469 tiles can be displayed colour coded by standard IPF colour schemes using a W threshold, in
 470 the same way as for calculations made with stencils (examples are given later). The tiles can
 471 be thought of as large pixels, though not all properties are precisely analogous to those of
 472 individual measurement points. In all circumstances, if the loop crosses a high angle
 473 boundary, then a WBV can in principle be calculated but as discussed above, has no meaning
 474 - so instead the algorithms we use do not return a result and the tile is left uncoloured.

475 *2.4. Numerical aspects of dealing with orientation measurement errors*

476 Orientation measurements used may be in error as a result of errors in the Hough transform,
 477 up to a degree at most (Prior et al. 2009); for one study on an Si single crystal, was 0.2° (Ram
 478 et al. 2015). Improved “real time” approaches to indexing Kikuchi patterns reduce the
 479 angular error in orientations to $<0.05^\circ$ (Nicolay et al. 2019). For higher angular resolution
 480 methods, e.g. correlating Kikuchi patterns, errors may be as low as ~ 0.0003 radians (Wallis et
 481 al. 2019a). The differential method uses gradients in crystal orientation to calculate WBV. On
 482 the grid of measurement points, a gradient is calculated from the misorientations between
 483 adjacent measurements. The misorientation angles are likely to be small and so the errors in
 484 misorientation axes will be large (Prior 1999) and these errors will propagate into the WBV
 485 calculation. An algebraic analysis would involve error propagation through operations on
 486 various orientation tensors and is beyond the scope of this contribution; instead, we use
 487 simple arguments followed by some numerical experiments.

488 *2.4.1. General nature of error effects*

489 We argue in this section that angular errors in WBV are smaller for long WBVs. Longer
 490 WBVs are linked to higher lattice curvatures. Higher lattice curvatures mean the
 491 misorientation angles between adjacent pixels are larger, and the misorientation axes will

492 have smaller errors, and the WBV direction will have smaller errors. We illustrate this
 493 assuming a typical orientation error of 0.01 radians.

494 Benchmark curvature (above which calculation will be less error prone) $\sim 0.01/(\text{step size})$

495 and in terms of magnitude

496 $|\text{WBV}| \sim \text{curvature}$

497 which means we should consider a benchmark below which WBV is error-prone as

498 $|\text{WBV}| \sim 0.01/(\text{step size}) = W_t$

499 This approach is similar to the derivation of eqn. 13 of Wilkinson and Randman (2010) and
 500 eqn 2 of Jiang et al. (2013), where a lower limit on detectable dislocation density is given in
 501 terms of step size:

502 (Minimum detectable GND density) \sim

503 $(\text{Angular resolution}) / ((\text{step size}) * (\text{Burgers vector length}))$

504 For example $0.01 / ((1 \text{ micron}) * (5 \text{ angstrom})) = 2 \times 10^{13} \text{ m}^{-2}$

505 The approach described below is related because in order of magnitude, $W = \rho b$. Hence our
 506 W_t/b equates to the minimum detectable GND density discussed in other work. That work,
 507 and others (by the group) focusses on accuracy in determining dislocation *density*; here we
 508 also analyse WBV *direction* since it plays a key role in several studies (Table 1). In Wheeler
 509 et al. (2009) we argued that longer WBVs would be more accurate in terms of direction. For
 510 example, the map of Mg used in Fig. 2 and 3 of Wheeler et al. (2009), modified in Fig. 7, has
 511 a step size of $4 \mu\text{m}$ so $W_t = 0.0025 \mu\text{m}^{-1}$. Fig. 7 shows considerable scatter for $W > 0.002 \mu\text{m}^{-1}$
 512 1 and much less for $W > 0.004 \mu\text{m}^{-1}$, in accordance with the argument that W_t offers a guide
 513 to judging precision. Guided by this, our approach to displaying WBV data involves selecting
 514 data based on ranges of W . The minimum value W_{min} in the range will be associated with the
 515 maximum angular error. Setting it high will reduce error. The maximum value W_{max} is less
 516 important but is useful for dividing up datasets.

<p>Figure 7. IPFs of Mg WBV displayed using three different thresholds: threshold lengths and numbers of points as indicated, modified from Fig. 3 of Wheeler et al. (2009).</p>
--

517

518 Figure 5b) and c) are non-rigorous illustrations of error effects. The graphs illustrate that
 519 larger stencils will give better precision. Errors ε in gradients are independent of the gradients
 520 themselves but for larger orientation gradients (as in Fig. 5c)), longer WBVs) the errors are
 521 *proportionately* less important. The insets in b) and c) illustrate the consequent effects on
 522 angular errors. The errors in WBV are now drawn as circles around the actual values since
 523 errors may be in any direction. The error circles are the same size in b) and c). The green
 524 arrows mark the vectors with maximum angular error δ , showing that longer WBVs in c) will
 525 have smaller angular errors. In the next section we analyse error effects using numerical
 526 models.

527 2.4.2. Specific analyses of error effects

528 It is useful to quantify error estimates for WBV, incorporating the effects of WBV length and
 529 other parameters. We define an angle α_{95} so that there is a 95% chance that the true WBV
 530 direction is that angle or less from the calculated direction, an approach used in analysing
 531 palaeomagnetic data for example Butler (1992). In essence α_{95} defines a cone of directions
 532 within which the true direction is likely to be. This is analogous to the ± 2 standard deviation
 533 range within which 95% of the data lie when dealing with a one-dimensional normal
 534 distribution. Our approach gives the angular error for the WBV in sample coordinates: it is in
 535 principal the same for crystal coordinates except crystal symmetry may modify the
 536 interpretation, as addressed in Appendix 3.1.

537 EBSD orientation errors will depend on mineralogy, acquisition conditions and indexing
 538 methods and will propagate in the WBV calculations. For illustration we create model
 539 orientation maps with angular errors in orientation up to 0.57° (0.01 rad) – so our angular
 540 error estimates for WBVs are likely to be pessimistic. We used theoretical models shown in
 541 Fig. 3 with added orientation noise, and calculated \mathbf{W} for the noisy datasets. Larger stencils
 542 and tiles take into account more orientation measurements and, in common with other
 543 averaging methods, we hypothesised in Wheeler et al. (2009) that this would give higher
 544 precision. We examine this idea in Appendix 3. First, we calculate the error on WBV, by
 545 comparing actual \mathbf{W} and theoretical \mathbf{W}_c values. We find that the error in WBV magnitudes \mathbf{E}
 546 $= \mathbf{W} - \mathbf{W}_c$ are not strongly dependent on length W , or on whether the model is tilt or twist,
 547 but they do depend on stencil size. To quantify the errors, we calculate a standard deviation σ
 548 for the vector \mathbf{E} as described in Appendix 3. Larger stencils and tiles give smaller errors (Fig.
 549 6). So, if one uses stencils (i.e the differential method), there is an approximate relationship
 550 between W precision and the area S of a stencil (number of points, hence dimensionless)

$$551 \quad \sigma_S = 0.0247S^{-1}/u \quad (7)$$

552 where u is step size.

553 If one uses tiles (i.e. the integral method) and defines the dimensionless area T of a tile the
 554 standard deviation σ_T of vector \mathbf{E} is:

$$555 \quad \sigma_T = 0.0081T^{-3/4}/u . \quad (8)$$

Figure 8. a) Standard deviation σ of nondimensionalised WBV magnitude plotted against calculation region size for tilt and twist models, showing errors are independent of the detailed nature of distortion. The three left-hand points are for stencils, the others are for tiles. b) Same, plotted against areas of stencils and tiles for both tilt and twist models. c) Same as b) but plotted as log-log graphs to show linear relationships.

556

557 In Wheeler et al. (2009) we suggested that the integral method would have higher precision
 558 than the differential method because numerical integration is less sensitive to errors than
 559 numerical differentiation. Our assertion was correct because we were using small stencils (P
 560 $= 9$) and large integral loops. Fig. 8 b) and c) show that in fact the precision depends mainly
 561 on the area of the tile or stencil used. The integral method remains our favoured method for
 562 initial exploration since the calculation is much faster than for a stencil of comparable size.

563 The second stage of error analysis involves the angular errors. These *do* depend on the length
 564 W as described above and in Fig. 8. The inset in Fig 5c) suggests that $\delta \approx \varepsilon/W$ when errors
 565 are small. This is in accord with Fig. S1. One might then expect some proportionality
 566 between measures of vector error σ and angular error α_{95} in a more rigorous approach, and
 567 this is confirmed in Appendix 3. For small errors we have

$$568 \quad \alpha_{95} \cong 1.413 \frac{\sigma}{W}$$

569 For example, in Table 1, for the second Mg example we have a step size of 4 μm and
 570 calculated the WBV using a stencil area 9 so $\sigma_s = 0.000686 \mu\text{m}^{-1}$. For a WBV length 0.004
 571 μm^{-1} we have

$$572 \quad \alpha_{95} \cong 1.413 \frac{0.000686}{0.004} = 0.24 \text{ rad} = 13.8^\circ$$

573 (the table calculation is more precise). If we compare the calculated α_{95} with Fig. 7c), it is
 574 plausible that the dislocations are all basal and we see a scatter up to 14° away from the basal
 575 plane, broadly in accord with the calculation. The above assessment of precision should be
 576 used with caution, since it assumes a particular range of orientation errors in the measured
 577 data, and those errors are dependent on acquisition conditions and the mineral being
 578 measured. A larger stencil or tile will give a more precise measure of WBV magnitude and
 579 direction, but larger regions are also more likely to contain more than one type of dislocation.
 580 There is a trade-off between finding a relatively precise WBV direction in a large region that
 581 may contain more than one type of GND, versus finding a less precise direction in a smaller
 582 region which may relate to a single type of GND.

583 Our error analysis is numerical rather than algebraic but simple calculations give confidence
 584 that, if other parameters are maintained, the WBV angular error will scale linearly with
 585 orientation angular error. Thus, if angular errors are distributed uniformly between 0 and
 586 0.001 rad, we expect angular errors in WBV to be 10 times less than those we present here.
 587 Such low indexing errors are now routinely possible, albeit with a trade-off on indexing
 588 speed (Nicolay et al. 2019). Improved indexing would allow for use of a smaller stencil or tile
 589 ensure a particular level of WBV precision. We note that algorithms that assign interpolated
 590 orientations to misindexed or non-indexed pixels may have adverse effects on subsequent
 591 WBV calculations. For example, if the orientation value of an adjacent pixel is used, this
 592 guarantees that there is a zero orientation gradient between those two pixels, which may have
 593 a big (and spurious) influence on the WBV calculation. Ideally, analysis is done only on
 594 confidently indexed points. We also urge caution using dictionary indexed EBSD maps (De
 595 Graef 2020) for WBV calculations, because the orientations stored in the dictionary of
 596 Kikuchi patterns are discrete and orientation gradients therefore will be stepped. This may
 597 give a spurious influence on WBV calculations.

598 **3. WBV applications in Earth Sciences: examples**

599

600 The published works in Table 1 show a variety of approaches for interpreting WBV. The
 601 basic algorithms we use do *not* decompose the WBV down into individual Burgers vectors
 602 because to do this requires additional assumptions, dependent on the particular mineral and
 603 its microstructural evolution. For example, a WBV parallel to [100] may result from a single

604 population of GNDs with Burgers vectors parallel to [100], or a mix of dislocations with
 605 [110] and [1-10]. In some phases, prior knowledge of likely Burgers vectors will mean there
 606 is only one choice for decomposition – e.g. if such a WBV is found in olivine. In the
 607 following, we present first two new examples of WBV usage and then comment on published
 608 examples.

Figure 9. Example of WBV applied to olivine. a) IPF map of Y direction of deformed single crystal of olivine. Scale bar is 1000 μm . b) IPF key. c) IPF coloured as in a), showing a few degrees of distortion within a single initially undeformed crystal. d) WBV magnitude map calculated on 10 x 10 tiles. e) IPF map of WBV direction (calculated as in (d)) superimposed on a band contrast greyscale map; minimum length 0.001 μm^{-1} . f) IPF of WBV as in (e). g) WBV magnitude map calculated on 3 x 3 stencils in part of overview map shown as white box in (d). Scale bar is 1000 μm . Inset shows orientation variation (degrees) from left hand end of transect marked by white line. h) IPF map of WBV direction (calculated as in (g)) superimposed on a band contrast greyscale map; minimum length 0.00005 μm^{-1} , showing subgrain walls with [100] Burgers vectors running NE and those with [001] running NW. White squares indicate results of the integral method, with numbers in μm^{-2} expressed as coefficients of crystal basis vectors (K values). i) IPF of WBV as in (h).

609

610 3.1. Olivine: subgrain wall analysis free from trace, or tilt or twist assumptions

611 Fig. 9 shows an experimentally deformed single crystal of olivine (PI-1766) as in Fig. 8 of
 612 Tielke et al. (2017). The experiment was set up so that the Y (shortening) direction was
 613 initially parallel to [101]_c, at 45° to [100] and [001], with an expectation that slip systems
 614 with [100] and [001] Burgers vectors would be activated. The orientation map (a) shows the
 615 crystal direction that is parallel to the Y sample direction, in accord with the IPF key (b). We
 616 refer to such maps as “IPF Y maps” below. The colour variations reveal rather straight
 617 subgrain walls running in two directions. Orientations vary over a few degrees (c). Fig 9(d)
 618 shows 10 x 10 tiles colour coded by WBV magnitude and (e) by direction, superimposed on
 619 the band contrast greyscale map. The size of the tiles reduces α_{95} but the threshold length for
 620 display is set low, at 0.00005/ μm , so α_{95} is 26°. With this in mind, the IPF Fig 9f) is, within
 621 error, in accord with a mix of dislocations with [100] and [001] Burgers vectors, and the
 622 dominant blue colour on the map indicates mainly [100]. Figs (g) and (h) show a subarea
 623 with WBV now calculated using a 3 x 3 stencil, giving less precision but more spatial
 624 resolution and revealing individual subgrain walls. Blue subgrain walls running NE are
 625 consistent with being [100] tilt boundaries and red subgrain walls running SE are consistent
 626 with being [001] tilt boundaries. A higher threshold length for display (0.001/ μm) means α_{95}
 627 is 14° and the IPF in Fig. (i) is in accord with that, insofar as most points are within 14° of the
 628 plane containing [100] and [001]. There are still mixtures of [100] and [001]. Some will
 629 result from where the stencil overlapped subgrain wall junctions, but as Fig. (h) shows, these
 630 mixtures also appear along irregular segments of the NW-SE subgrain walls and are likely to
 631 represent two types of GND in an individual wall. The three square “loops” show results of
 632 the integral method and provide additional illustration of how the WBV is averaged over the
 633 sample area. Each triplet of numbers is a list of K values, i.e. the coefficients defining the
 634 WBV when it is expressed in crystal basis vectors (eqn (5)). The numbers have the

635 dimensions of dislocation density but must be interpreted with care, as discussed above and
636 shown in Fig. 4, since the dislocations are in discrete walls.

637 In this example the directional information is more useful than the density information:
638 integral and differential methods both give information about where GNDs with [100] and
639 [001] occur. Note that examining the subgrain wall traces together with misorientation axes
640 deduced from the distortion (Fig. 9c) could yield similar results. However, that approach
641 would involve manual and subjective selection of boundary segments and of subregions from
642 which to use misorientation data; it would be based on assumptions about pure tilt or twist
643 boundary character and errors would be difficult to assess. Use of WBV does not preclude
644 further analysis (e.g. Wieser et al. (2020)) but provides a firm foundation.

645 3.2. Plagioclase: distributed deformation analysis free from slip system assumptions

646 Fig. 10 shows plagioclase from a deformed gabbro from close to the slow spreading mid
647 ocean ridge in the SW Indian Ocean (sample ODP 176-735B-95R-2 from approx. 546 m
648 below the ocean floor). The plagioclase is highly strained, with two prominent ribbons bent
649 around an augite porphyroclast (grey scale on right). Trails of smaller grains are interpreted
650 as new grains due to recrystallization. Hornblende marginal to pyroxene suggests
651 deformation is amphibolite facies, as recorded deeper in the leg (Gardner et al. 2020), but it
652 may have been higher temperature. Our aim here is to not to offer a full interpretation of how
653 the microstructure evolved, but to show how the WBV tools assist in that task.

Figure 10. Example of WBV applied to plagioclase. Figure layout is similar to Fig. 9 but contouring is used to reveal dominant directions. a) IPF map of plagioclase Y direction of a deformed gabbro. Inset shows orientation variation (degrees) from top end of transect marked by white line. The right-hand porphyroclast is augite rimmed by hornblende. b) Key for IPF map colour scheme. c) IPF map of plagioclase as in a), contoured with intervals at 0.1 x uniform. d) Magnitude of WBV calculated on 20 x 20 tiles in area a) superimposed on a band contrast greyscale map. e) IPF map of WBV calculated as in d) colour coded by WBV direction using b), minimum length $0.0005 \mu\text{m}^{-1}$. f) IPF of WBV as in d) and e), contoured in multiples of uniform. g) Magnitude of WBV calculated on 3×3 stencils in white box subarea of map d) superimposed on a band contrast greyscale map. h) IPF map of WBV calculated as in g) colour coded by WBV direction as in b), minimum length $0.01 \mu\text{m}^{-1}$. i) IPF of WBV as in g) and h).

654

655 The IPF Y map (Fig. 10a), colour coded as in 10b)) indicates rather smooth variations in
656 orientation for the large grain, in contrast to the olivine example Fig. 9a). Large tiles used in
657 Fig 10d) confirm this, showing a rather uniform level of distortion on the scale of the tiles
658 through the two ribbons. The WBV IPF map (Fig. 10e)) shows $\langle 100 \rangle$ dominates at the top of
659 the left hand ribbon, whilst $\langle 001 \rangle$ dominates at the bottom, and the IPF (Fig. 10f)) combines
660 these. In and around new grains no data is displayed (Fig. 10d and e) because the 20×20
661 pixel tiles are large enough to cover several small grains and include high ($> 5^\circ$) angle
662 boundaries. Thus, in these areas WBV analysis is not appropriate. It is worth considering
663 whether the apparent variation in WBV direction is a stereological effect, like that shown in
664 Fig. 3h), j). Could the ribbon have a relatively uniform population of GNDs, but with a
665 stereological bias governed by varying orientation? The misorientation from bottom to top of
666 (for example) the left-hand ribbon is about 35° in contrast to Fig. 3h), j) which involved 90°

667 of twist. We conclude it is likely that there are real variations in the GND population in this
 668 grain, which is not surprising given the stretch and non-uniform bending it has enjoyed. Fig
 669 10g)-i) shows WBV calculated using the differential method on a subarea marked with a
 670 white box in Figs. 10d and e. In Fig 10g), boundaries above 5° are shown in black and the
 671 highest distortions i.e. WBV magnitude are shown not in the large ribbons but in small grains
 672 interpreted as products of dynamic recrystallization. Fig. 10h) and i) show WBV direction,
 673 with a pronounced maximum close to $\langle 001 \rangle$ as illustrated by the preponderance of red
 674 colours in new grains in (h) and a contoured maximum near $\langle 001 \rangle$ in (i). The relict ribbon in
 675 centre right of Fig. 10h) shows two left-right tapered zones coloured green, indicating WBV
 676 rather close to $\langle -100 \rangle$ and in accord with the tiling in Fig. 10e).

677 In summary this example shows how the integral (here, tiling) and differential methods may
 678 be used to interrogate different parts of the microstructure. The interiors of the plagioclase
 679 ribbons have relatively low dislocation densities, with GNDs with Burgers vectors combining
 680 $\langle 100 \rangle$ and $\langle 001 \rangle$, likely in different proportions in different parts. Here, the integral method
 681 is a very effective tool. For the small grains, interpreted as recrystallized, the differential
 682 method is helpful; they have higher dislocation densities and various Burgers vectors but with
 683 an emphasis on $\langle 001 \rangle$. In tectonites small grains are often interpreted as new, forming by
 684 static or dynamic recrystallisation from strongly plastically deformed large old grains, and are
 685 relatively strain free. Intriguingly, here the small grains are more distorted than the old
 686 ribbons though normally one would expect them to be relatively strain free. Further WBV
 687 investigation will assist in understanding the evolution of that microstructure. Methods
 688 including the traces of subgrain walls could not be used here, since distortion is distributed;
 689 methods assuming slip systems and dislocation line energies could be applied but the
 690 required inputs may be difficult to constrain in a mineral like plagioclase. As in the olivine
 691 example, we suggest the WBV approach provides a firm foundation on which other analyses
 692 can be built if required.

693 3.3. Ice: investigation of non-basal slip

Figure 11. Example of WBV applied to a subgrain in ice, modified from Fig. 2 of Chauve et al. (2017). WBV is colour coded not by the full IPF but just by the sin of the angle of the WBV from the basal plane, i.e. (component of W parallel to c)/W. This runs between 0 and 1 as shown by the colour scale. Red arrows show the WBV projected onto the map plane, using its actual length not just its direction. Black line is a subgrain wall of 5° or more misorientation.

694

695 There is ongoing research into the role of non-basal slip in ice, since if that is active it will
 696 alter the rheology of ice sheets (Chauve et al. 2017, Piazzolo et al. 2015, Weikusat et al. 2011).
 697 Chauve et al. (2017) undertook deformation experiments on ice and Fig. 11a), modified from
 698 Fig. 2 of that paper, shows a subgrain from an experiment run at -7°C and 0.5 MPa stress.
 699 The WBV is colour coded not by the full IPF but just by the sin of the angle of the WBV
 700 from the basal plane, i.e. (component of W parallel to c)/W. For this dataset we estimate α_{95}
 701 as 32° (Table 1). The yellow vertical subgrain wall indicates angles near 90° from the basal
 702 plane so, even though the errors are large, there is negligible probability that these WBVs lie
 703 in the basal plane. Moreover, the colours along this wall are quite consistent, adding credence
 704 to the diagnosis that the WBV is subparallel to c. It does not immediately imply that

705 individual Burgers vectors are parallel to c : for example, there could be a mixed population of
 706 $c + a$ and $c - a$, bearing in mind the WBV is a vector average. Further data and/or assumptions
 707 are required to determine this. However, as noted above the WBV cannot contain “phantom”
 708 directions: it must be the weighted average of Burgers vectors that are actually present in the
 709 microstructure, and here must include non-basal vectors of some sort. The Figure also
 710 provides an example of WBVs drawn in red as vectors in sample coordinates. As discussed
 711 above and derived in Appendix 1, there is only one such choice at each point, regardless of
 712 crystal symmetry. Despite α_{95} being predicted as 32° , the WBV directions along each wall
 713 segment are quite consistent, suggesting the angular errors are in fact lower, though further
 714 work is required to confirm this.

715 *3.4. Titanite: discovery of new slip system*

716 Fig. 12 shows the use of tiling in a study of deformed titanite, modified from Timms et al.
 717 (2019). The titanite grain is from a shocked granitoid from the Chicxulub impact structure,
 718 Mexico, and the study searched for slip systems activated under extreme stresses, which
 719 would not necessarily correspond to slip systems documented from other settings. The study
 720 included a boundary trace/misorientation approach, but that assumed pure tilt boundaries, so
 721 the WBV method was used for independent verification. The differential method gave a wide
 722 scatter of WBV directions so to reduce errors 20×20 pixel tiles were used. The tiles are
 723 colour coded in terms of IPF direction; missing colours indicate either that the tile includes a
 724 high angle boundary, or the WBV magnitude is below the threshold for display (Table 1).
 725 There are many shock-induced twins, and the abundance of those high angle boundaries
 726 mean that tile coverage is sparse. However, the WBV directions show a strong maximum
 727 near $\langle 341 \rangle$. This is a Burgers vector not previously described in titanite but likely indicating
 728 a dislocation slip system operating concurrently with twinning under shock.

Figure 10. Example of WBV applied to titanite. The greyscale map is of band contrast in a shocked titanite grain and its surroundings, redrawn from Fig. 8 of Timms et al. (2019). Inset shows orientation variation (degrees) from lower left end of transect marked by thick black line. Tiling was used to analyse the microstructure – tiles are coloured for WBV direction in accordance with the IPF key on bottom left. The WBV IPF (top right) shows distinct preferred directions. Calculation and display parameters are given in Table 1.

729

730 *3.5. WBV precision in specific studies*

731 In Table 1 we compile the parameters required for estimating α_{95} from previous studies
 732 making a big assumption, that the orientation measurement errors in those studies are all
 733 distributed uniformly between 0 and 0.01 radians. Despite this, the error estimates are in
 734 general agreement with the appearance of the relevant IPFs. For example, for Mg metal Fig. 7
 735 shows IPFs with α_{95} of 28° and 14° , and those angles are in accord with the scatters of points
 736 if all WBVs are in fact in the basal plane. One large $\alpha_{95} = 110^\circ$ is for quartz and relates to
 737 Fig. 15 of Wheeler et al. (2009), but the left hand IPF there was drawn to specifically
 738 illustrate the effect of choosing a threshold W that is too low. The cone of error would cover
 739 the entire IPF and that is in accord with the random scatter of points seen. In contrast, another
 740 study is predicted to have a large α_{95} of 110° yet the IPFs show strong maxima. Fig. 4 of
 741 Kendrick et al. (2017) shows IPFs of WBV for deformed plagioclase microlites in an andesite
 742 with strong maxima around $[001]$, particularly in the experimentally deformed sample. We

743 suggest this is because there is a single family of GNDs with a single [001] Burgers vector.
744 Then, even though individual WBVs have large errors, the maximum is strong because the
745 errors cancel out to some extent. This is analogous to a standard result in statistics of a single
746 variable: the standard variation of the mean is equal to the standard deviation of an individual
747 measurement divided by the square root of the sample size. A similar idea might be
748 developed for directional statistics in future work.

749 **4. Comparison of WBV with other methods used for analysing GND directional data**

750 All 6 orientation gradients (3 in x and 3 in y) can be calculated from EBSD maps and provide
751 6 constraints on the Nye curvature tensor as in (Pantleon 2008), Wilkinson and Randman
752 (2010), Wallis et al. (2016). If there are 6 types of dislocation, then eqn (3) has a unique
753 solution for 6 GND densities, given the 6 constraints on the Nye tensor. In many materials,
754 particularly cubic phases, symmetry indicates there are more than 6 types of slip system and
755 there is no unique solution for eqn (3). So, an additional assumption is made, that the total
756 line energy of all the dislocations involved is the minimum out of all the possible solutions.

757 This approach uses more information than the WBV method (6 components of the Nye tensor
758 versus 3) but is based on assumptions that we recommend deserve appraisal on a mineral-by-
759 mineral basis.

760 i) Assumptions about allowable slip systems might be misleading as we do not have a
761 complete knowledge of all in all minerals.

762 ii) Assumptions about the line energies of each type of dislocation, to enable overall
763 energy minimisation if there are more than 6 slip systems, will be based on limited
764 information for minerals.

765 iii) Assuming that the types of dislocation related to slip also characterise growth defects
766 deserves scrutiny. For growth the concept of slip systems is not relevant: there might be
767 alternative lists of allowable GND types, but again in minerals such information is scanty.

768 iv) Assuming that dislocations have locally reorganised to minimise their net energy may
769 not be true (e.g. in cold working, or when defects are due to growth).

770

771

772 In contrast WBV calculation makes no assumptions about GND types at any stage of the
773 calculations. Instead, individual studies tailor the interpretation, possibly involving further
774 calculation, based on the problems being addressed. This is well illustrated in the published
775 ice non-basal slip example outlined above. Here, the hypothesis to be tested was to identify if
776 non-basal dislocations are present in ice, tested by calculating and displaying the angle of the
777 WBV to the basal plane (Chauve et al. 2017). The calculation is free from detailed
778 assumptions about dislocation types and energies, which are not well known. A further
779 example is provided in Wieser et al. (2020) who used the trace of subgrain walls together with
780 WBV analysis to provide additional constraints on potential activated slip systems. In this
781 case, additional assumptions were introduced, e.g. that all subgrain walls were either pure tilt
782 or pure twist. Those assumptions are not intrinsic to the WBV calculation. In essence the
783 WBV may provide sufficient information on its own and provides a platform for further in-
784 depth analysis which may use additional assumptions.

785 In a number of works using the “energy minimisation” method, the EBSD data are high
786 resolution electron backscatter diffraction (HREBSD) which gives higher angular accuracy to

787 orientation measurements: for details see Wilkinson and Randman (2010), Wallis et al.
788 (2016) and Wallis et al. (2019a). This means that errors in misorientation gradients and hence
789 WBV or other calculations will be lower than using conventional data (Gardner et al. 2024).
790 However, there is no intrinsic difference in applying WBV or energy minimisation
791 calculations to HREBSD versus conventional data or to data obtained with new techniques
792 e.g. (Winkelmann et al. 2020). WBV can be calculated from HREBSD data, as in Wallis et
793 al. (2016) and Gardner et al. (2024). Equally, best fit/energy minimisation can be used on
794 Hough based orientation data as in Pantleon (2008).

795 **5. Summary and discussion**

796 We have described the theoretical basis for the WBV method and shown examples where it
797 has assisted in deducing Burgers vectors for slip systems in various minerals. Since the
798 method is purely geometric it can also be used to analyse distortions due to growth as in
799 Gardner et al. (2021). Key aspects of the WBV method are as follows.

- 800 • It makes no assumptions about the dislocation populations being investigated.
- 801 • It uses just the three numbers defining orientation at each measurement point, so is fast.
- 802 • It assumes there are no significant grain scale elastic strains.

803 The software we use in this contribution (“Crystalscape”) involves user-defined parameters
804 for calculation as follows; these need to be recorded to allow calculations to be reproduced.

- 805 • The cutoff angle above which boundaries are assumed to no longer have dislocation
806 substructure.
- 807 • The size of the stencil or tile used for systematic calculations.

808 WBV results can be displayed in several ways and the key user-defined parameters for
809 display are the minimum and maximum WBV lengths. The minimum length can then,
810 together with the other parameters, be used to estimate the angular accuracy α_{95} (the shortest
811 vectors being the least accurate in terms of direction). That estimation contains several
812 simplifications and, in any case, depends on an assumed angular error in the EBSD data; but
813 it serves as an indication of accuracy which proves useful.

814 For interpretation, the following properties must be borne in mind.

- 815 • The WBV does *not* measure the complete GND population or density. It is a sample of
816 that population, weighted towards dislocation lines that intersect the EBSD map at high
817 angles. Maps cut in different planes will show different but related WBV information.
- 818 • The WBV is a weighted sum of Burgers vectors of GNDs. In general, there are multiple
819 ways of decomposing the WBV, but it still provides a platform for testing hypotheses. It
820 will never generate “phantom” components. For example, if a trigonal or hexagonal
821 mineral shows WBVs with significant *c* axis components, there must be GNDs with
822 Burgers vectors involving *c* (though not necessarily parallel to *c*).
- 823 • Errors in WBV are smaller when larger stencils or tiles are used. Angular errors are
824 smaller for longer WBVs.
- 825 • Larger stencils or tiles tend to “smear out” the WBV pattern. Increased angular precision
826 is thus linked to reduced spatial resolution.

827 Future directions using this method could include further development of ways to
828 characterise non-basal slip in hexagonal and trigonal materials e.g. Chauve et al. (2017). The
829 combination of WBV analysis with subgrain boundary trace analysis (Wieser et al. 2020) has
830 potential to be developed for olivine and other minerals. More advanced statistical tests
831 related to directional data could be developed. We have not discussed 3D orientation data
832 here but in principle this allows calculation of orientation gradients in all three dimensions
833 and hence the complete Nye tensor which would be valuable for constraining GNDs.
834 However, even the 9 components of the Nye tensor are not sufficient to constrain all GND
835 types in very symmetric minerals. Statistical tests could be developed for 3D analysis as we
836 have done in 2D. Hybrid approaches using two or more maps at right angles also deserve
837 investigation.

838 We note that the methods discussed here are applicable to any crystalline material including
839 metals, ceramics and ice.

840 The Matlab software used for analysis here (“Crystalscape”) is available from the lead author
841 for academic use only. In 2021 Oxford Instruments Nanoanalysis adapted a version of the
842 WBV method for use in Aztec Crystal, their EBSD analysis suite. This is described here:
843 <https://www.ebsd.com/ois-ebsd-system/dislocation-density-analysis> and in a webinar here
844 <https://register.gotowebinar.com/register/5472775566652982031>.

845

846 **Credit author statement**

847 **John Wheeler:** Conceptualization, Software, Writing - Original Draft, Visualization; **Sandra**
848 **Piazolo:** Conceptualization, Writing – Review and Editing; **David Prior:** Conceptualization,
849 Writing – Review and Editing; **Patrick Trimby:** Conceptualization, Resources, Writing –
850 Review and Editing; **Jake Tielke:** Resources, Writing – Review and Editing.

851 **Acknowledgements**

852 We thank all the user of the WBV method who have contributed through discussion to
853 developing the method. We thank Elena Miranda and David Wallis for constructive reviews
854 and Virginia Toy for substantial editorial work.

855

856 Table 1. Details of published WBV studies, and the new studies here

857 Table 1. Published papers using WBV on minerals, with precision estimates added in this
858 contribution. We include one example of use on Mg metal as it helps illustrate the basic
859 ideas. In the right hand columns we have compiled information from the published works to
860 estimate α_{95} based on the assumption that orientation measurement errors are distributed
861 uniformly between 0 and 0.01 radians, a realistic if somewhat pessimistic range for data
862 obtained by Hough transform.

863

Crystal system	Laue group	Phase	weighted Burgers vector study motivation	Reference	Figure in referenced paper	Integral method used?	Stencil or tile	Sampled area (pixels)	Step size (μm)	W minimum length ($(\mu\text{m})^{-1}$)	α_{95} (deg)
Cubic holosymmetric	m3m	Periclase	example	(Wheeler et al. 2009)	Fig 11		s	9	10	0.0015	14.9
Cubic	m3		<i>no studies yet published on minerals</i>	-							-
Hexagonal holosymmetric	6/mmm	Mg	example	(Wheeler et al. 2009)	Fig 3, 5		s	9	4	0.002	28.1
		Mg	example	(Wheeler et al. 2009)			s	9	4	0.004	13.9
		Ti	magnitude display from TKD data	(Trimby et al. 2014)	Fig 5				0.01		n/a
		Ice	search for non-basal dislocations	(Piazolo et al. 2015)			s	9	15	0.0004	37.7
		Ice	search for non-basal dislocations	(Chauve et al. 2017)	Fig. 2		s	9	5	0.0014	32.2
		Ice	intragranular boundary development	(Fan et al. 2022)	Fig. 5		s	9	5	0.006	7.4
Hexagonal	6/m		<i>no studies yet published on minerals</i>	-							-
Trigonal holosymmetric	-3m	Quartz	example	(Wheeler et al. 2009)	Fig 15		s	9	2	0.001	110.0
		Quartz	example	(Wheeler et al. 2009)	Fig 15		s	9	2	0.003	37.7
		Quartz	compare GND density with density from etch pits	(Billia et al. 2013)	n/a	y					n/a
		Calcite	deduce slip systems hence deformation T	(Mcnamara et al. 2020)	Fig 4, 5						
Trigonal	-3		<i>no studies yet published on minerals</i>	-							
Tetragonal holosymmetric	4/mmm	Zircon	Link magnitude to Pb loss	(MacDonald et al. 2013)	Fig. 9	y			1, 2, 0.8		n/a
		Zircon	Planar deformation bands	(Kovaleva et al. 2015)	Fig. 6	y					n/a
		Zircon	help to characterise slip systems	(Kovaleva et al. 2018)	Fig. 6	y					n/a
Tetragonal	4/m		<i>no studies yet published on minerals</i>	-						-	
Orthorhombic	mmm	Olivine	confirm slip systems dominated by [100]	(Tielke et al. 2019)	Fig. 5 b	y	s	9	3	0.005	14.9
		Olivine	determine slip systems	(Wieser et al. 2020)	Fig. 4, 7						
		Olivine	tiling example	<i>this contribution</i>	Fig. 7	y	t	100	16	0.00005	26.2
		Olivine	stencil example	<i>this contribution</i>	Fig. 7		s	9	16	0.001	13.9
Monoclinic	2/m	Titanite	Diagnose slip systems: map showing WBV direction (6 μm tiles)	(Timms et al. 2019)	Fig. 8c		t	400	0.3	0.001	24.6
		Titanite	Contoured IPF showing WBV direction (2.4 μm tiles)	(Timms et al. 2019)	Fig. 8e		t	64	0.3	0.003	32.6
Triclinic	-1	Plagioclase	Diagnose slip system in naturally and experimentally deformed microlites; latter show [001] clearly; both show it in loops	(Kendrick et al. 2017)	Fig. 4		s	9	0.2	0.01	110.0
		Plagioclase	Understand plagioclase replacement by albite	(Gardner et al. 2021)	Fig. 6		s				
		Plagioclase	tiling example	<i>this contribution</i>	Fig. 8	y	t	400	1	0.0005	14.7
		Plagioclase	stencil example	<i>this contribution</i>	Fig. 8		s	21	1	0.01	9.5

References

- Ashby, M. F. 1970. Deformation of plastically non-homogeneous materials. *Philosophical Magazine* **21**(170), 399-424.
- Billia, M. A., Timms, N. E., Toy, V. G., Hart, R. D. & Prior, D. J. 2013. Grain boundary dissolution porosity in quartzofeldspathic ultramylonites: Implications for permeability enhancement and weakening of mid-crustal shear zones. *Journal Of Structural Geology* **53**, 2-14.
- Butler, R. F. 1992. *Paleomagnetism: Magnetic Domains to Geologic Terranes*. Blackwell Scientific Publications.
- Chauve, T., Montagnat, M., Piazzolo, S., Journaux, B., Wheeler, J., Barou, F., Mainprice, D. & Tommasi, A. 2017. Non-basal dislocations should be accounted for in simulating ice mass flow. *Earth And Planetary Science Letters* **473**, 247-255.
- Das, S., Hofmann, F. & Tarleton, E. 2018. Consistent determination of geometrically necessary dislocation density from simulations and experiments. *International Journal Of Plasticity* **109**, 18-42.
- De Graef, M. 2020. A dictionary indexing approach for EBSD. *IOP Conference Series: Materials Science and Engineering* **891**, 012009.
- Drury, M. R. & Urai, J. L. 1990. Deformation related recrystallization processes. *Tectonophysics* **172**, 235-253.
- Fan, S., Wheeler, J., Prior, D. J., Negrini, M., Cross, A. J., Hager, T. F., Goldsby, D. L. & Wallis, D. 2022. Using misorientation and weighted Burgers vector statistics to understand intragranular boundary development and grain boundary formation at high temperatures. *Journal of Geophysical Research - Solid Earth* **127**(8), 26 pages.
- Gardner, J., Wallis, D., Hansen, L. N. & Wheeler, J. 2024. Weighted Burgers Vector analysis of orientation fields from high-angular resolution electron backscatter diffraction. *Ultramicroscopy* **257**, 113893.
- Gardner, J., Wheeler, J. & Mariani, E. 2021. Interactions between deformation and dissolution-precipitation reactions in feldspar at greenschist facies. *Lithos* **396-397**.
- Gardner, R. L., Piazzolo, S., Daczko, N. R. & Trimby, P. 2020. Microstructures reveal multistage melt present strain localisation in mid-ocean gabbros. *Lithos* **366**.
- Guillopé, M. & Poirier, J. P. 1979. Dynamic recrystallization during creep of single-crystal halite: an experimental study. *Journal of Geophysical Research* **84**, 5557-5567.
- Hildyard, R. C., Prior, D. J., Faulkner, D. R. & Mariani, E. 2009. Microstructural analysis of anhydrite rocks from the Triassic Evaporites, Umbria-Marche Apennines, Central Italy: An insight into deformation mechanisms and possible slip systems. *Journal Of Structural Geology* **31**(1), 92-103.
- Jiang, J., Britton, T. B. & Wilkinson, A. J. 2013. Measurement of geometrically necessary dislocation density with high resolution electron backscatter diffraction: Effects of detector binning and step size. *Ultramicroscopy* **125**, 1-9.
- Kalácska, S., Dankházi, Z., Zilahi, G., Maeder, X., Michler, J., Ispánovity, P. D. & Groma, I. 2020. Investigation of geometrically necessary dislocation structures in compressed Cu micropillars by 3-dimensional HR-EBSD. *Materials Science and Engineering: A* **770**, 138499.
- Kendrick, J. E., Lavalley, Y., Mariani, E., Dingwell, D. B., Wheeler, J. & Varley, N. R. 2017. Crystal plasticity as a strain marker of the viscous-brittle transition in magmas. *Nature Communications* **8**(1), Art. No. 1926.
- Konijnenberg, P. J., Zaeferrer, S. & Raabe, D. 2015. Assessment of geometrically necessary dislocation levels derived by 3D EBSD. *Acta Materialia* **99**, 402-414.
- Kovaleva, E., Klotzli, U., Habler, G. & Wheeler, J. 2015. Planar microstructures in zircon from paleo-seismic zones. *American Mineralogist*.

- Kovaleva, E., Klotzli, U., Wheeler, J. & Habler, G. 2018. Mechanisms of strain accommodation in plastically-deformed zircon under simple shear deformation conditions during amphibolite-facies metamorphism. *Journal Of Structural Geology* **107**, 12-24.
- Kuhr, B. & Farkas, D. 2019. Dislocation content in random high angle grain boundaries. *Modelling and Simulation in Materials Science and Engineering* **27**(4), 045005.
- Lloyd, G. E. 2002. Microstructural evolution in a mylonitic quartz simple shear zone: the significant roles of dauphine twinning and misorientation. In: *Joint International Meeting of the Tectonic-Studies-Group of the Geological-Society London/Structural Geology and Tectonics Division of the Geological-Society-of-America/Geological-Society-of-Australia. Geological Society Special Publication* **224**, London, ENGLAND, 39-61.
- MacDonald, J. M., Wheeler, J., Harley, S. L., Mariani, E., Goodenough, K. M., Crowley, Q. G. & Tatham, D. 2013. Lattice distortion in a zircon population and its effects on trace element mobility and U–Th–Pb isotope systematics: examples from the Lewisian Gneiss Complex, northwest Scotland. *Contributions To Mineralogy And Petrology* **166**, 21-41.
- Mamtani, M. A., Reznik, B. & Kontny, A. 2020. Intracrystalline deformation and nanotectonic processes in magnetite from a naturally deformed rock. *Journal of Structural Geology* **135**, 104045.
- Marquardt, K. & Faul, U. H. 2018. The structure and composition of olivine grain boundaries: 40 years of studies, status and current developments. *Physics and Chemistry of Minerals* **45**(2), 139-172.
- Mcnamara, D. D., Lister, A., Prior, D. J., Scully, A., Gardner, J. & Wheeler, J. 2020. Microanalysis of Calcite Scaling in a Fractured Geothermal System.
- Nicolay, A., Franchet, J. M., Cormier, J., Mansour, H., De Graef, M., Seret, A. & Bozzolo, N. 2019. Discrimination of dynamically and post-dynamically recrystallized grains based on EBSD data: application to Inconel 718. *JOURNAL OF MICROSCOPY* **273**(2), 135-147.
- Nye, J. F. 1953. Some geometrical relations in dislocated crystals. *Acta Metallurgica* **1**, 153-162.
- Pantleon, W. 2008. Resolving the geometrically necessary dislocation content by conventional electron backscattering diffraction. *Scripta Materialia* **58**(11), 994-997.
- Piazolo, S., Montagnat, M., Grennerat, F., Moulinec, H. & Wheeler, J. 2015. Effect of local stress heterogeneities on dislocation fields: Examples from transient creep in polycrystalline ice. *Acta Materialia* **90**, 303-309.
- Poirier, J. P. & Nicolas, A. 1975. Deformation-induced recrystallization due to progressive misorientation of subgrains, with special reference to mantle peridotites. *Journal of Geology* **83**, 707-720.
- Prior, D. J. 1999. Problems in determining the orientations of crystal misorientation axes, for small angular misorientations, using electron backscatter diffraction in the SEM. *Journal of Microscopy* **195**, 217-225.
- Prior, D. J., Mariani, E. & Wheeler, J. 2009. EBSD in the Earth Sciences: applications, common practice and challenges. In: *Electron Backscatter Diffraction in Materials Science* (edited by Schwartz, A. J., Kumar, M., Adams, B. L. & Field, D. P.). Springer, 345-357.
- Ram, F., Zaefferer, S., Japel, T. & Raabe, D. 2015. Error analysis of the crystal orientations and disorientations obtained by the classical electron backscatter diffraction technique. *Journal of Applied Crystallography* **48**(3), 797-813.
- Shigematsu, N., Prior, D. J. & Wheeler, J. 2006. First combined electron backscatter diffraction and transmission electron microscopy study of grain boundary structure of deformed quartzite *Journal of Microscopy* **224**, 306-321.
- Spruzeniece, L., Piazolo, S. & Maynard-Casely, H. E. 2017. Deformation-resembling microstructure created by fluid-mediated dissolution-precipitation reactions. *Nature Communications* **8**.
- Sutton, A. P. & Balluffi, R. W. 1995. *Interfaces in crystalline materials*. Clarendon Press, Oxford.

- Tielke, J. A., Mecklenburgh, J., Mariani, E. & Wheeler, J. 2019. The influence of water on the strength of olivine dislocation slip systems. *Journal Of Geophysical Research: Solid Earth* **124**, 6542-6559.
- Tielke, J. A., Zimmerman, M. E. & Kohlstedt, D. L. 2017. Hydrolytic weakening in olivine single crystals. *Journal of Geophysical Research-Solid Earth* **122**(5), 3465-3479.
- Timms, N. E., Pearce, M. A., Erickson, T. M., Cavosie, A. J., Rae, A., Wheeler, J., Wittman, A., Ferriere, F., Poelchau, M. H., Tomioka, N., Collins, G. S., Gulick, S. P. S., Rasmussen, C., Morgan, J. V. & Scientists, I.-I. E. 2019. New shock microstructures in titanite (CaTiSiO₅) from the peak ring of the Chicxulub impact structure, Mexico. *Contributions To Mineralogy And Petrology*.
- Timms, N. E., Reddy, S. M., Healy, D., Nemchin, A. A., Grange, M. L., Pidgeon, R. T. & Hart, R. 2012. Resolution of impact-related microstructures in lunar zircon: A shock-deformation mechanism map. *Meteoritics & Planetary Science* **47**(1), 120-141.
- Trimby, P. W., Cao, Y., Chen, Z., Han, S., Hemker, K. J., Lian, J., Liao, X., Rottmann, P., Samudrala, S., Sun, J., Wang, J. T., Wheeler, J. & Cairney, J. M. 2014. Characterizing deformed ultrafine-grained and nanocrystalline materials using transmission Kikuchi diffraction in a scanning electron microscope. *Acta Materialia* **62**, 69-80.
- Trimby, P. W., Prior, D. J. & Wheeler, J. 1998. Grain boundary hierarchy development in a quartz mylonite. *Journal of Structural Geology* **20**, 917-935.
- Wallis, D., Hansen, L. N., Ben Britton, T. & Wilkinson, A. J. 2016. Geometrically necessary dislocation densities in olivine obtained using high-angular resolution electron backscatter diffraction. *Ultramicroscopy* **168**, 34-45.
- Wallis, D., Hansen, L. N., Britton, T. B. & Wilkinson, A. J. 2019a. High-Angular Resolution Electron Backscatter Diffraction as a New Tool for Mapping Lattice Distortion in Geological Minerals. *Journal of Geophysical Research: Solid Earth* **124**, 6337–6358.
- Wallis, D., Parsons, A. J. & Hansen, L. N. 2019b. Quantifying geometrically necessary dislocations in quartz using HR-EBSD: Application to chessboard subgrain boundaries. *Journal of Structural Geology* **125**, 235-247.
- Weikusat, I., Miyamoto, A., Faria, S. H., Kipfstuhl, S., Azuma, N. & Hondoh, T. 2011. Subgrain boundaries in Antarctic ice quantified by X-ray Laue diffraction. *Journal of Glaciology* **57**(201), 111-120.
- Wheeler, J., Mariani, E., Piazzolo, S., Prior, D. J., Trimby, P. & Drury, M. R. 2009. The weighted Burgers vector: a new quantity for constraining dislocation densities and types using Electron Backscatter Diffraction on 2D sections through crystalline materials. *Journal of Microscopy* **233**(3), 482-494.
- White, S. 1976. The effects of strain on the microstructures, fabrics, and deformation mechanisms in quartzites. *Philosophical Transactions of the Royal Society of London A* **283**, 69-86.
- Wieser, P., Edmonds, M., Maclennan, J. & Wheeler, J. 2020. The Record of Magma Storage under Kīlauea Volcano preserved in Distorted Olivine Crystals. *Nature Communications*.
- Wilkinson, A. J. & Randman, D. 2010. Determination of elastic strain fields and geometrically necessary dislocation distributions near nanoindentations using electron back scatter diffraction. *Philosophical Magazine* **90**(9), 1159-1177.
- Winkelmann, A., Nolze, G., Cios, G., Tokarski, T. & Bała, P. 2020. Refined Calibration Model for Improving the Orientation Precision of Electron Backscatter Diffraction Maps. *Materials* **13**(12), 2816.
- Wirth, R. 1996. Thin amorphous films (1–2 nm) at olivine grain boundaries in mantle xenoliths from San Carlos, Arizona. *Contributions to Mineralogy and Petrology* **124**(1), 44-54.
- Zhang, Z., Ódor, É., Farkas, D., Jóni, B., Ribárik, G., Tichy, G., Nandam, S.-H., Ivanisenko, J., Preuss, M. & Ungár, T. 2020. Dislocations in Grain Boundary Regions: The Origin of Heterogeneous Microstrains in Nanocrystalline Materials. *Metallurgical and Materials Transactions A* **51**(1), 513-530.

For submission to Journal of Structural Geology

Using crystal-lattice distortion data for geological investigations: the weighted Burgers vector method

J. Wheeler¹, S. Piazzolo², D. J. Prior³, P. W. Trimby⁴ and J. A. Tielke⁵

¹Department of Earth, Ocean, and Ecological Sciences, University of Liverpool, 4 Brownlow Street, Liverpool, L69 3GP, UK

²University of Leeds, School of Earth & Environment, Leeds LS2 9JT, UK

³Department of Geology, University of Otago, Dunedin, New Zealand

⁴Oxford Instruments Nanoanalysis, High Wycombe, Bucks, England

⁵Lamont-Doherty Earth Observatory of Columbia University, Palisades, NY, USA

Abstract

Distorted crystals carry useful information on processes involved in their formation, deformation and growth. The distortions are accommodated by geometrically necessary dislocations, and therefore characterising those dislocations is an informative task, to assist in, for example, deducing the slip systems that produced the dislocations. Electron backscatter diffraction (EBSD) allows detailed quantification of distorted crystals and we summarise here a method for extracting information on dislocations from such data. The weighted Burgers vector (WBV) method calculates a vector at each point on an EBSD map, or an average over a region. The vector is a weighted average of the Burgers vectors of dislocation lines intersecting the map surface. It is weighted towards dislocation lines at a high angle to the map but that can be accounted for in interpretation. The method is fast and does not involve specific assumptions about dislocation types; it assumes only that elastic strains have little effect on the calculation. It can be used, with care, to analyse subgrain walls (sharp orientation changes) as well as gradational orientation changes within individual grains. There are four linked parts to this contribution.

1. We describe the mathematical background to the WBV and then how it is modified to deal with spaced, discrete orientation measurements.
2. EBSD orientation data have angular errors, and so does the WBV. We present a new analysis of these angular errors, showing there is a trade-off between directional accuracy and area sampled. Angular errors can now be accounted for during testing of hypotheses about dislocation types.
3. We present new studies on olivine and plagioclase to illustrate how to use the method.
4. We discuss published studies on ice and titanite to further illustrate the method.

We note that the methods discussed here are applicable to any crystalline material encompassing minerals (including ice), metals and ceramics.

Keywords

Electron Backscatter Diffraction; Geometrically Necessary Dislocations; Slip Systems; Intracrystalline Distortion; weighted Burgers vector; Olivine; Plagioclase; Ice; Titanite

1. Introduction

Microstructures are crucial indicators of processes that have affected rocks. Dislocations provide evidence for how and under what conditions individual grains have deformed or they may be growth defects indicating growth conditions. Regardless of their origin dislocations give rise to *distortion* in a crystal lattice on some scale, and we advocate use of this word as a non-genetic description of their geometric effects. If dislocations are due to deformation their Burgers vectors may help constrain the style or conditions of deformation. Individual dislocations give a lattice extra energy, so the density of dislocations is needed to estimate this on a volumetric basis. This plastic strain energy provides a driving force for recrystallization in deformed rocks (Drury & Urai 1990). TEM is the standard method to image individual dislocations, a procedure that can be laborious and will characterise just a tiny fraction of the microstructure, leaving doubts as to how representative it is. In contrast intracrystalline distortions may be optically visible and can be quickly characterised by EBSD mapping over large regions. Such distortions, regardless of cause, must be accommodated by geometrically necessary dislocations (GNDs) (Ashby 1970) and hence give indirect information on dislocation content.

The GND concept complements the statistically stored dislocation (SSD) concept. The dislocations involved are not fundamentally different types; instead, these are scale dependent ideas. Lattice curvature over a particular length scale is by definition accommodated by GNDs *at that scale*. Over that length scale there may be other dislocations for example of opposite signs, that cancel out each other's local curvature effects (though still contribute to plastic strain energy and other relevant properties): these are SSDs. Zooming in to a smaller length scale may reveal local lattice curvatures related to what were classified as SSDs. At this smaller length scale some SSDs are now GNDs. If one examines lattice curvature on the atomic scale, all dislocations would be classified as GNDs. In relation to EBSD, the relevant length scale is the step size. So lattice curvature shown on EBSD maps relates to GNDs on the scale of the step size. SSDs will, by definition, not leave a fingerprint on the curvature. A smaller step size will reveal more GNDs. Very small step sizes can reveal individual dislocations (<https://www.ebsd.com/ois-ebsd-system/dislocation-density-analysis>).

It would be useful to constrain *directional* (lines, Burgers vectors) and *magnitude* (dislocation density) GND information from EBSD data: examples of approaches follow. If distortion is due to deformation by dislocation motion it can in principle be used to constrain active slip systems (hence deformation conditions) using directional information. Based on geometric assumptions alone, such studies have often focussed on subgrain walls (in essence, localised sharp distortions). For example Lloyd (2002) argues that subgrain walls traces and misorientation axes in quartz can be used to deduce slip systems, though assumptions about "pure" tilt or twist nature of boundaries are needed. Wieser et al. (2020) applied a modified approach to olivine, incorporating subgrain wall traces with information from the method of Wheeler et al. (2009). The latter, the weighted Burgers vector (WBV) method, is what we discuss in this contribution. In minerals with multiple slip systems, distortion cannot be uniquely linked to slip systems using geometry alone. Calculations can then be made assuming that the net dislocation energy is minimised with respect to all possible combinations of dislocation lines and Burgers vectors for example in quartz (Wallis et al. 2019b). Distortion magnitudes can be quantified using for example "local misorientation" though the link to actual dislocation densities is not straightforward to make. For example

84 Timms et al. (2012) use local misorientation maps to give an overview of the heterogeneous
85 distortion in shocked zircon crystals.

86 If distortion is due to growth, or is postulated to be, then purely geometric analyses can be
87 applied as they would be to deformed crystals but any extra assumptions must be evaluated
88 with care. Spruzeniece et al. (2017) quantified crystal distortions in KBr-KCl solid solution
89 grown in a stress-free environment: these are due to growth not deformation. Gardner et al.
90 (2021) examined natural distorted albite and showed that some subgrain walls contain
91 dislocations with Burgers vectors with $\langle 010 \rangle$ components. There are no known slip systems
92 with such Burgers vectors, so the subgrain walls were diagnosed as growth defects.

93 The methods in these and many other papers using EBSD to analyse distortions include
94 various assumptions, both in manual processes (e.g. selecting straight segments of boundary
95 traces) and in automatic calculations (e.g. assumptions about allowed slip systems and
96 dislocation energy minimisation). It is generally not clear how errors in EBSD orientation
97 measurements affect deductions: specifically, here we address *angular* errors although
98 *magnitude* errors are relevant (e.g. Jiang et al. (2013) ~~Jiang~~). Some methods are slow if they
99 are manual or compute intensive, a relevant consideration in terms of time versus benefit.
100 Methods using boundary trace analysis cannot be applied to smooth, distributed distortions
101 because there are no discrete boundaries. Overall, the methods to date have diverse strengths
102 and weaknesses.

103 Our overall aim here is to review and extend the WBV method for extracting information on
104 GNDs from EBSD data, based on our experience of how it has been used since first
105 publication in 2009. By clarifying and enhancing the insights it can give we hope to
106 encourage its use in future studies. In this contribution we summarise the WBV method for
107 extracting information on GNDs from EBSD data. There are four linked aims.

- 108 1. A description of the theoretical basis based on existing understanding (sections 2.1-
109 2.3) but using new illustrative models. We explain the method using model distorted
110 crystals, with mathematical details in Supplementary Information. We discuss how
111 the method applies to smoothly curved lattices and to subgrain walls (where GNDs
112 are collected into surfaces of negligible width). The aim here is to ensure users of the
113 method understand its advantages and limitations.
- 114 2. New analysis of the errors (specifically angular errors) inherent in the calculation, so
115 that hypotheses about microstructural evolution can be tested robustly (section 2.4).
- 116 3. New examples of application of the method (sections 3.1 olivine and 3.2 plagioclase)
117 to assist in understanding how it works in practice.
- 118 4. Review of implications for previous studies in section 3.5 (Table 1), with some detail
119 in 3.3 ice and 3.4 titanite.

120 Finally, we discuss this method in relation to others used to analyse intracrystalline distortion
121 and suggest future developments. We note that the methods discussed here are applicable to
122 any crystalline material encompassing minerals (including ice), metals and ceramics.

123 2. The WBV method: background and error analysis

124 The method gives information on combinations of GND Burgers vectors and GND densities,
125 so we now discuss these two concepts. Imagine a closed loop joining atoms (or unit cells)
126 around a dislocation in “sample coordinates” (Fig. 1a, c). ~~in “sample coordinates”~~. Now

Formatted: Not Highlight

127 move the atoms to the positions they would have in an undistorted crystal: the Burgers vector
 128 is the gap opened up in the previously closed loop (red arrows in Fig. 1b, d) in “crystal
 129 coordinates”). It can be described in crystal coordinates (hence dimensionless, for example
 130 [100] for the edge and [001] for the screw) or in sample coordinates (dimensions of length;
 131 direction depends on sample orientation). Dislocation density is a phrase that is used in
 132 different ways. It may refer to the total line length of SSDs in a unit volume. Not all of these
 133 give rise to lattice curvature so here we consider only the total line length of GNDs per unit
 134 volume. We illustrate the basic ideas using a 2D model first.

Fig. 1. a) A closed loop around an edge dislocation in sample space, view down along the dislocation line. b) The same path traced out in crystal coordinates, showing a gap that is the definition of the Burgers vector (red) of the dislocation within the loop. c), d) The same for a screw dislocation; the dislocation line is parallel to the Burgers vector.

135

136 2.1. Concepts in 2D

137 GND density relates to lattice curvature and a 2D description illustrates this most simply,
 138 where there is no distortion in the z or [001] direction. We show here how curvature relates to
 139 single then multiple dislocation populations. Figure 2 shows lattice orientations in a 2D
 140 model which can, at each point, be described by a single number (angle θ of a particular
 141 lattice direction anticlockwise from a reference direction). In 2D all dislocations have edge
 142 character and in the Figure the Burgers vectors are defined as one atomic spacing so $\mathbf{b} =$
 143 [100]. The four frames show increasing dislocation density ρ , defined in 2D as the number of
 144 dislocations per unit area, and the corresponding increase in lattice curvature. The irregular
 145 spacing of dislocations means this model is an approximate illustration but provides a basis
 146 for understanding.

147

Figure 2. Visualization of the link between GND density (chosen here as edge dislocations all the same sign) and lattice curvature. The crystallographic “z” direction [001] is chosen as out of the page so the dislocations illustrated have line vector [001] and Burgers vector [100]. Angle θ , dependent on position, shows orientation of a lattice direction relative to a reference direction (thick line).

148

149 EBSD measurements do not pick out individual atoms but provide orientation θ as a defined
 150 function of position (in 2D, $\theta(x, y)$); that is what we must work with. Lattice curvature is
 151 defined by variations in θ in the x and/or y directions. The lattice curvature is then a vector

$$152 \quad \boldsymbol{\kappa} = - \left(\frac{\partial \theta}{\partial x}, \frac{\partial \theta}{\partial y} \right) \quad (1)$$

153 (see Appendix 2.1 for details). There is one key assumption made when using the WBV
 154 method: that elastic strains have a relatively small effect. If EBSD records lattice curvature,
 155 then that could in principle be caused by elastic strain. As EBSD cannot generally image
 156 individual dislocations, an EBSD map of (for example) Fig. 2 could look identical to a map
 157 of a perfect lattice with no GNDs, elastically bent. However, as was argued in Wheeler et al.

158 (2009), in the microstructures we have studied, curvature is often localized along sub-grain
 159 walls and we cannot conceive of elastic strain being localized in this way. Secondly, we
 160 would expect elastic bending in a wide variety of orientations in a polycrystal, giving rise to a
 161 wide variety of (illusory) WBVs. Instead, we see systematic patterns as exhibited in the case
 162 studies we present here, and in most of the published studies (Table 1). Wallis et al. (2019a)
 163 find that “often the rotation gradients are larger than the elastic strain gradients ... in which
 164 case, the elastic strain gradients can be neglected”.

165 From now on we will assume no elastic strains and, in that case, κ relates to a single
 166 population of GNDs by

$$167 \quad \kappa = \rho \mathbf{b}$$

168 that incorporates the fact that in sample coordinates, \mathbf{b} may vary even if it is a single
 169 crystallographic direction. Considering just the magnitudes, we can write this as

$$170 \quad (\text{curvature}) = (\text{dislocation density}) \times (\text{Burgers vector length})$$

171 which is a starting point for understanding the link between curvature and dislocation density.
 172 If there is more than one type of dislocation (each with different Burgers vectors and
 173 densities)

$$174 \quad \kappa = \sum_N \rho^{(N)} \mathbf{b}^{(N)} \quad (2)$$

175 where ρ and \mathbf{b} are the density and Burgers vectors *for each type* (superscript N) of
 176 dislocation. If there were just 2 types of dislocation, this equation would yield their densities
 177 uniquely. If more than 2 types are present then the densities are non-unique, but the equation
 178 still provides constraints. Such issues are relevant for 3D which we now discuss.

179 2.2. Concepts in 3D

180 In 3D we require three numbers to define a lattice orientation (e.g. conventionally three Euler
 181 angles, although other representations are available), and we have three directions in which to
 182 evaluate gradients, there are 9 gradients to consider. Nye (1953) showed how curvature is
 183 then a second rank tensor, but a more direct link to dislocation density (line length per unit
 184 volume in 3D) is established via a tensor α (which now carries his name), also a function of
 185 orientation gradients. This links to dislocation density as follows.

$$186 \quad \alpha_{i\gamma} = \sum_N \rho^{(N)} b_i^{(N)} l_\gamma^{(N)} \quad (3)$$

187 where ρ , \mathbf{b} and \mathbf{l} are the density, Burgers vector and unit line vector for each type (labelled N)
 188 of dislocation. Note the close resemblance to eqn 2, but with the extension to include
 189 dislocation line vectors. When there are many types of dislocation, there may be multiple
 190 combinations giving a particular Nye tensor. Note the following.

- 191 • This has to be written in terms of vectors and tensors, since the situation is 3D.
- 192 • Such equations are best written using index notation which makes explicit whether
- 193 vectors are expressed in crystal coordinates (Latin subscript for b_i) or sample coordinates
- 194 (Greek subscript for l_γ), for reasons explained in Wheeler et al. (2009) and Das et al.
- 195 (2018).

- 196 • α is sometimes called “dislocation density” but must be distinguished from other uses of
197 the same phrase.

198 Determining the full Nye tensor requires orientation gradients in all three directions.
199 Although there are GND studies using 3D EBSD from serial focussed ion beam milling e.g.
200 (Kalácska et al. 2020, Konijnenberg et al. 2015) these are challenging and generally EBSD is
201 conducted on 2D sections. Wheeler et al. (2009) showed that relevant (though incomplete)
202 information could still be extracted from a 2D map. Specifically, of the 9 components of the
203 Nye tensor, a 3-component vector can be calculated. The vector is a sum of Burgers vectors
204 of GNDs, *weighted* by the actual dislocation density of each type of GND and by the angle
205 between the dislocation lines and the map. Lines at a high angle to the map are favoured
206 because the mathematics involves multiplying the true density by $\sin(\text{angle between}$
207 $\text{dislocation line and map})$. The phrase “weighted Burgers vector” (WBV) was used, to make
208 clear that this vector is a weighted “sample” of the Nye tensor.

$$209 \quad W_i = \alpha_{i3} = \sum_N \rho^{(N)} b_i^{(N)} l_3^{(N)} = \sum_N \left[\rho^{(N)} l_3^{(N)} \right] b_i^{(N)} \quad (4)$$

210 where \mathbf{W} is the WBV, and the subscript “3” refers to the z direction, perpendicular to the
211 map, so l_3 is the component of a dislocation line vector perpendicular to the map: it varies
212 from 0 (lines parallel to map) to 1 (lines perpendicular to map). The terms in square brackets
213 are scalars, so note that the WBV is a linear combination of Burgers vectors – this is one
214 reasons why it is a useful quantity. The WBV has units of $(\text{length})^{-1}$ and we recommend using
215 the convenient it is convenient to use units of $(\mu\text{m})^{-1}$. We denote its magnitude as W . It can
216 be expressed in crystal coordinates as in eqn (4), or in sample coordinates by calculating $\mathbf{h}\mathbf{W}$
217 where \mathbf{h} is the orientation tensor (a function of Euler angles). It might appear that this will
218 give a non-unique answer for the vector in sample coordinates, since \mathbf{W} has symmetric
219 variants in crystal coordinates, but Appendix 1 shows this is not the case – there is a unique
220 WBV in sample coordinates.

221 There are two approaches to calculating \mathbf{W} , differential and integral. The differential method
222 involves evaluating local gradients in \mathbf{h} around the point at which \mathbf{W} is required. Since that
223 point has a specific orientation, \mathbf{W} can be expressed in crystal or sample coordinates. The
224 integral method involves integrating round a closed loop on the map to obtain the *net* or
225 *average* Burgers vector content of the GND lines intersecting the map inside the loop,
226 expressed in crystal coordinates. The mathematics in essence defines the loop in sample
227 coordinates (c.f. Fig. 1a) black arrows), transforms each loop segment (black arrow) into
228 crystal coordinates (c.f. Fig. 1b) black arrows), and sums up the segments in crystal
229 coordinates to give the net Burgers vector (red arrow). Unlike the differential method, there is
230 no strict way to express the vector in sample coordinates because orientation varies around
231 and within the loop and the result of the integral method is not linked to any particular point
232 within the loop. However, as we discuss below, for the calculation to be meaningful there
233 should be no “high angle” grain boundaries (HAGBs) (which do not usually have organised
234 dislocation substructures) large orientation variations around intersected by the loop. If the
235 loop crosses HAGBs then the calculation will still return a vector, but that will not give clear
236 information on dislocations. There is no systematic knowledge of or agreement on what
237 constitutes an HAGB and we usually pick 5 degrees as a maximum angle: see, discussed
238 further in section 2.2.5. In that case the orientation at, for example, the loop centroid could be

~~used to convert from crystal to sample coordinates. If orientation variations include “high angle” grain boundaries (HAGBs) which do not have organised dislocation substructures then the calculation will still return a vector but it will not give information on dislocations. Unlike the differential method, there is no strict way to express the vector in sample coordinates because orientation varies around and within the loop and the result of the integral method is not linked to any specific point within the loop. In However, if the loop does not include HAGBs then orientation variations in the loop are small that ease and the orientation at, for example, the loop centroid could be used to convert from crystal to sample coordinates. There is no systematic knowledge of or agreement on what constitutes an HAGB and we usually pick 5 degrees as a maximum angle; see section 2.2.5.~~

If the orientation \mathbf{h} is a defined mathematical function of position, then the methods are identical (they are related by Stokes’ theorem). In practice \mathbf{h} is defined at discrete measurement points, e.g. on a square grid. The differential method then involves numerical estimation of orientation gradients, with some flexibility in terms of the number of points used. The integral method involves numerical integration around the closed loop. As we will show later (section 2.3), the methods have different advantages in practice.

2.2.1. WBV, lattice vectors and Burgers vectors

In this section we discuss the links between WBV and Burgers vectors and show how there may be unique or non-unique relationships. In the approach we describe here, the “differential” values of WBV are usually expressed in units of $(\mu\text{m})^{-1}$. In crystal coordinates \mathbf{W} can be decomposed into lattice basis vectors \mathbf{L} if needed

$$\mathbf{W} = K_1\mathbf{L}_1 + K_2\mathbf{L}_2 + K_3\mathbf{L}_3 \quad (5)$$

where the coefficients K are in units of $(\text{length})^{-2}$. These coefficients *resemble* dislocation densities but are in general different. This decomposition relates to the GND types and densities and is unique but further assumptions are needed to express it in terms of the Burgers vectors of actual slip systems. For example, in olivine, slips systems have Burgers vectors that are either [100] or [001]. If we find that \mathbf{W} is parallel to [203] and we know the distortion is due to crystal plasticity then we can deduce that it shows a combination of slip systems with [100] and [001] Burgers vectors. The magnitude of \mathbf{W} parallel to [100] would then, in accord with eqn. (4), be a weighted sum of the dislocation densities of all types of dislocation with [100] Burgers vectors. In anhydrite, also orthorhombic, slip systems can involve [001], [1-1-2] and [11-2] Burgers vectors (Hildyard et al. 2009). There is a unique way to express the three components of \mathbf{W} in terms of those three vectors, if those vectors are linearly independent: in this example $[203] = 7[001] + [1-1-2] + [11-2]$. However, many crystals have more than three Burgers vectors for possible slip systems, especially in more symmetric crystals counting all symmetric variants. For example, in a trigonal phase such as calcite, there will be at least 3 Burgers vectors in the basal plane. Any two of these can be combined to give the basal plane component of \mathbf{W} , so the decomposition is non-unique. \mathbf{W} still carries valuable information on the relative contributions of dislocations with basal and non-basal Burgers vectors (Chauve et al. 2017). Our philosophy here is that the methods give the value of \mathbf{W} , and if further assumptions are required (in terms of expected slip systems, relative energies etc.) these should be made on a case-by-case basis. The K coefficients can be related to GND densities using further information such as the specific Burgers vectors of GNDs.

283 Except for angular errors which are discussed later, it is crucial to note that the WBV cannot
 284 generate “phantom” directions: it must be the weighted average of Burgers vectors that are
 285 actually present in the microstructure. For example, regardless of mineral symmetry, if \mathbf{W} is
 286 $[203]$ then *at least one* of the GND types involved *must* have Burgers vector with an $[001]$
 287 component, though not necessarily parallel to $[001]$. Similarly, *at least one* of the GND types
 288 involved *must* have Burgers vector with an $[100]$ component. \mathbf{W} could be decomposed as
 289 $2[100] + 3[001]$, or $2[101] + 1[001]$, or $3[101] - 1[001]$ or even simply $1[203]$ if $[203]$ is a
 290 known Burgers vector. [In a later section](#)

291 We next illustrate how to visualise and interpret the WBV, using models for a smoothly tilted
 292 lattice and a smoothly twisted lattice (for illustration, distortions are much larger than those
 293 found in real crystals). We then address a tilt subgrain wall, describing some issues that are
 294 specific to sharp changes in orientation. The models have no variation of orientation in the z
 295 direction and the Nye tensors can be calculated fully (Appendix 2).

296

Figure 3. Basic WBV concepts illustrated with model tilted and twisted crystals. a), b) 3D views of model tilted and twisted crystals, planes are colour coded in accord with IPF key (inset) for plane normal. Pale yellow of semi-transparent rectangles indicates the map plane though not the shape, [with x and y marked for subsequent maps](#). c), d) Misorientation relative to top-left corner for tilt and twist models. In c) misorientation is around the $[001]$ axis that points out of the page. In d) misorientation is around the $[010]$ axis, running left-right, with linearly increasing gradient of twist angle to right. e), f) WBV magnitude (in μm^{-1}) colour coded for each model. In e) actual vector directions shown as white arrows; in f) WBV directions point directly into page so are not shown. The boxes are example integration loops with the net WBV indicated as \mathbf{K} coefficients in $(\mu\text{m})^{-2}$. g), h) WBV direction colour coded for each model. i) 3D view of semi-transparent WBV magnitude map for tilt model (as in (e)), with edge dislocations lines shown schematically: parallel to $[010]$ and colour coded in accord with their $[100]$ Burgers vectors. j) 3D view of semi-transparent WBV direction map for twist model (as in (h)), with two sets of screw dislocations lines shown schematically: blue parallel to $[100]$, red parallel to $[001]$. For visual clarity the dislocations are shown as if in walls, but the distortion gradient is smooth. Note how the “weighting” towards dislocation lines perpendicular to the map causes variation in WBV direction (as in f) although the relative density of the two types of dislocation is uniform in 3D.

297

298 2.2.2. Smoothly tilted crystal

299 This model is similar to Fig 2, with a 3D view shown in Fig. 3a). The lattice is misoriented
 300 relative to the y -axis by an angle θ (zero along the y -axis and < 0 to the right), Fig. 3c). The
 301 misorientation axis is $[001]$ that points out of the page. The centre of curvature is beyond the
 302 bottom left of the map (Fig. 3c)). If r is the distance to this centre, it is the radius of curvature
 303 of the lattice and in sample coordinates

$$304 \mathbf{W} = \frac{1}{r} (\cos \theta, \sin \theta, 0)$$

305 and in crystal coordinates,

$$306 \quad \mathbf{W} = \frac{1}{r}(1, 0, 0) \quad (6)$$

307 The magnitude of \mathbf{W} is shown in Fig. 3e), increasing towards the centre of curvature in
 308 accord with eqn. (6). The WBV is a vector that can be represented in sample or crystal space:
 309 these require different methods for visualising direction. In sample space WBVs can be
 310 displayed as arrows on a map as in Fig. 3e). The direction in crystal coordinates is colour
 311 coded (as in any other sort of IPF map) in Fig. 3g), with the IPF colour scheme inset. Since
 312 \mathbf{W} is everywhere parallel to [100] we see a single colour. The rectangle is an integral loop
 313 labelled with its net Burgers vector content in units of $(\mu\text{m})^{-2}$; note only the first [100]
 314 component is non-zero.

315 Multiple decompositions of \mathbf{W} are possible, but the simplest is a single population of edge
 316 dislocations with lines parallel to [001], Burgers vectors parallel to [100] and density

$$317 \quad \frac{1}{ar}$$

318 where a is the length of [100]. Fig. 3i) shows a 3D view of that model. If this were not a
 319 model, all the map and WBV data could be in accord with other interpretations, for example
 320 dislocation lines not parallel to z . However, *any* interpretation must involve dislocations with
 321 Burgers vectors with a [100] component: the WBV calculation cannot generate “phantom”
 322 components (see above).

323 2.2.3. Smoothly twisted crystal

324 This model illustrates the importance of understanding the “weighting” or stereological bias
 325 in the WBV calculation. In Fig. 3b) the twist is defined by misorientation by angle θ around
 326 the [010] axis, with $\frac{d\theta}{dx}$ increasing to the right. Fig. 3d) shows the misorientation, defined as
 327 the *minimum* angle (with no absolute sign) required to rotate a lattice back to a reference
 328 orientation, relative to the top-left corner. Because this is olivine, symmetry dictates that the
 329 misorientation reaches a maximum at 90 degrees then decreases rightwards even though the
 330 lattice is more twisted to the right and the angle θ used for calculations increases
 331 monotonically. In sample coordinates
 332 (appendix 2.2) we have

$$334 \quad \mathbf{W} = \frac{d\theta}{dx}(0, 0, -1)$$

335 In crystal coordinates

$$336 \quad \mathbf{W} = \frac{d\theta}{dx}(\sin \theta, 0, -\cos \theta) . \quad (7)$$

337 The magnitude of \mathbf{W} is simply $\frac{d\theta}{dx}$ and increases linearly to the right because θ is quadratic in
 338 x (Fig. 3f)). WBV arrows in sample coordinates are not shown for the twist example because
 339 they all point vertically out of the map. Despite the fact that individual dislocation lines and
 340 Burgers vectors are clearly not vertical, the WBV components parallel to the map cancel out
 341 because we are adding weighted contributions. In crystal coordinates the direction of \mathbf{W}
 342 varies sinusoidally with θ (Fig. 3h)). The rectangle is an integral loop labelled with its net
 343 Burgers vector content in units of $(\mu\text{m})^{-2}$; note both [100] and [001] components are non-
 344 zero, in agreement with the presence of blues and purples within the loop. The variation in

345 WBV direction across the map could be interpreted to mean that different types of dislocation
 346 predominate in different parts of the model. This is not the case: it is a stereological effect
 347 and needs careful explanation now because such effects must be borne in mind in any study.

348 Multiple decompositions of \mathbf{W} are possible, but the simplest is as a sum of contributions from
 349 screw dislocations parallel to [100] with a density of

$$350 \frac{1}{a} \frac{d\theta}{dx}$$

351 and screw dislocations parallel to [001] with a density of

$$352 \frac{1}{c} \frac{d\theta}{dx}$$

353 This decomposition is show in Fig. 3j). The screw dislocation lines are coloured using the
 354 IPF colour scheme for screw dislocation *line direction* (as in Fig. 3g)) but since these are
 355 screw dislocations the colours also indicate Burgers vector directions. Consider the model
 356 near the left hand end where θ is small. Blue dislocations, with [100] line vectors, are almost
 357 parallel to the map. This means the WBV calculation does not “sample” them and the IPF
 358 colour (Fig. 3h)) is dominated by red [001]. As the lattice is more twisted passing to the right,
 359 [100] lines are at higher and higher angles to the map. Hence the WBV IPF map is more
 360 dominated by blue. At a position near the right-hand side of the map, [001] lines are parallel
 361 to the maps so are not sampled at all; the IPF map is blue. As θ increases beyond 90 degrees
 362 we see an influence of [001] reappear. This is an example of the “weighting” towards
 363 dislocation lines at a high angle to the map.

364 The twist structure illuminates some fundamental aspects of WBV. The displays are entirely
 365 in accord with eqn. (7) and the WBV provides a weighted “subset” of the full dislocation
 366 population. If we were to examine another map at right angles to the one considered (but still
 367 containing the twist rotation axis) this second map would show a preponderance of [100]
 368 vectors at the left end, with more [001] passing to the right – it would look quite different.

369 2.2.4. Model of subgrain tilt wall

370 Many microstructures contain subgrain walls that, although populated by GNDs, have in
 371 essence zero width and hence zero volume. This means that dislocation density, defined as
 372 line length per unit volume, is infinite. Similarly, a sharp change in orientation means the
 373 lattice curvature is infinite. So, although eqn. (4) still applies, it is not particularly helpful. In
 374 contrast the integral method is helpful because it still yields finite values when the loop
 375 crosses a subgrain wall. ~~For any particular subgrain wall the Now, though, the quantities~~
 376 ~~obtained are highly dependent on the size of the loop chosen for integration: the area does not~~
 377 ~~affect the~~ net Burgers vector content \mathbf{B} ; ~~depends~~ only the length of subgrain wall intersected
 378 by the loop, ~~and not on the loop area.~~ In this paper we use a vector \mathbf{B}/A with units of
 379 $(\text{length})^{-1}$ to characterise the GND content of any loop. ~~For a subgrain wall, then, the~~
 380 ~~magnitude of \mathbf{B}/A is strongly influenced by loop area.~~ Fig. 4 shows three loops, each
 381 intersecting the same length of subgrain wall and having the same value of \mathbf{B} . ~~However, the~~
 382 ~~areas differ and so the values magnitudes of \mathbf{B}/A differ differ; however, the direction of \mathbf{B}/A~~
 383 ~~is not influenced by A and carries useful GND information.~~ The advantage of the integral
 384 ~~method for analysing subgrain walls persists when we consider spaced measurement points~~
 385 ~~(section 2.3.2).~~

Fig. 4. Numerical aspects in of subgrain wall analysis - a sharp boundary indicated by green line, misorientation 5.6° around [001], crystal directions shown on either side with exaggerated misorientation for clarity. The 3 white boxes are used as loops to indicate the average dislocation density using the integral method (inset numbers for each box): they have relative lengths 1, 2 and 3.

386

387 So far we have assumed that all the analysed distortions are due to GNDs, but for sufficiently
388 high angle boundaries this will not be the case. We discuss this in detail next.

389 2.2.5 “High angle” boundaries and boundary dislocation content

390

391 When can boundaries be regarded as made of GNDs? Questions emerge for high angle grain
392 boundaries (HAGBs) where basic geometry proves that dislocations with specific Burgers
393 vectors must be close together and may not be recognisable as discrete entities. White (1976)
394 states “The limit is reached when dislocations are so closely spaced that they lose their
395 individual identity and when this happens the boundary is no longer a low angle sub-grain
396 boundary but a high angle, mobile, grain boundary. If a spacing of 2.5 nm (five lattice
397 spacings) is taken as the minimum distance before core interference ... then a low angle
398 boundary becomes a grain boundary when the misorientation is about 10° ”. Trimby et al.
399 (1998) state “Without detailed TEM [Transmission Electron Microscopy] studies the nature
400 of a boundary can only be constrained from the nature of the misorientation across it”: here
401 “constrained” does not mean “fully described”. They continue “In many studies an arbitrary
402 misorientation value is assigned, above which boundaries are assumed to be grain boundaries
403 and below which they are assumed to be subgrain walls although, in some cases (e.g. quartz),
404 this value corresponds to the necessary misorientation for the overlap of dislocation cores.
405 Typical values are 10° for quartz (White 1976), 15° or more for halite (Guillopé & Poirier
406 1979) and 15° for olivine (Poirier & Nicolas 1975)”. Two decades later there is still a lack of
407 clarity regarding such angles, but we discuss some relevant work next.

408

409 Shigematsu et al. (2006) coupled TEM to EBSD and showed that in quartz boundaries
410 dislocation substructures were lost somewhere between 9° and 17° , with one 13.5° boundary
411 still having dislocations (beyond the angular limit of 10° mentioned above). Mamtani et al.
412 (2020) image dislocations near HAGBs in magnetite using TEM as do Zhang et al. (2020) in
413 a Pd-10%Au alloy. So, HAGBs are not always disorganised. Kuhr and Farkas (2019) used
414 molecular dynamics models of an FCC polycrystal and found dislocations present in some
415 HAGBs. Twin boundaries may have dislocations e.g. p 79 of (Sutton & Balluffi 1995) but if
416 the twin plane is perfectly oriented there are none. An attempt to apply the WBV calculation
417 would yield an enormous and illusory dislocation density. Some HAGBs have lattices in
418 direct contact (Marquardt & Faul 2018), others may have amorphous films nm thick (Wirth
419 1996). In summary, HAGBs have diverse characteristics. We cannot address that diversity
420 here; nor can other methods of using EBSD data to deduce dislocation information. We
421 simply assert that our calculation is interpreted assuming that the lattice curvature is due to
422 the presence of GNDs. There is no single “cut-off” HAGB angle beyond which the GND
423 assumption is invalid. For this reason, in the algorithms we have created the user chooses the
424 HAGB angle above which calculations are excluded. The WBV method may in future
425 provide useful information about HAGB structure, but further research is required.

426

427 Our models up to this point are based on algebraic descriptions of distorted lattices (see
428 Appendix 2). We next address the finite number of measurement points that comprise an

429 actual EBSD map, and their consequences for gradient and WBV calculations (section 2.3).
 430 We then explore the errors in orientation and their consequences for those calculations
 431 (section 2.4).

432 2.3. Numerical aspects of analysing spaced EBSD measurement points

433 Orientation data to be analysed are not mathematical functions of position but discrete
 434 measurements at scattered measurement points (hereafter, simply “points” for brevity). The
 435 calculation methods therefore involve numerical approximations to the gradients and
 436 integrals of the underlying theory, and the differential and integral methods have different
 437 advantages in practice. The points in the studies we describe are on square grids, but there is
 438 no reason why the method should not be extended to hexagonal or other grids.

439 2.3.1. Differential method

440 The differential method uses gradients in orientation in the x and y map directions to
 441 calculate the WBV. A numerical estimation of gradients uses 2 or more orientation
 442 measurements and the distances between the points. We call the cluster of points used a
 443 “stencil” (Fig. 5a)). Here each measurement point is represented by a square with a side equal
 444 to the step size, so a stencil is illustrated as a cluster of squares. For flexibility our software
 445 allows for different stencil sizes; the differential method calculates a “best fit” lattice
 446 curvature using the orientations at each point in the stencil. Using larger stencils reduces
 447 errors in calculation (discussed later), but at the same time “smears out” microstructural
 448 details on the scale of the stencil. In published works the $P = 9$ stencil has usually been used;
 449 we discuss the effects of stencil size in the section on accuracy below.

Figure 5. Stencils, orientation gradients and errors relevant for WBV. a) “Stencils” are arrangements of nearby measurement points (shown here as squares) used for numerical calculation of orientation gradients at the central point (coloured). Shown are example stencils of area 3, 5, 9 and 21. b) Illustration of effects of orientation errors. Blue graph shows a low but uniform orientation gradient (in 1D) with errors imposed. Red lines show the large effects of errors on estimating gradients over a short segment (analogous to using a small stencil). Note the estimate may even have the wrong sign. Orange line shows the improved precision using a longer segment (analogous to using a larger stencil as in a)). Inset illustrates consequent angular error in WBV direction (in 2D). The actual WBV is shown as middle arrow but with error ε (related to the gradient error) so WBV values might fall in the circle. Outer arrows illustrate the range of directions and hence the angular error δ that would arise due to these errors. c) as in b), with the same errors imposed, but for a larger orientation gradient. The errors in slope are the same as in b) but are *proportionately* less. The error ε in WBV is the same as in b) and the size of the error circle is the same for both. However, the angular error δ is smaller in c) because the WBV is longer.

450

451 In a ~~previous~~ section 2.2.4 we pointed out that if a subgrain wall is considered as having zero
 452 width, it will have infinite dislocation density. Because of this numerical differentiation
 453 creates numerical artefacts as it uses spaced measurement points. The algorithm cannot
 454 distinguish a sharp orientation change between two points from a smooth orientation gradient
 455 between those points. A consequence is that if a subgrain wall is present, the apparent WBV
 456 magnitude will be finite and depend on step size, so should be interpreted with care. In

457 practice we find that narrow “swathes” of high W are common on calculated W maps and are
 458 likely to be subgrain walls. In this case the magnitude W must be interpreted with care but the
 459 WBV direction still contains information on the Burgers vectors of the GNDs in the subgrain
 460 wall. The 3 boxes in Fig. 6 indicate the calculated W values for a sharp orientation boundary,
 461 using the differential method using stencils with areas 9, 13 and 21. Note how the dislocation
 462 density is smeared out more for larger stencils, and has apparently lower values.

Fig. 6. Numerical aspects in of subgrain wall analysis - a sharp orientation boundary indicated by green line – using the differential method. The 3 black boxes show regions in which W has been calculated using stencils of size 9 (top), 13 and 21. Compare Fig. 4 which uses the integral method on the same boundary.

463

464 2.3.2. Integral method

465 The integral method involves integrating the orientation tensor around a closed loop in the
 466 map plane, directly giving the net Burgers vector sum for all the dislocation lines threading
 467 through that loop. The details of numerical integration are given in Supplementary
 468 Information 1.2. Publications to date have restricted loop shapes to rectangles, though there is
 469 no fundamental difficulty in implementing other shapes and this has been done in a
 470 commercial version of the algorithm in the Oxford Instruments Aztec system. The result of
 471 integration is a vector \mathbf{B} with dimensions of length. We divide this by the loop area A to get a
 472 vector in $(\text{length})^{-1}$ which is more easily compared to results of the differential method.
 473 Algebraically, the vector \mathbf{B}/A must equal the average \mathbf{W} value in the loop (eqn. (6)).
 474 Numerically, the “best fit” algorithm used in the differential method means the methods may
 475 give slightly different results: for subgrain walls the integral method remains advantageous
 476 (c.f. section 2.2.4).

477 In Wheeler et al. (2009) the integral method was presented as an exploratory tool in which
 478 the user drew rectangular loops and the WBV was reported as a lattice vector (e.g. Fig 3e,
 479 f)). More recently a method of systematically “tiling” the map with square loops, and
 480 applying the integral method to each loop was used in Fig. 8c of Timms et al. (2019). The
 481 tiles can be displayed colour coded by standard IPF colour schemes using a W threshold, in
 482 the same way as for calculations made with stencils (examples are given later). The tiles can
 483 be thought of as large pixels, though not all properties are precisely analogous to those of
 484 individual measurement points. In all circumstances, if the loop crosses a high angle
 485 boundary, then a WBV can in principle be calculated but as discussed above, has no meaning
 486 - so instead the algorithms we use do not return a result and the tile is left uncoloured.

487 2.4. Numerical aspects of dealing with orientation measurement errors

488 Orientation measurements used may be in error as a result of errors in the Hough transform,
 489 up to a degree at most (Prior et al. 2009); for one study on an Si single crystal, was 0.2° (Ram
 490 et al. 2015). Improved “real time” approaches to indexing Kikuchi patterns reduce the
 491 angular error in orientations to $<0.05^\circ$ (Nicolay et al. 2019). For higher angular resolution
 492 methods, e.g. correlating Kikuchi patterns, errors may be as low as ~ 0.0003 radians (Wallis et
 493 al. 2019a). The differential method uses gradients in crystal orientation to calculate WBV. On
 494 the grid of measurement points, a gradient is calculated from the misorientations between
 495 adjacent measurements. The misorientation angles are likely to be small and so the errors in
 496 misorientation axes will be large (Prior 1999) and these errors will propagate into the WBV

497 calculation. An algebraic analysis would involve error propagation through operations on
 498 various orientation tensors and is beyond the scope of this contribution; instead, we use
 499 simple arguments followed by some numerical experiments.

500 2.4.1. General nature of error effects

501 We argue in this section that angular errors in WBV are smaller for long WBVs. Longer
 502 WBVs are linked to higher lattice curvatures. Higher lattice curvatures mean the
 503 misorientation angles between adjacent pixels are larger, and the misorientation axes will
 504 have smaller errors, and the WBV direction will have smaller errors. We illustrate this
 505 assuming a typical orientation error of 0.01 radians.

506 Benchmark curvature (above which calculation will be less error prone) $\sim 0.01/(\text{step size})$
 507 and in terms of magnitude

508 $|\text{WBV}| \sim \text{curvature}$

509 which means we should consider a benchmark below which WBV is error-prone as

510 $|\text{WBV}| \sim 0.01/(\text{step size}) = W_t$

511 This approach is similar to the derivation of eqn. 13 of Wilkinson and Randman (2010) and
 512 eqn 2 of Jiang et al. (2013), where a lower limit on detectable dislocation density is given in
 513 terms of step size:

514 (Minimum detectable GND density) \sim

515 $(\text{Angular resolution}) / ((\text{step size}) * (\text{Burgers vector length}))$

516 For example $0.01 / ((1 \text{ micron}) * (5 \text{ angstrom})) = 2 \times 10^{13} \text{ m}^{-2}$

517 The approach described below is related because in order of magnitude, $W = \rho b$. Hence our
 518 W_t/b equates to the minimum detectable GND density discussed in other work. That work,
 519 and others (by the group) focusses on accuracy in determining dislocation *density*; here we
 520 also analyse WBV *direction* since it plays a key role in several studies (Table 1). In Wheeler
 521 et al. (2009) we argued that longer WBVs would be more accurate in terms of direction. For
 522 example, the map of Mg used in Fig. 2 and 3 of Wheeler et al. (2009), modified in Fig. 7, has
 523 a step size of $4 \mu\text{m}$ so $W_t = 0.0025 \mu\text{m}^{-1}$. Fig. 7 shows considerable scatter for $W > 0.002 \mu\text{m}^{-1}$
 524 and much less for $W > 0.004 \mu\text{m}^{-1}$, in accordance with the argument that W_t offers a guide
 525 to judging precision. Guided by this, our approach to displaying WBV data involves selecting
 526 data based on ranges of W . The minimum value W_{min} in the range will be associated with the
 527 maximum angular error. Setting it high will reduce error. The maximum value W_{max} is less
 528 important but is useful for dividing up datasets.

Figure 7. IPFs of Mg WBV displayed using three different thresholds: threshold lengths and numbers of points as indicated, modified from Fig. 3 of Wheeler et al. (2009).

529

530 Figure 5b) and c) are non-rigorous illustrations of error effects. The graphs illustrate that
 531 larger stencils will give better precision. Errors ϵ in gradients are independent of the gradients
 532 themselves but for larger orientation gradients (as in Fig. 5c)), longer WBVs) the errors are

533 *proportionately* less important. The insets in b) and c) illustrate the consequent effects on
 534 angular errors. The errors in WBV are now drawn as circles around the actual values since
 535 errors may be in any direction. The error circles are the same size in b) and c). The green
 536 arrows mark the vectors with maximum angular error δ , showing that longer WBVs in c) will
 537 have smaller angular errors. In the next section we analyse error effects using numerical
 538 models.

539 2.4.2. Specific analyses of error effects

540 It is useful to quantify error estimates for WBV, incorporating the effects of WBV length and
 541 other parameters. We define an angle α_{95} so that there is a 95% chance that the true WBV
 542 direction is that angle or less from the calculated direction, an approach used in analysing
 543 palaeomagnetic data for example Butler (1992). In essence α_{95} defines a cone of directions
 544 within which the true direction is likely to be. This is analogous to the ± 2 standard deviation
 545 range within which 95% of the data lie when dealing with a one-dimensional normal
 546 distribution. Our approach gives the angular error for the WBV in sample coordinates: it is in
 547 principle the same for crystal coordinates except crystal symmetry may modify the
 548 interpretation, as addressed in Appendix 3.1.

549 EBSD orientation errors will depend on mineralogy, acquisition conditions and indexing
 550 methods and will propagate in the WBV calculations. For illustration we create model
 551 orientation maps with angular errors in orientation up to 0.57° (0.01 rad) – so our angular
 552 error estimates for WBVs are likely to be pessimistic. We used theoretical models shown in
 553 Fig. 3 with added orientation noise, and calculated \mathbf{W} for the noisy datasets. Larger stencils
 554 and tiles take into account more orientation measurements and, in common with other
 555 averaging methods, we hypothesised in Wheeler et al. (2009) that this would give higher
 556 precision. We examine this idea in Appendix 3. First, we calculate the error on WBV, by
 557 comparing actual \mathbf{W} and theoretical \mathbf{W}_c values. We find that the error in WBV magnitudes \mathbf{E}
 558 $= \mathbf{W} - \mathbf{W}_c$ are not strongly dependent on length W , or on whether the model is tilt or twist,
 559 but they do depend on stencil size. To quantify the errors, we calculate a standard deviation σ
 560 for the vector \mathbf{E} as described in Appendix 3. Larger stencils and tiles give smaller errors (Fig.
 561 6). So, if one uses stencils (i.e the differential method), there is an approximate relationship
 562 between W precision and the area S of a stencil (number of points, hence dimensionless)

$$563 \sigma_S = 0.0247S^{-1}/u \quad (7)$$

564 where u is step size.

565 If one uses tiles (i.e. the integral method) and defines the dimensionless area T of a tile the
 566 standard deviation σ_T of vector \mathbf{E} is:

$$567 \sigma_T = 0.0081T^{-3/4}/u \quad (8)$$

Figure 8. a) Standard deviation σ of nondimensionalised WBV magnitude plotted against calculation region size for tilt and twist models, showing errors are independent of the detailed nature of distortion. The three left-hand points are for stencils, the others are for tiles. b) Same, plotted against areas of stencils and tiles for both tilt and twist models. c) Same as b) but plotted as log-log graphs to show linear relationships.

568

569 In Wheeler et al. (2009) we suggested that the integral method would have higher precision
 570 than the differential method because numerical integration is less sensitive to errors than
 571 numerical differentiation. Our assertion was correct because we were using small stencils (P
 572 = 9) and large integral loops. Fig. 8 b) and c) show that in fact the precision depends mainly
 573 on the area of the tile or stencil used. The integral method remains our favoured method for
 574 initial exploration since the calculation is much faster than for a stencil of comparable size.

575 The second stage of error analysis involves the angular errors. These *do* depend on the length
 576 W as described above and in Fig. 8. The inset in Fig 5c) suggests that $\delta \approx \varepsilon/W$ when errors
 577 are small. This is in accord with Fig. S1. One might then expect some proportionality
 578 between measures of vector error σ and angular error α_{95} in a more rigorous approach, and
 579 this is confirmed in Appendix 3. For small errors we have

$$580 \quad \alpha_{95} \cong 1.413 \frac{\sigma}{W}$$

581 For example, in Table 1, for the second Mg example we have a step size of 4 μm and
 582 calculated the WBV using a stencil area 9 so $\sigma_s = 0.000686 \mu\text{m}^{-1}$. For a WBV length 0.004
 583 μm^{-1} we have

$$584 \quad \alpha_{95} \cong 1.413 \frac{0.000686}{0.004} = 0.24 \text{ rad} = 13.8^\circ$$

585 (the table calculation is more precise). If we compare the calculated α_{95} with Fig. 7c), it is
 586 plausible that the dislocations are all basal and we see a scatter up to 14° away from the basal
 587 plane, broadly in accord with the calculation. The above assessment of precision should be
 588 used with caution, since it assumes a particular range of orientation errors in the measured
 589 data, and those errors are dependent on acquisition conditions and the mineral being
 590 measured. A larger stencil or tile will give a more precise measure of WBV magnitude and
 591 direction, but larger regions are also more likely to contain more than one type of dislocation.
 592 There is a trade-off between finding a relatively precise WBV direction in a large region that
 593 may contain more than one type of GND, versus finding a less precise direction in a smaller
 594 region which may relate to a single type of GND.

595 Our error analysis is numerical rather than algebraic but simple calculations give confidence
 596 that, if other parameters are maintained, the WBV angular error will scale linearly with
 597 orientation angular error. Thus, if angular errors are distributed uniformly between 0 and
 598 0.001 rad, we expect angular errors in WBV to be 10 times less than those we present here.
 599 Such low indexing errors are now routinely possible, albeit with a trade-off on indexing
 600 speed (Nicolay et al. 2019). Improved indexing would allow for use of a smaller stencil or tile
 601 ensure a particular level of WBV precision. We note that algorithms that assign interpolated
 602 orientations to misindexed or non-indexed pixels may have adverse effects on subsequent
 603 WBV calculations. For example, if the orientation value of an adjacent pixel is used, this
 604 guarantees that there is a zero orientation gradient between those two pixels, which may have
 605 a big (and spurious) influence on the WBV calculation. Ideally, analysis is done only on
 606 confidently indexed points. We also urge caution using dictionary indexed EBSD maps (De
 607 Graef 2020) for WBV calculations, because the orientations stored in the dictionary of
 608 Kikuchi patterns are discrete and orientation gradients therefore will be stepped. This may
 609 give a spurious influence on WBV calculations.

3. WBV applications in Earth Sciences: examples

610
611
612 The published works in Table 1 show a variety of approaches for interpreting WBV. The
613 basic algorithms we use do *not* decompose the WBV down into individual Burgers vectors
614 because to do this requires additional assumptions, dependent on the particular mineral and
615 its microstructural evolution. For example, a WBV parallel to [100] may result from a single
616 population of GNDs with Burgers vectors parallel to [100], or a mix of dislocations with
617 [110] and [1-10]. In some phases, prior knowledge of likely Burgers vectors will mean there
618 is only one choice for decomposition – e.g. if such a WBV is found in olivine. In the
619 following, we present first two new examples of WBV usage and then comment on published
620 examples.

Figure 9. Example of WBV applied to olivine. a) IPF map of Y direction of deformed single crystal of olivine. Scale bar is 1000 μm . b) IPF key. c) IPF coloured as in a), showing a few degrees of distortion within a single initially undeformed crystal. d) WBV magnitude map calculated on 10 x 10 tiles. e) IPF map of WBV direction (calculated as in (d)) superimposed on a band contrast greyscale map; minimum length 0.001 μm^{-1} . f) IPF of WBV as in (e). g) WBV magnitude map calculated on 3 x 3 stencils in part of overview map shown as white box in (d). Scale bar is 1000 μm . Inset shows orientation variation (degrees) from left hand end of transect marked by white line. h) IPF map of WBV direction (calculated as in (g)) superimposed on a band contrast greyscale map; minimum length 0.00005 μm^{-1} , showing subgrain walls with [100] Burgers vectors running NE and those with [001] running NW. White squares indicate results of the integral method, with numbers in μm^{-2} expressed as coefficients of crystal basis vectors (K values). i) IPF of WBV as in (h).

621
622 *3.1. Olivine: subgrain wall analysis free from trace, or tilt or twist assumptions*
623 Fig. 9 shows an experimentally deformed single crystal of olivine (PI-1766) as in Fig. 8 of
624 Tielke et al. (2017). The experiment was set up so that the Y (shortening) direction was
625 initially parallel to [101]_c, at 45° to [100] and [001], with an expectation that slip systems
626 with [100] and [001] Burgers vectors would be activated. The orientation map (a) shows the
627 crystal direction that is parallel to the Y sample direction, in accord with the IPF key (b). We
628 refer to such maps as “IPF Y maps” below. The colour variations reveal rather straight
629 subgrain walls running in two directions. Orientations vary over a few degrees (c). Fig 9(d)
630 shows 10 x 10 tiles colour coded by WBV magnitude and (e) by direction, superimposed on
631 the band contrast greyscale map. The size of the tiles reduces α_{95} but the threshold length for
632 display is set low, at 0.00005/ μm , so α_{95} is 26°. With this in mind, the IPF Fig 9f) is, within
633 error, in accord with a mix of dislocations with [100] and [001] Burgers vectors, and the
634 dominant blue colour on the map indicates mainly [100]. Figs (g) and (h) show a subarea
635 with WBV now calculated using a 3 x 3 stencil, giving less precision but more spatial
636 resolution and revealing individual subgrain walls. Blue subgrain walls running NE are
637 consistent with being [100] tilt boundaries and red subgrain walls running SE are consistent
638 with being [001] tilt boundaries. A higher threshold length for display (0.001/ μm) means α_{95}
639 is 14° and the IPF in Fig. (i) is in accord with that, insofar as most points are within 14° of the
640 plane containing [100] and [001]. There are still mixtures of [100] and [001]. Some will
641 result from where the stencil overlapped subgrain wall junctions, but as Fig. (h) shows, these

642 mixtures also appear along irregular segments of the NW-SE subgrain walls and are likely to
 643 represent two types of GND in an individual wall. The three square “loops” show results of
 644 the integral method and provide additional illustration of how the WBV is averaged over the
 645 sample area. Each triplet of numbers is a list of K values, i.e. the coefficients defining the
 646 WBV when it is expressed in crystal basis vectors (eqn (5)). The numbers have the
 647 dimensions of dislocation density but must be interpreted with care, as discussed above and
 648 shown in Fig. 4, since the dislocations are in discrete walls.

649 In this example the directional information is more useful than the density information:
 650 integral and differential methods both give information about where GNDs with [100] and
 651 [001] occur. Note that examining the subgrain wall traces together with misorientation axes
 652 deduced from the distortion (Fig. 9c) could yield similar results. However, that approach
 653 would involve manual and subjective selection of boundary segments and of subregions from
 654 which to use misorientation data; it would be based on assumptions about pure tilt or twist
 655 boundary character and errors would be difficult to assess. Use of WBV does not preclude
 656 further analysis (e.g. Wieser et al. (2020)) but provides a firm foundation.

657 3.2. Plagioclase: distributed deformation analysis free from slip system assumptions

658 Fig. 10 shows plagioclase from a deformed gabbro from close to the slow spreading mid
 659 ocean ridge in the SW Indian Ocean (sample ODP 176-735B-95R-2 from approx. 546 m
 660 below the ocean floor). The plagioclase is highly strained, with two prominent ribbons bent
 661 around an augite porphyroclast (grey scale on right). Trails of smaller grains are interpreted
 662 as new grains due to recrystallization. Hornblende marginal to pyroxene suggests
 663 deformation is amphibolite facies, as recorded deeper in the leg (Gardner et al. 2020), but it
 664 may have been higher temperature. Our aim here is to not to offer a full interpretation of how
 665 the microstructure evolved, but to show how the WBV tools assist in that task.

Figure 10. Example of WBV applied to plagioclase. Figure layout is similar to Fig. 9 but contouring is used to reveal dominant directions. a) IPF map of plagioclase Y direction of a deformed gabbro. Inset shows orientation variation (degrees) from top end of transect marked by white line. The right-hand porphyroclast is augite rimmed by hornblende. b) Key for IPF map colour scheme. c) IPF map of plagioclase as in a), contoured with intervals at 0.1 x uniform. d) Magnitude of WBV calculated on 20 x 20 tiles in area a) superimposed on a band contrast greyscale map. e) IPF map of WBV calculated as in d) colour coded by WBV direction using b), minimum length 0.0005 μm^{-1} . f) IPF of WBV as in d) and e), contoured in multiples of uniform. g) Magnitude of WBV calculated on 3 x 3 stencils in white box subarea of map d) superimposed on a band contrast greyscale map. h) IPF map of WBV calculated as in g) colour coded by WBV direction as in b), minimum length 0.01 μm^{-1} . i) IPF of WBV as in g) and h).

666

667 The IPF Y map (Fig. 10a), colour coded as in 10b) indicates rather smooth variations in
 668 orientation for the large grain, in contrast to the olivine example Fig. 9a). Large tiles used in
 669 Fig 10d) confirm this, showing a rather uniform level of distortion on the scale of the tiles
 670 through the two ribbons. The WBV IPF map (Fig. 10e)) shows <100> dominates at the top of
 671 the left hand ribbon, whilst <001> dominates at the bottom, and the IPF (Fig. 10f)) combines
 672 these. In and around new grains no data is displayed (Fig. 10d and e) because the 20 x 20
 673 pixel tiles are large enough to cover several small grains and include high (> 5°) angle

674 boundaries. Thus, in these areas WBV analysis is not appropriate. It is worth considering
 675 whether the apparent variation in WBV direction is a stereological effect, like that shown in
 676 Fig. 3h), j). Could the ribbon have a relatively uniform population of GNDs, but with a
 677 stereological bias governed by varying orientation? The misorientation from bottom to top of
 678 (for example) the left-hand ribbon is about 35° in contrast to Fig. 3h), j) which involved 90°
 679 of twist. We conclude it is likely that there are real variations in the GND population in this
 680 grain, which is not surprising given the stretch and non-uniform bending it has enjoyed. Fig
 681 10g)-i) shows WBV calculated using the differential method on a subarea marked with a
 682 white box in Figs. 10d) and e). In Fig 10g), boundaries above 5° are shown in black and the
 683 highest distortions i.e. WBV magnitude are shown not in the large ribbons but in small grains
 684 interpreted as products of dynamic recrystallization. Fig. 10h) and i) show WBV direction,
 685 with a pronounced maximum close to $\langle 001 \rangle$ as illustrated by the preponderance of red
 686 colours in new grains in (h) and a contoured maximum near $\langle 001 \rangle$ in (i). The relict ribbon in
 687 centre right of Fig. 10h) shows two left-right tapered zones coloured green, indicating WBV
 688 rather close to $\langle -100 \rangle$ and in accord with the tiling in Fig. 10e).

689 In summary this example shows how the integral (here, tiling) and differential methods may
 690 be used to interrogate different parts of the microstructure. The interiors of the plagioclase
 691 ribbons have relatively low dislocation densities, with GNDs with Burgers vectors combining
 692 $\langle 100 \rangle$ and $\langle 001 \rangle$, likely in different proportions in different parts. Here, the integral method
 693 is a very effective tool. For the small grains, interpreted as recrystallized, the differential
 694 method is helpful; they have higher dislocation densities and various Burgers vectors but with
 695 an emphasis on $\langle 001 \rangle$. In tectonites small grains are often interpreted as new, forming by
 696 static or dynamic recrystallisation from strongly plastically deformed large old grains, and are
 697 relatively strain free. Intriguingly, here the small grains are more distorted than the old
 698 ribbons though normally one would expect them to be relatively strain free. Further WBV
 699 investigation will assist in understanding the evolution of that microstructure. Methods
 700 including the traces of subgrain walls could not be used here, since distortion is distributed;
 701 methods assuming slip systems and dislocation line energies could be applied but the
 702 required inputs may be difficult to constrain in a mineral like plagioclase. As in the olivine
 703 example, we suggest the WBV approach provides a firm foundation on which other analyses
 704 can be built if required.

705 3.3. Ice: investigation of non-basal slip

Figure 11. Example of WBV applied to a subgrain in ice, modified from Fig. 2 of Chauve et al. (2017). WBV is colour coded not by the full IPF but just by the sin of the angle of the WBV from the basal plane, i.e. (component of W parallel to c)/W. This runs between 0 and 1 as shown by the colour scale. Red arrows show the WBV projected onto the map plane, using its actual length not just its direction. Black line is a subgrain wall of 5° or more misorientation.

706

707 There is ongoing research into the role of non-basal slip in ice, since if that is active it will
 708 alter the rheology of ice sheets (Chauve et al. 2017, Piazzolo et al. 2015, Weikusat et al. 2011).
 709 Chauve et al. (2017) undertook deformation experiments on ice and Fig. 11a), modified from
 710 Fig. 2 of that paper, shows a subgrain from an experiment run at -7°C and 0.5 MPa stress.
 711 The WBV is colour coded not by the full IPF but just by the sin of the angle of the WBV

712 from the basal plane, i.e. (component of W parallel to c)/ W . For this dataset we estimate α_{95}
 713 as 32° (Table 1). The yellow vertical subgrain wall indicates angles near 90° from the basal
 714 plane so, even though the errors are large, there is negligible probability that these WBVs lie
 715 in the basal plane. Moreover, the colours along this wall are quite consistent, adding credence
 716 to the diagnosis that the WBV is subparallel to c . It does not immediately imply that
 717 individual Burgers vectors are parallel to c : for example, there could be a mixed population of
 718 $c + a$ and $c - a$, bearing in mind the WBV is a vector average. Further data and/or assumptions
 719 are required to determine this. However, as noted above the WBV cannot contain “phantom”
 720 directions: it must be the weighted average of Burgers vectors that are actually present in the
 721 microstructure, and here must include non-basal vectors of some sort. The Figure also
 722 provides an example of WBVs drawn in red as vectors in sample coordinates. As discussed
 723 above and derived in Appendix 1, there is only one such choice at each point, regardless of
 724 crystal symmetry. Despite α_{95} being predicted as 32° , the WBV directions along each wall
 725 segment are quite consistent, suggesting the angular errors are in fact lower, though further
 726 work is required to confirm this.

727 3.4. Titanite: discovery of new slip system

728 Fig. 12 shows the use of tiling in a study of deformed titanite, modified from Timms et al.
 729 (2019). The titanite grain is from a shocked granitoid from the Chicxulub impact structure,
 730 Mexico, and the study searched for slip systems activated under extreme stresses, which
 731 would not necessarily correspond to slip systems documented from other settings. The study
 732 included a boundary trace/misorientation approach, but that assumed pure tilt boundaries, so
 733 the WBV method was used for independent verification. The differential method gave a wide
 734 scatter of WBV directions so to reduce errors 20×20 pixel tiles were used. The tiles are
 735 colour coded in terms of IPF direction; missing colours indicate either that the tile includes a
 736 high angle boundary, or the WBV magnitude is below the threshold for display (Table 1).
 737 There are many shock-induced twins, and the abundance of those high angle boundaries
 738 mean that tile coverage is sparse. However, the WBV directions show a strong maximum
 739 near $\langle 341 \rangle$. This is a Burgers vector not previously described in titanite but likely indicating
 740 a dislocation slip system operating concurrently with twinning under shock.

Figure 10. Example of WBV applied to titanite. The greyscale map is of band contrast in a shocked titanite grain and its surroundings, redrawn from Fig. 8 of Timms et al. (2019). Inset shows orientation variation (degrees) from lower left end of transect marked by thick black line. Tiling was used to analyse the microstructure – tiles are coloured for WBV direction in accordance with the IPF key on bottom left. The WBV IPF (top right) shows distinct preferred directions. Calculation and display parameters are given in Table 1.

741

742 3.5. WBV precision in specific studies

743 In Table 1 we compile the parameters required for estimating α_{95} from previous studies
 744 making a big assumption, that the orientation measurement errors in those studies are all
 745 distributed uniformly between 0 and 0.01 radians. Despite this, the error estimates are in
 746 general agreement with the appearance of the relevant IPFs. For example, for Mg metal Fig. 7
 747 shows IPFs with α_{95} of 28° and 14° , and those angles are in accord with the scatters of points
 748 if all WBVs are in fact in the basal plane. One large $\alpha_{95} = 110^\circ$ is for quartz and relates to
 749 Fig. 15 of Wheeler et al. (2009), but the left hand IPF there was drawn to specifically

750 illustrate the effect of choosing a threshold W that is too low. The cone of error would cover
751 the entire IPF and that is in accord with the random scatter of points seen. In contrast, another
752 study is predicted to have a large α_{95} of 110° yet the IPFs show strong maxima. Fig. 4 of
753 Kendrick et al. (2017) shows IPFs of WBV for deformed plagioclase microlites in an andesite
754 with strong maxima around [001], particularly in the experimentally deformed sample. We
755 suggest this is because there is a single family of GNDs with a single [001] Burgers vector.
756 Then, even though individual WBVs have large errors, the maximum is strong because the
757 errors cancel out to some extent. This is analogous to a standard result in statistics of a single
758 variable: the standard variation of the mean is equal to the standard deviation of an individual
759 measurement divided by the square root of the sample size. A similar idea might be
760 developed for directional statistics in future work.

761 **4. Comparison of WBV with other methods used for analysing GND directional data**

762 All 6 orientation gradients (3 in x and 3 in y) can be calculated from EBSD maps and provide
763 6 constraints on the Nye curvature tensor as in (Pantleon 2008), Wilkinson and Randman
764 (2010), Wallis et al. (2016). If there are 6 types of dislocation, then eqn (3) has a unique
765 solution for 6 GND densities, given the 6 constraints on the Nye tensor. In many materials,
766 particularly cubic phases, symmetry indicates there are more than 6 types of slip system and
767 there is no unique solution for eqn (3). So, an additional assumption is made, that the total
768 line energy of all the dislocations involved is the minimum out of all the possible solutions.

769 This approach uses more information than the WBV method (6 components of the Nye tensor
770 versus 3) but is based on assumptions that we recommend deserve appraisal on a mineral-by-
771 mineral basis.

- 772 i) Assumptions about allowable slip systems might be misleading as we do not have a
773 complete knowledge of all in all minerals.
- 774 ii) Assumptions about the line energies of each type of dislocation, to enable overall
775 energy minimisation if there are more than 6 slip systems, will be based on limited
776 information for minerals.
- 777 iii) Assuming that the types of dislocation related to slip also characterise growth defects
778 deserves scrutiny. For growth the concept of slip systems is not relevant: there might be
779 alternative lists of allowable GND types, but again in minerals such information is scanty.
- 780 iv) Assuming that dislocations have locally reorganised to minimise their net energy may
781 not be true (e.g. in cold working, or when defects are due to growth).

782

783
784 In contrast WBV calculation makes no assumptions about GND types at any stage of the
785 calculations. Instead, individual studies tailor the interpretation, possibly involving further
786 calculation, based on the problems being addressed. This is well illustrated in the published
787 ice non-basal slip example outlined above. Here, the hypothesis to be tested was to identify if
788 non-basal dislocations are present in ice, tested by calculating and displaying the angle of the
789 WBV to the basal plane (Chauve et al. 2017). The calculation is free from detailed
790 assumptions about dislocation types and energies, which are not well known. A further
791 example is provided in Wieser et al. (2020) who used the trace of subgrain walls together with
792 WBV analysis to provide additional constraints on potential activated slip systems. In this
793 case, additional assumptions were introduced, e.g. that all subgrain walls were either pure tilt
794 or pure twist. Those assumptions are not intrinsic to the WBV calculation. In essence the

795 WBV may provide sufficient information on its own and provides a platform for further in-
796 depth analysis which may use additional assumptions.

797 In a number of works using the “energy minimisation” method, the EBSD data are high
798 resolution electron backscatter diffraction (HREBSD) which gives higher angular accuracy to
799 orientation measurements: for details see Wilkinson and Randman (2010), Wallis et al.
800 (2016) and Wallis et al. (2019a). This means that errors in misorientation gradients and hence
801 WBV or other calculations will be lower than using conventional data (Gardner et al. 2024).
802 However, there is no intrinsic difference in applying WBV or energy minimisation
803 calculations to HREBSD versus conventional data or to data obtained with new techniques
804 e.g. (Winkelmann et al. 2020). WBV ~~could~~ can be calculated from HREBSD data, as in
805 Wallis et al. (2016) and Gardner et al. (2024). Equally, best fit/energy minimisation can be
806 used on Hough based orientation data as in Pantleon (2008).

807 5. Summary and discussion

808 We have described the theoretical basis for the WBV method and shown examples where it
809 has assisted in deducing Burgers vectors for slip systems in various minerals. Since the
810 method is purely geometric it can also be used to analyse distortions due to growth as in
811 Gardner et al. (2021). Key aspects of the WBV method are as follows.

- 812 • It makes no assumptions about the dislocation populations being investigated.
- 813 • It uses just the three numbers defining orientation at each measurement point, so is fast.
- 814 • It assumes there are no significant grain scale elastic strains.

815 The software we use in this contribution (“Crystalscape”) involves user-defined parameters
816 for calculation as follows; these need to be recorded to allow calculations to be reproduced.

- 817 • The cutoff angle above which boundaries are assumed to no longer have dislocation
818 substructure.
- 819 • The size of the stencil or tile used for systematic calculations.

820 WBV results can be displayed in several ways and the key user-defined parameters for
821 display are the minimum and maximum WBV lengths. The minimum length can then,
822 together with the other parameters, be used to estimate the angular accuracy α_{95} (the shortest
823 vectors being the least accurate in terms of direction). That estimation contains several
824 simplifications and, in any case, depends on an assumed angular error in the EBSD data; but
825 it serves as an indication of accuracy which proves useful.

826 For interpretation, the following properties must be borne in mind.

- 827 • The WBV does *not* measure the complete GND population or density. It is a sample of
828 that population, weighted towards dislocation lines that intersect the EBSD map at high
829 angles. Maps cut in different planes will show different but related WBV information.
- 830 • The WBV is a weighted sum of Burgers vectors of GNDs. In general, there are multiple
831 ways of decomposing the WBV, but it still provides a platform for testing hypotheses. It
832 will never generate “phantom” components. For example, if a trigonal or hexagonal
833 mineral shows WBVs with significant c axis components, there must be GNDs with
834 Burgers vectors involving c (though not necessarily parallel to c).

- 835 • Errors in WBV are smaller when larger stencils or tiles are used. Angular errors are
836 smaller for longer WBVs.
- 837 • Larger stencils or tiles tend to “smear out” the WBV pattern. Increased angular precision
838 is thus linked to reduced spatial resolution.

839 Future directions using this method could include further development of ways to
840 characterise non-basal slip in hexagonal and trigonal materials e.g. Chauve et al. (2017). The
841 combination of WBV analysis with subgrain boundary trace analysis (Wieser et al. 2020) has
842 potential to be developed for olivine and other minerals. More advanced statistical tests
843 related to directional data could be developed. We have not discussed 3D orientation data
844 here but in principle this allows calculation of orientation gradients in all three dimensions
845 and hence the complete Nye tensor which would be valuable for constraining GNDs.
846 However, even the 9 components of the Nye tensor are not sufficient to constrain all GND
847 types in very symmetric minerals. Statistical tests could be developed for 3D analysis as we
848 have done in 2D. Hybrid approaches using two or more maps at right angles also deserve
849 investigation.

850 We note that the methods discussed here are applicable to any crystalline material including
851 metals, ceramics and ice.

852 The Matlab software used for analysis here (“Crystalscape”) is available from the lead author
853 [for academic use only](#). In 2021 Oxford Instruments Nanoanalysis adapted a version of the
854 WBV method for use in Aztec Crystal, their EBSD analysis suite. This is described here:
855 <https://www.ebsd.com/ois-ebsd-system/dislocation-density-analysis> and in a webinar here
856 <https://register.gotowebinar.com/register/5472775566652982031>. ~~To safeguard the~~
857 ~~commercial development, Crystalscape for academic use only.~~

858

859 **Credit author statement**

860 **John Wheeler:** Conceptualization, Software, Writing - Original Draft, Visualization; **Sandra**
861 **Piazolo:** Conceptualization, Writing – Review and Editing; **David Prior:** Conceptualization,
862 Writing – Review and Editing; **Patrick Trimby:** Conceptualization, Resources, Writing –
863 Review and Editing; **Jake Tielke:** Resources, Writing – Review and Editing.

864 **Acknowledgements**

865 We thank all the user of the WBV method who have contributed through discussion to
866 developing the method. We thank Elena Miranda and David Wallis for constructive reviews
867 [and Virginia Toy for substantial editorial work](#).

868

869 **Table 1. Details of published WBV studies, and the new studies here**

870 Table 1. Published papers using WBV on minerals, with precision estimates added in this
871 contribution. We include one example of use on Mg metal as it helps illustrate the basic
872 ideas. In the right hand columns we have compiled information from the published works ~~so~~
873 ~~as~~ to estimate α_{95} based on the assumption that orientation measurement errors are distributed
874 uniformly between 0 and 0.01 radians, a realistic if somewhat pessimistic range for data
875 obtained by Hough transform.-

876

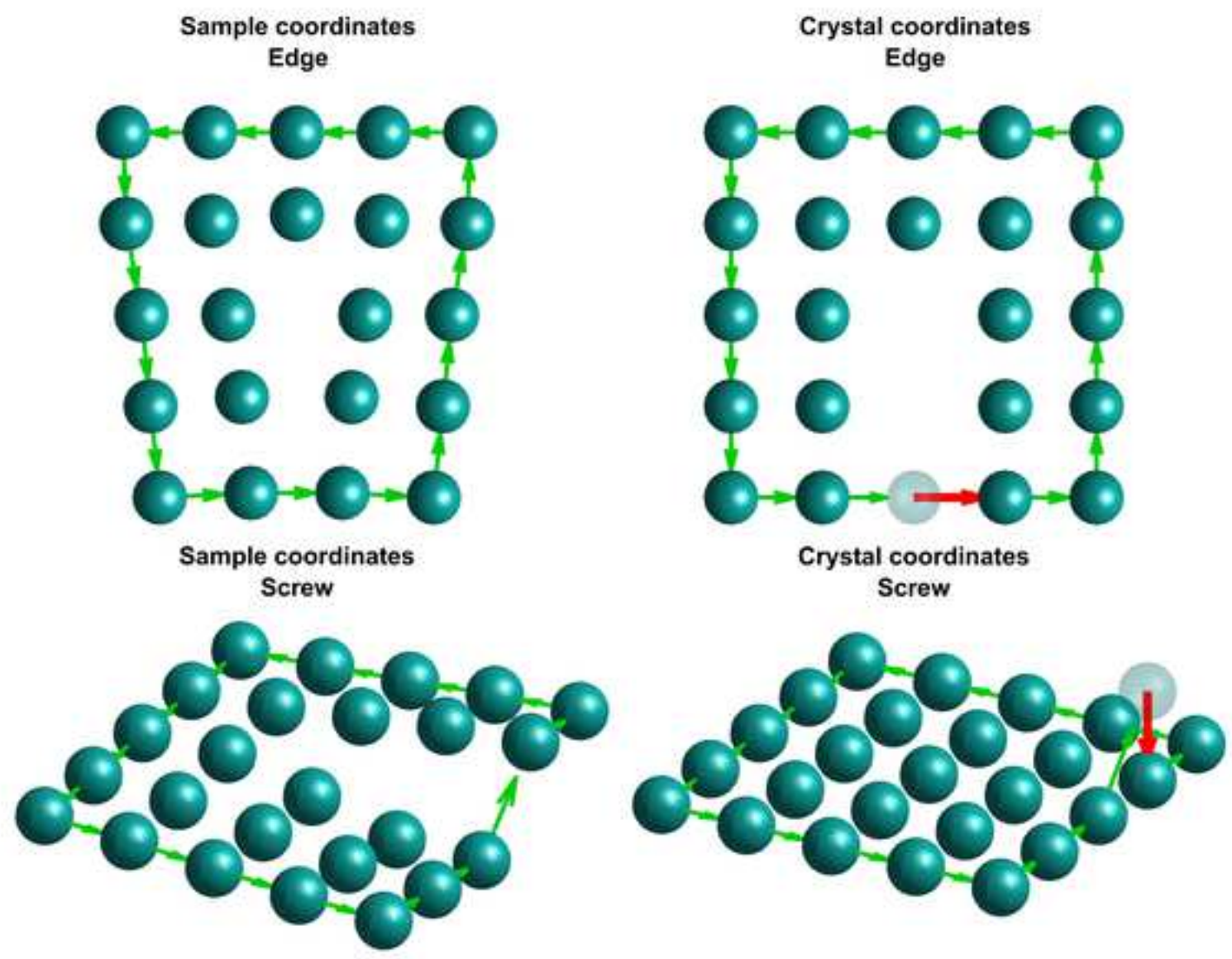
Crystal system	Laue group	Phase	weighted Burgers vector study motivation	Reference	Figure in referenced paper	Integral method used?	Stencil or tile	Sampled area (pixels)	Step size (μm)	W minimum length ($(\mu\text{m})^{-1}$)	α_{95} (deg)	
Cubic holosymmetric	m3m	Periclase	example	(Wheeler et al. 2009)	Fig 11		s	9	10	0.0015	14.9	
Cubic	m3		<i>no studies yet published on minerals</i>	-							-	
Hexagonal holosymmetric	6/mmm	Mg	example	(Wheeler et al. 2009)	Fig 3, 5		s	9	4	0.002	28.1	
		Mg	example	(Wheeler et al. 2009)			s	9	4	0.004	13.9	
		Ti	magnitude display from TKD data	(Trimby et al. 2014)	Fig 5					0.01		n/a
		Ice	search for non-basal dislocations	(Piazolo et al. 2015)				s	9	15	0.0004	37.7
		Ice	search for non-basal dislocations	(Chauve et al. 2017)	Fig. 2			s	9	5	0.0014	32.2
		Ice	intragranular boundary development	(Fan et al. 2022)	Fig. 5		s	9	5	0.006	7.4	
Hexagonal	6/m		<i>no studies yet published on minerals</i>	-							-	
Trigonal holosymmetric	-3m	Quartz	example	(Wheeler et al. 2009)	Fig 15		s	9	2	0.001	110.0	
		Quartz	example	(Wheeler et al. 2009)	Fig 15		s	9	2	0.003	37.7	
		Quartz	compare GND density with density from etch pits	(Billia et al. 2013)	n/a	y						n/a
		Calcite	deduce slip systems hence deformation T	(Mcnamara et al. 2020)	Fig 4, 5							
Trigonal	-3		<i>no studies yet published on minerals</i>	-								
Tetragonal holosymmetric	4/mmm	Zircon	Link magnitude to Pb loss	(MacDonald et al. 2013)	Fig. 9	y				1, 2, 0.8	n/a	
		Zircon	Planar deformation bands	(Kovaleva et al. 2015)	Fig. 6	y					n/a	
		Zircon	help to characterise slip systems	(Kovaleva et al. 2018)	Fig. 6	y					n/a	
Tetragonal	4/m		<i>no studies yet published on minerals</i>	-							-	
Orthorhombic	mmm	Olivine	confirm slip systems dominated by [100]	(Tielke et al. 2019)	Fig. 5 b	y	s	9	3	0.005	14.9	
		Olivine	determine slip systems	(Wieser et al. 2020)	Fig. 4, 7							
		Olivine	tiling example	<i>this contribution</i>	Fig. 7	y	t	100	16	0.00005	26.2	
		Olivine	stencil example	<i>this contribution</i>	Fig. 7		s	9	16	0.001	13.9	
Monoclinic	2/m	Titanite	Diagnose slip systems: map showing WBV direction (6 μm tiles)	(Timms et al. 2019)	Fig. 8c		t	400	0.3	0.001	24.6	
		Titanite	Contoured IPF showing WBV direction (2.4 μm tiles)	(Timms et al. 2019)	Fig. 8e		t	64	0.3	0.003	32.6	
Triclinic	-1	Plagioclase	Diagnose slip system in naturally and experimentally deformed microlites; latter show [001] clearly; both show it in loops	(Kendrick et al. 2017)	Fig. 4		s	9	0.2	0.01	110.0	
		Plagioclase	Understand plagioclase replacement by albite	(Gardner et al. 2021)	Fig. 6		s					
		Plagioclase	tiling example	<i>this contribution</i>	Fig. 8	y	t	400	1	0.0005	14.7	
		Plagioclase	stencil example	<i>this contribution</i>	Fig. 8		s	21	1	0.01	9.5	

References

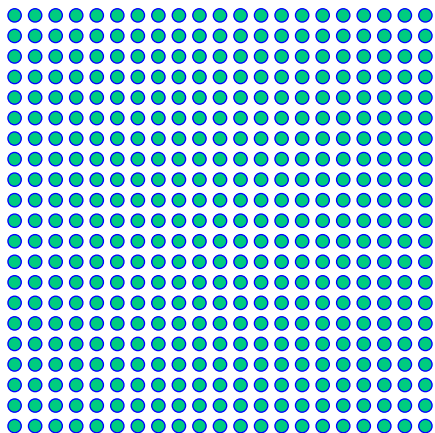
- Ashby, M. F. 1970. Deformation of plastically non-homogeneous materials. *Philosophical Magazine* **21**(170), 399-424.
- Billia, M. A., Timms, N. E., Toy, V. G., Hart, R. D. & Prior, D. J. 2013. Grain boundary dissolution porosity in quartzofeldspathic ultramylonites: Implications for permeability enhancement and weakening of mid-crustal shear zones. *Journal Of Structural Geology* **53**, 2-14.
- Butler, R. F. 1992. *Paleomagnetism: Magnetic Domains to Geologic Terranes*. Blackwell Scientific Publications.
- Chauve, T., Montagnat, M., Piazzolo, S., Journaux, B., Wheeler, J., Barou, F., Mainprice, D. & Tommasi, A. 2017. Non-basal dislocations should be accounted for in simulating ice mass flow. *Earth And Planetary Science Letters* **473**, 247-255.
- Das, S., Hofmann, F. & Tarleton, E. 2018. Consistent determination of geometrically necessary dislocation density from simulations and experiments. *International Journal Of Plasticity* **109**, 18-42.
- De Graef, M. 2020. A dictionary indexing approach for EBSD. *IOP Conference Series: Materials Science and Engineering* **891**, 012009.
- Drury, M. R. & Urai, J. L. 1990. Deformation related recrystallization processes. *Tectonophysics* **172**, 235-253.
- Fan, S., Wheeler, J., Prior, D. J., Negrini, M., Cross, A. J., Hager, T. F., Goldsby, D. L. & Wallis, D. 2022. Using misorientation and weighted Burgers vector statistics to understand intragranular boundary development and grain boundary formation at high temperatures. *Journal of Geophysical Research - Solid Earth* **127**(8), 26 pages.
- Gardner, J., Wallis, D., Hansen, L. N. & Wheeler, J. 2024. Weighted Burgers Vector analysis of orientation fields from high-angular resolution electron backscatter diffraction. *Ultramicroscopy* **257**, 113893.
- Gardner, J., Wheeler, J. & Mariani, E. 2021. Interactions between deformation and dissolution-precipitation reactions in feldspar at greenschist facies. *Lithos* **396-397**.
- Gardner, R. L., Piazzolo, S., Daczko, N. R. & Trimby, P. 2020. Microstructures reveal multistage melt present strain localisation in mid-ocean gabbros. *Lithos* **366**.
- Guillopé, M. & Poirier, J. P. 1979. Dynamic recrystallization during creep of single-crystal halite: an experimental study. *Journal of Geophysical Research* **84**, 5557-5567.
- Hildyard, R. C., Prior, D. J., Faulkner, D. R. & Mariani, E. 2009. Microstructural analysis of anhydrite rocks from the Triassic Evaporites, Umbria-Marche Apennines, Central Italy: An insight into deformation mechanisms and possible slip systems. *Journal Of Structural Geology* **31**(1), 92-103.
- Jiang, J., Britton, T. B. & Wilkinson, A. J. 2013. Measurement of geometrically necessary dislocation density with high resolution electron backscatter diffraction: Effects of detector binning and step size. *Ultramicroscopy* **125**, 1-9.
- Kalácska, S., Dankházi, Z., Zilahi, G., Maeder, X., Michler, J., Ispánovity, P. D. & Groma, I. 2020. Investigation of geometrically necessary dislocation structures in compressed Cu micropillars by 3-dimensional HR-EBSD. *Materials Science and Engineering: A* **770**, 138499.
- Kendrick, J. E., Lavallee, Y., Mariani, E., Dingwell, D. B., Wheeler, J. & Varley, N. R. 2017. Crystal plasticity as a strain marker of the viscous-brittle transition in magmas. *Nature Communications* **8**(1), Art. No. 1926.
- Konijnenberg, P. J., Zaefferer, S. & Raabe, D. 2015. Assessment of geometrically necessary dislocation levels derived by 3D EBSD. *Acta Materialia* **99**, 402-414.
- Kovaleva, E., Klotzli, U., Habler, G. & Wheeler, J. 2015. Planar microstructures in zircon from paleo-seismic zones. *American Mineralogist*.

- Kovaleva, E., Klotzli, U., Wheeler, J. & Habler, G. 2018. Mechanisms of strain accommodation in plastically-deformed zircon under simple shear deformation conditions during amphibolite-facies metamorphism. *Journal Of Structural Geology* **107**, 12-24.
- Kuhr, B. & Farkas, D. 2019. Dislocation content in random high angle grain boundaries. *Modelling and Simulation in Materials Science and Engineering* **27**(4), 045005.
- Lloyd, G. E. 2002. Microstructural evolution in a mylonitic quartz simple shear zone: the significant roles of dauphine twinning and misorientation. In: *Joint International Meeting of the Tectonic-Studies-Group of the Geological-Society London/Structural Geology and Tectonics Division of the Geological-Society-of-America/Geological-Society-of-Australia. Geological Society Special Publication* **224**, London, ENGLAND, 39-61.
- MacDonald, J. M., Wheeler, J., Harley, S. L., Mariani, E., Goodenough, K. M., Crowley, Q. G. & Tatham, D. 2013. Lattice distortion in a zircon population and its effects on trace element mobility and U–Th–Pb isotope systematics: examples from the Lewisian Gneiss Complex, northwest Scotland. *Contributions To Mineralogy And Petrology* **166**, 21-41.
- Mamtani, M. A., Reznik, B. & Kontny, A. 2020. Intracrystalline deformation and nanotectonic processes in magnetite from a naturally deformed rock. *Journal of Structural Geology* **135**, 104045.
- Marquardt, K. & Faul, U. H. 2018. The structure and composition of olivine grain boundaries: 40 years of studies, status and current developments. *Physics and Chemistry of Minerals* **45**(2), 139-172.
- Mcnamara, D. D., Lister, A., Prior, D. J., Scully, A., Gardner, J. & Wheeler, J. 2020. Microanalysis of Calcite Scaling in a Fractured Geothermal System.
- Nicolay, A., Franchet, J. M., Cormier, J., Mansour, H., De Graef, M., Seret, A. & Bozzolo, N. 2019. Discrimination of dynamically and post-dynamically recrystallized grains based on EBSD data: application to Inconel 718. *JOURNAL OF MICROSCOPY* **273**(2), 135-147.
- Nye, J. F. 1953. Some geometrical relations in dislocated crystals. *Acta Metallurgica* **1**, 153-162.
- Pantleon, W. 2008. Resolving the geometrically necessary dislocation content by conventional electron backscattering diffraction. *Scripta Materialia* **58**(11), 994-997.
- Piazolo, S., Montagnat, M., Grennerat, F., Moulinec, H. & Wheeler, J. 2015. Effect of local stress heterogeneities on dislocation fields: Examples from transient creep in polycrystalline ice. *Acta Materialia* **90**, 303-309.
- Poirier, J. P. & Nicolas, A. 1975. Deformation-induced recrystallization due to progressive misorientation of subgrains, with special reference to mantle peridotites. *Journal of Geology* **83**, 707-720.
- Prior, D. J. 1999. Problems in determining the orientations of crystal misorientation axes, for small angular misorientations, using electron backscatter diffraction in the SEM. *Journal of Microscopy* **195**, 217-225.
- Prior, D. J., Mariani, E. & Wheeler, J. 2009. EBSD in the Earth Sciences: applications, common practice and challenges. In: *Electron Backscatter Diffraction in Materials Science* (edited by Schwartz, A. J., Kumar, M., Adams, B. L. & Field, D. P.). Springer, 345-357.
- Ram, F., Zaefferer, S., Japel, T. & Raabe, D. 2015. Error analysis of the crystal orientations and disorientations obtained by the classical electron backscatter diffraction technique. *Journal of Applied Crystallography* **48**(3), 797-813.
- Shigematsu, N., Prior, D. J. & Wheeler, J. 2006. First combined electron backscatter diffraction and transmission electron microscopy study of grain boundary structure of deformed quartzite *Journal of Microscopy* **224**, 306-321.
- Spruzeniece, L., Piazolo, S. & Maynard-Casely, H. E. 2017. Deformation-resembling microstructure created by fluid-mediated dissolution-precipitation reactions. *Nature Communications* **8**.
- Sutton, A. P. & Balluffi, R. W. 1995. *Interfaces in crystalline materials*. Clarendon Press, Oxford.

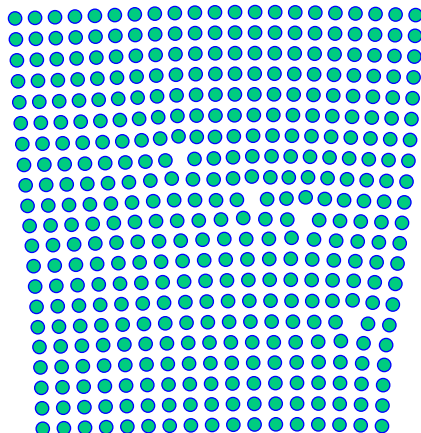
- Tielke, J. A., Mecklenburgh, J., Mariani, E. & Wheeler, J. 2019. The influence of water on the strength of olivine dislocation slip systems. *Journal Of Geophysical Research: Solid Earth* **124**, 6542-6559.
- Tielke, J. A., Zimmerman, M. E. & Kohlstedt, D. L. 2017. Hydrolytic weakening in olivine single crystals. *Journal of Geophysical Research-Solid Earth* **122**(5), 3465-3479.
- Timms, N. E., Pearce, M. A., Erickson, T. M., Cavosie, A. J., Rae, A., Wheeler, J., Wittman, A., Ferriere, F., Poelchau, M. H., Tomioka, N., Collins, G. S., Gulick, S. P. S., Rasmussen, C., Morgan, J. V. & Scientists, I.-I. E. 2019. New shock microstructures in titanite (CaTiSiO₅) from the peak ring of the Chicxulub impact structure, Mexico. *Contributions To Mineralogy And Petrology*.
- Timms, N. E., Reddy, S. M., Healy, D., Nemchin, A. A., Grange, M. L., Pidgeon, R. T. & Hart, R. 2012. Resolution of impact-related microstructures in lunar zircon: A shock-deformation mechanism map. *Meteoritics & Planetary Science* **47**(1), 120-141.
- Trimby, P. W., Cao, Y., Chen, Z., Han, S., Hemker, K. J., Lian, J., Liao, X., Rottmann, P., Samudrala, S., Sun, J., Wang, J. T., Wheeler, J. & Cairney, J. M. 2014. Characterizing deformed ultrafine-grained and nanocrystalline materials using transmission Kikuchi diffraction in a scanning electron microscope. *Acta Materialia* **62**, 69-80.
- Trimby, P. W., Prior, D. J. & Wheeler, J. 1998. Grain boundary hierarchy development in a quartz mylonite. *Journal of Structural Geology* **20**, 917-935.
- Wallis, D., Hansen, L. N., Ben Britton, T. & Wilkinson, A. J. 2016. Geometrically necessary dislocation densities in olivine obtained using high-angular resolution electron backscatter diffraction. *Ultramicroscopy* **168**, 34-45.
- Wallis, D., Hansen, L. N., Britton, T. B. & Wilkinson, A. J. 2019a. High-Angular Resolution Electron Backscatter Diffraction as a New Tool for Mapping Lattice Distortion in Geological Minerals. *Journal of Geophysical Research: Solid Earth* **124**, 6337-6358.
- Wallis, D., Parsons, A. J. & Hansen, L. N. 2019b. Quantifying geometrically necessary dislocations in quartz using HR-EBSD: Application to chessboard subgrain boundaries. *Journal of Structural Geology* **125**, 235-247.
- Weikusat, I., Miyamoto, A., Faria, S. H., Kipfstuhl, S., Azuma, N. & Hondoh, T. 2011. Subgrain boundaries in Antarctic ice quantified by X-ray Laue diffraction. *Journal of Glaciology* **57**(201), 111-120.
- Wheeler, J., Mariani, E., Piazzolo, S., Prior, D. J., Trimby, P. & Drury, M. R. 2009. The weighted Burgers vector: a new quantity for constraining dislocation densities and types using Electron Backscatter Diffraction on 2D sections through crystalline materials. *Journal of Microscopy* **233**(3), 482-494.
- White, S. 1976. The effects of strain on the microstructures, fabrics, and deformation mechanisms in quartzites. *Philosophical Transactions of the Royal Society of London A* **283**, 69-86.
- Wieser, P., Edmonds, M., Maclennan, J. & Wheeler, J. 2020. The Record of Magma Storage under Kilauea Volcano preserved in Distorted Olivine Crystals. *Nature Communications*.
- Wilkinson, A. J. & Randman, D. 2010. Determination of elastic strain fields and geometrically necessary dislocation distributions near nanoindenters using electron back scatter diffraction. *Philosophical Magazine* **90**(9), 1159-1177.
- Winkelmann, A., Nolze, G., Cios, G., Tokarski, T. & Bała, P. 2020. Refined Calibration Model for Improving the Orientation Precision of Electron Backscatter Diffraction Maps. *Materials* **13**(12), 2816.
- Wirth, R. 1996. Thin amorphous films (1–2 nm) at olivine grain boundaries in mantle xenoliths from San Carlos, Arizona. *Contributions to Mineralogy and Petrology* **124**(1), 44-54.
- Zhang, Z., Ódor, É., Farkas, D., Jóni, B., Ribárik, G., Tichy, G., Nandam, S.-H., Ivanisenko, J., Preuss, M. & Ungár, T. 2020. Dislocations in Grain Boundary Regions: The Origin of Heterogeneous Microstrains in Nanocrystalline Materials. *Metallurgical and Materials Transactions A* **51**(1), 513-530.



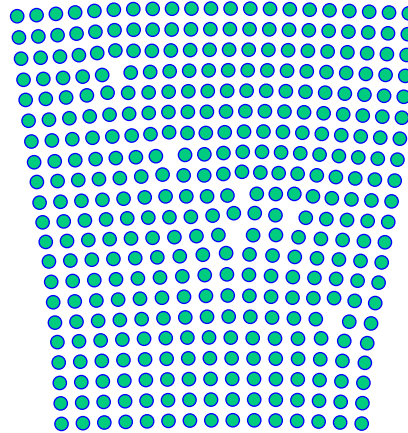
0 dislocations



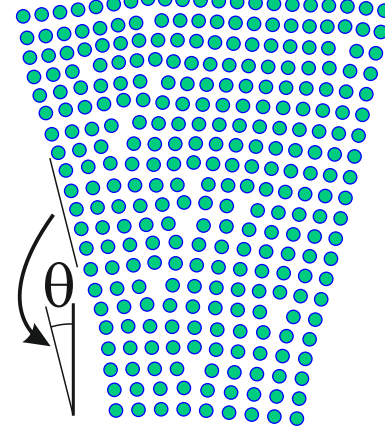
4 dislocations



6 dislocations

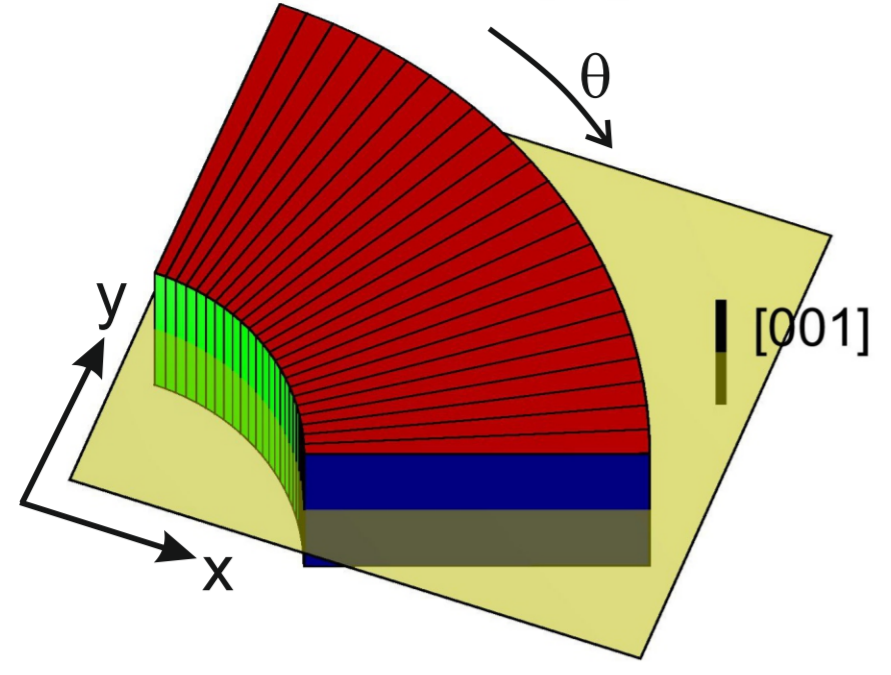


12 dislocations



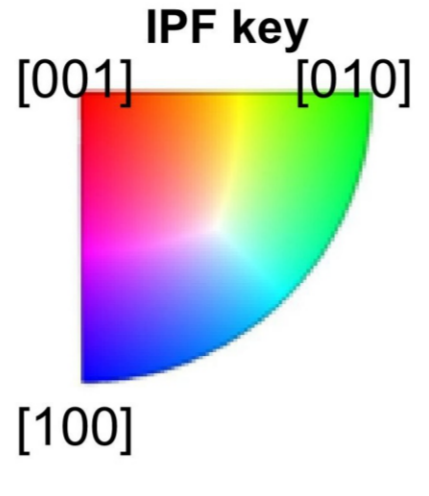
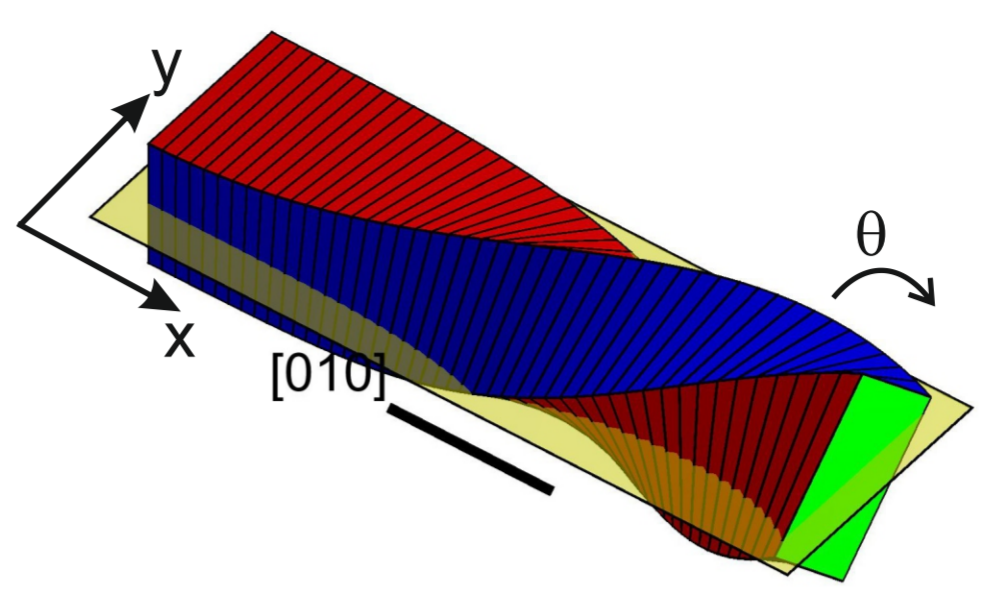
Smoothly Tilted Crystal

b) 3D view (tilt)

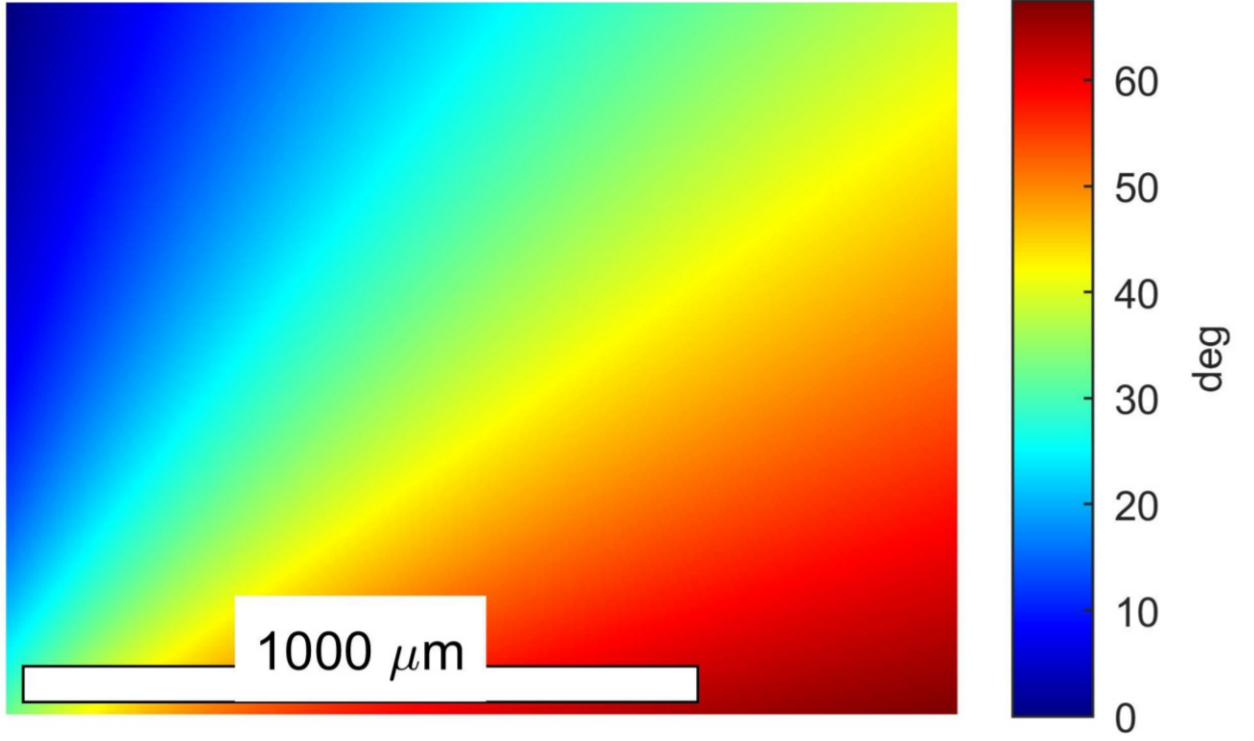


Smoothly Twisted Crystal

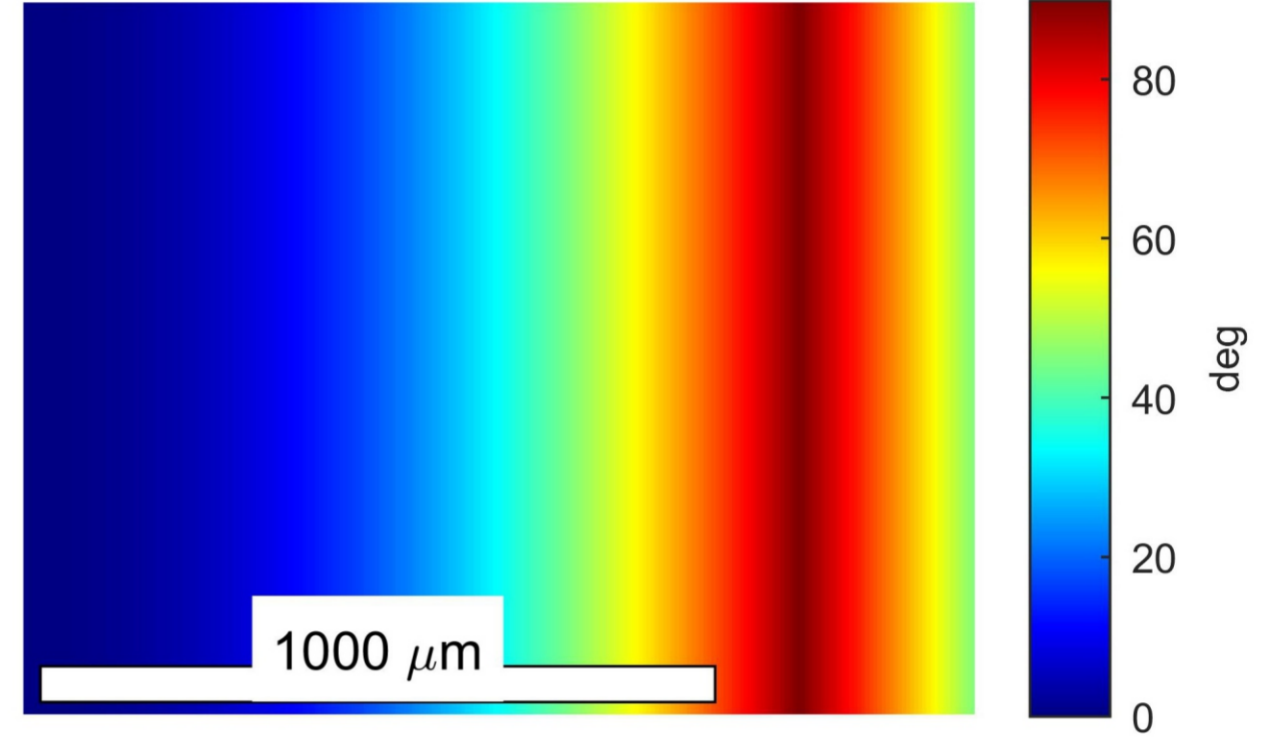
b) 3D view (twist)



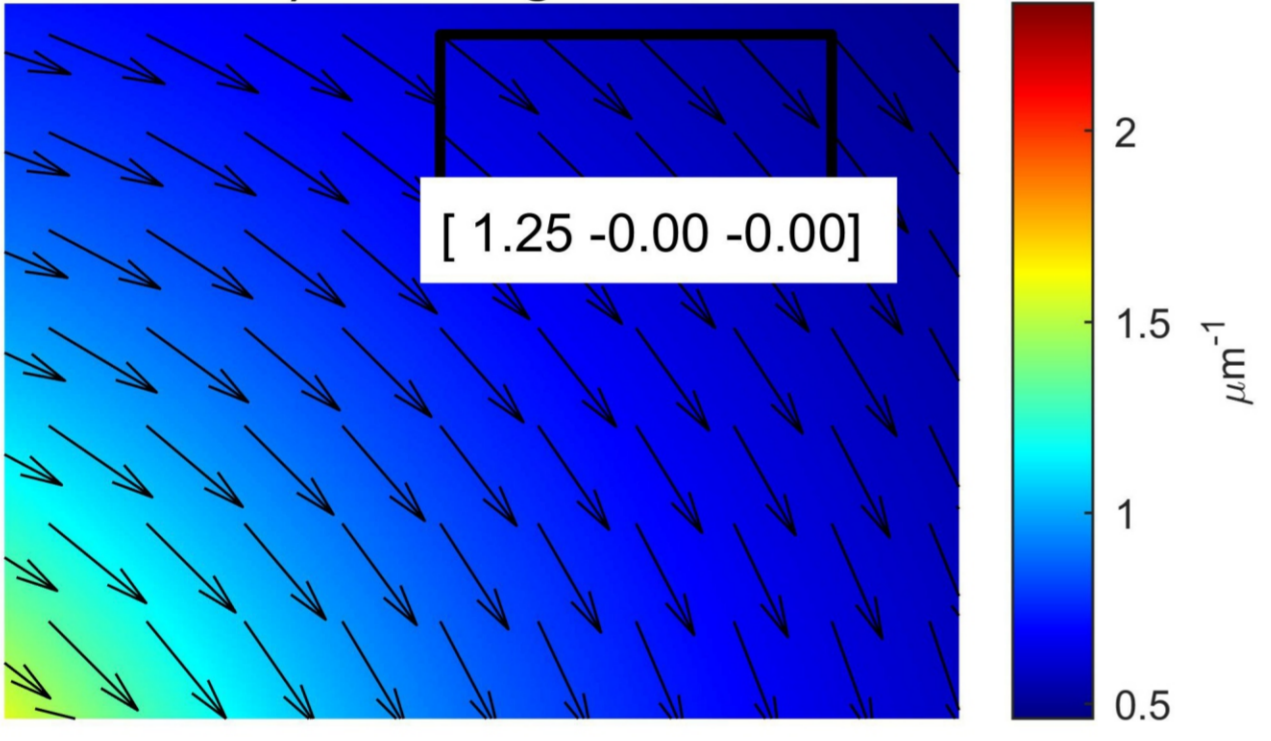
c) Misorientation



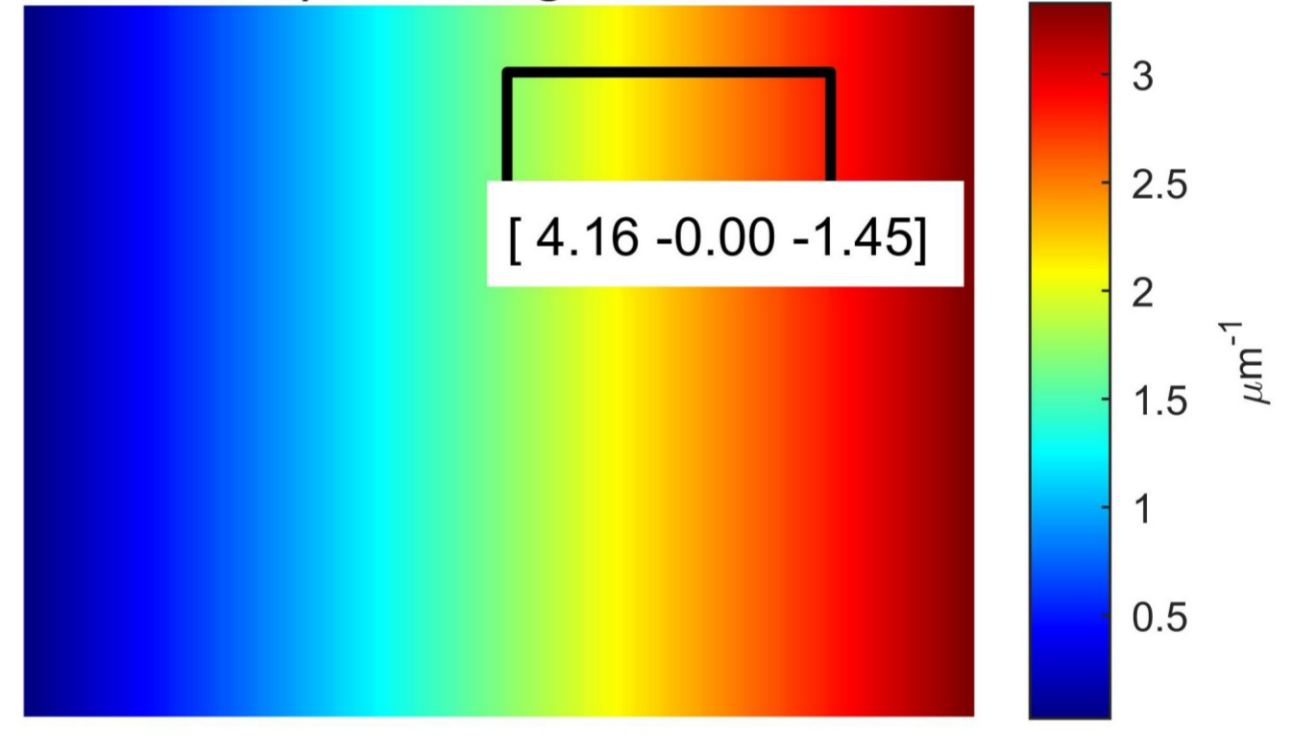
d) Misorientation



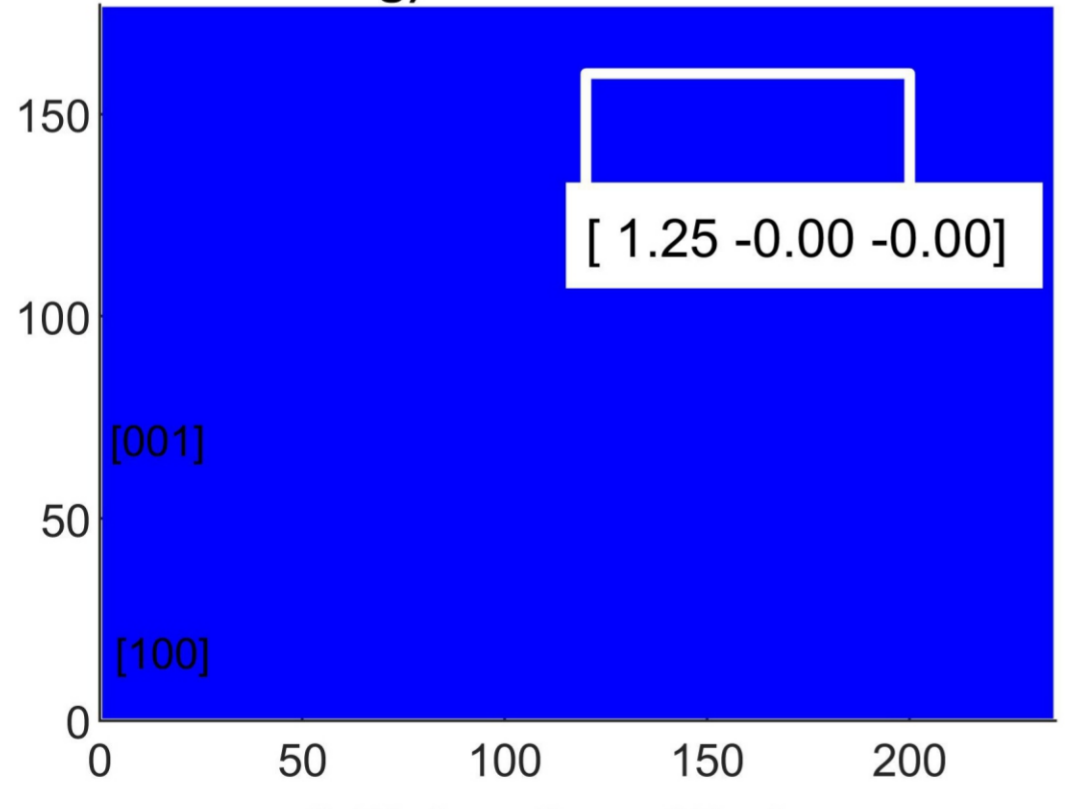
e) WBV magnitude



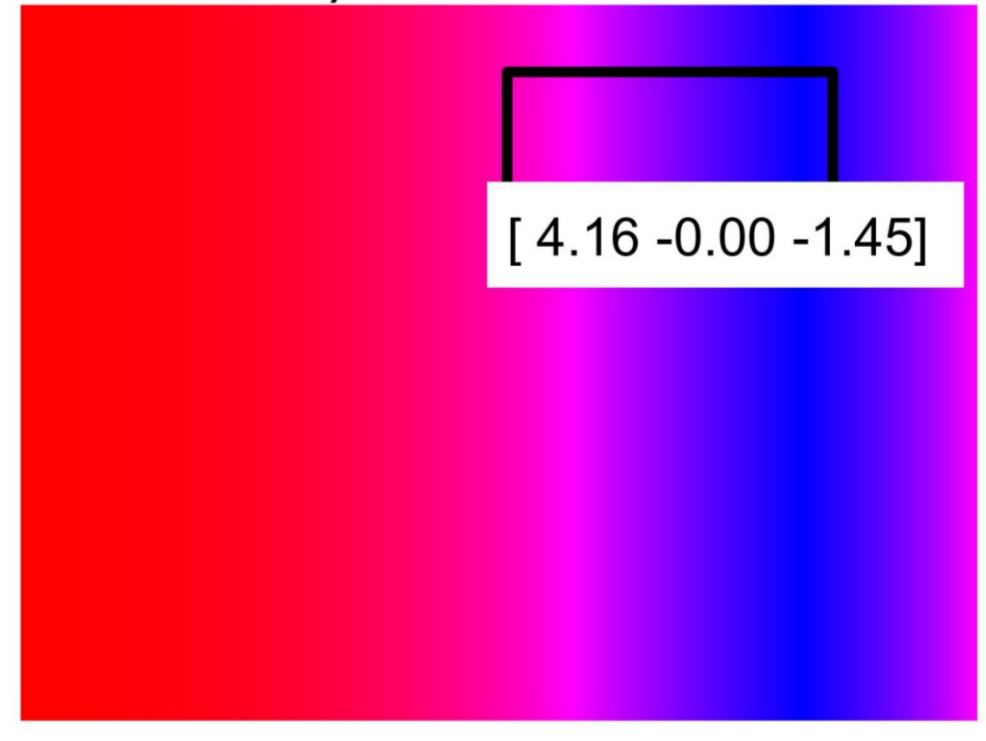
f) WBV magnitude



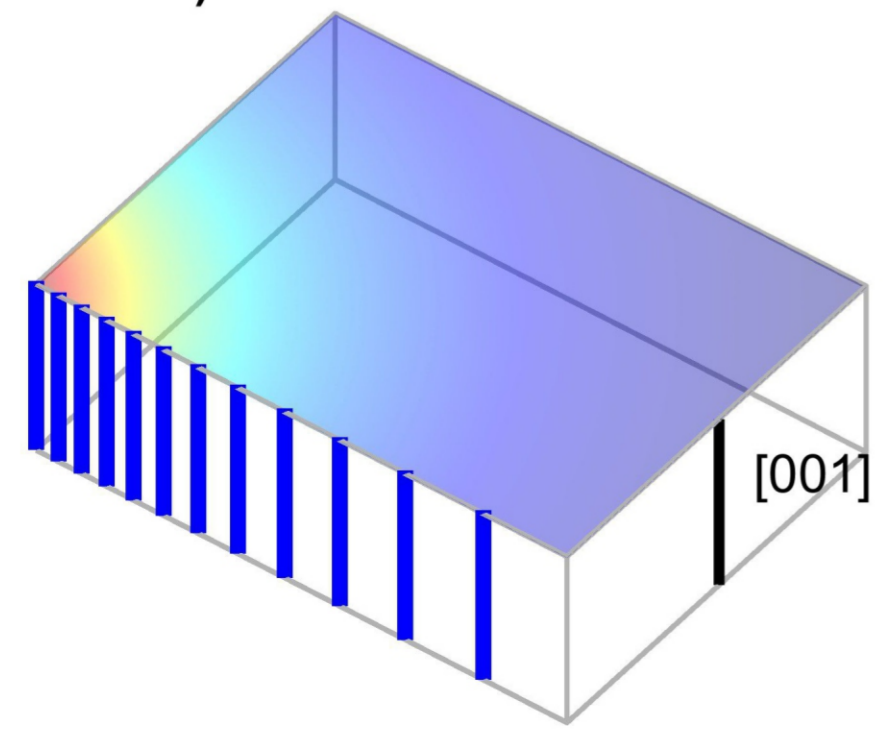
g) WBV direction



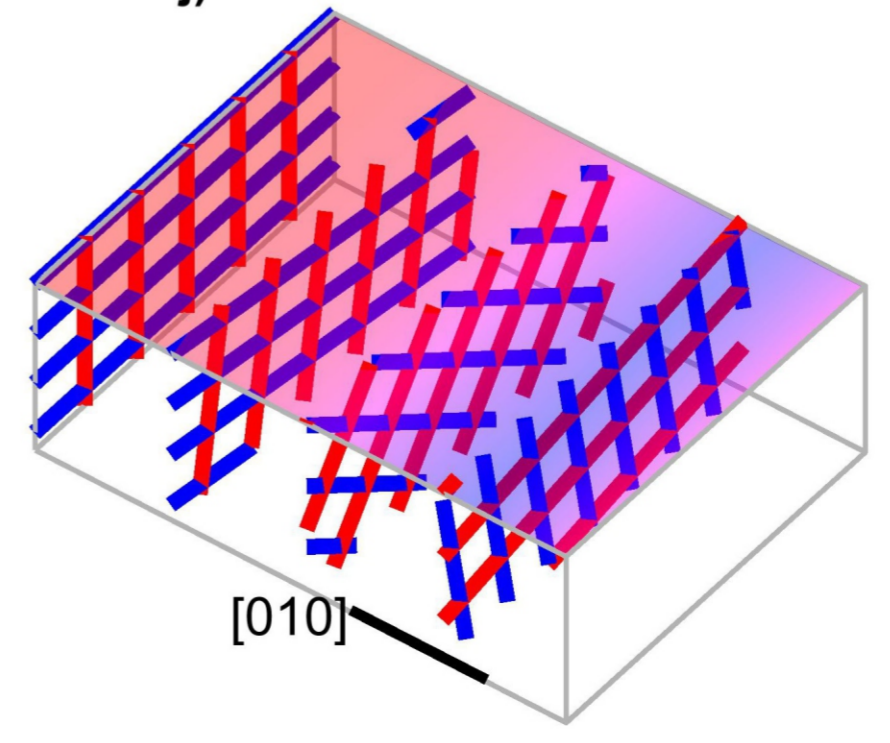
h) WBV direction

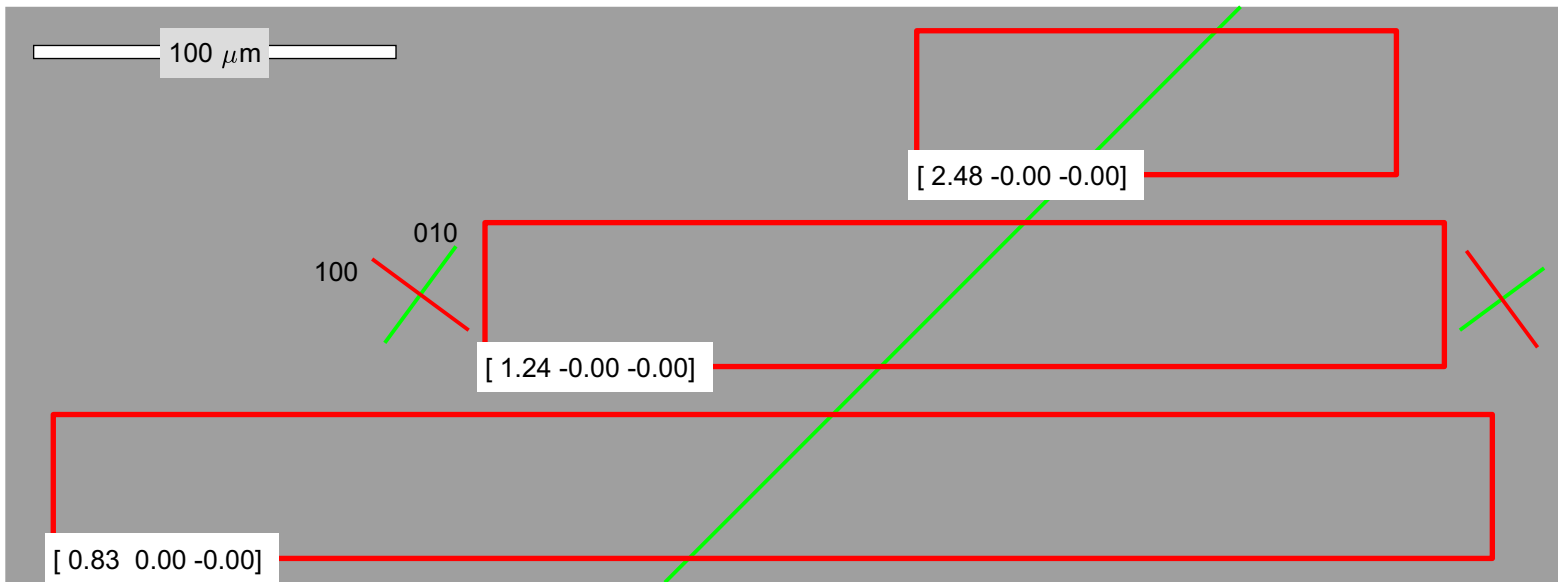


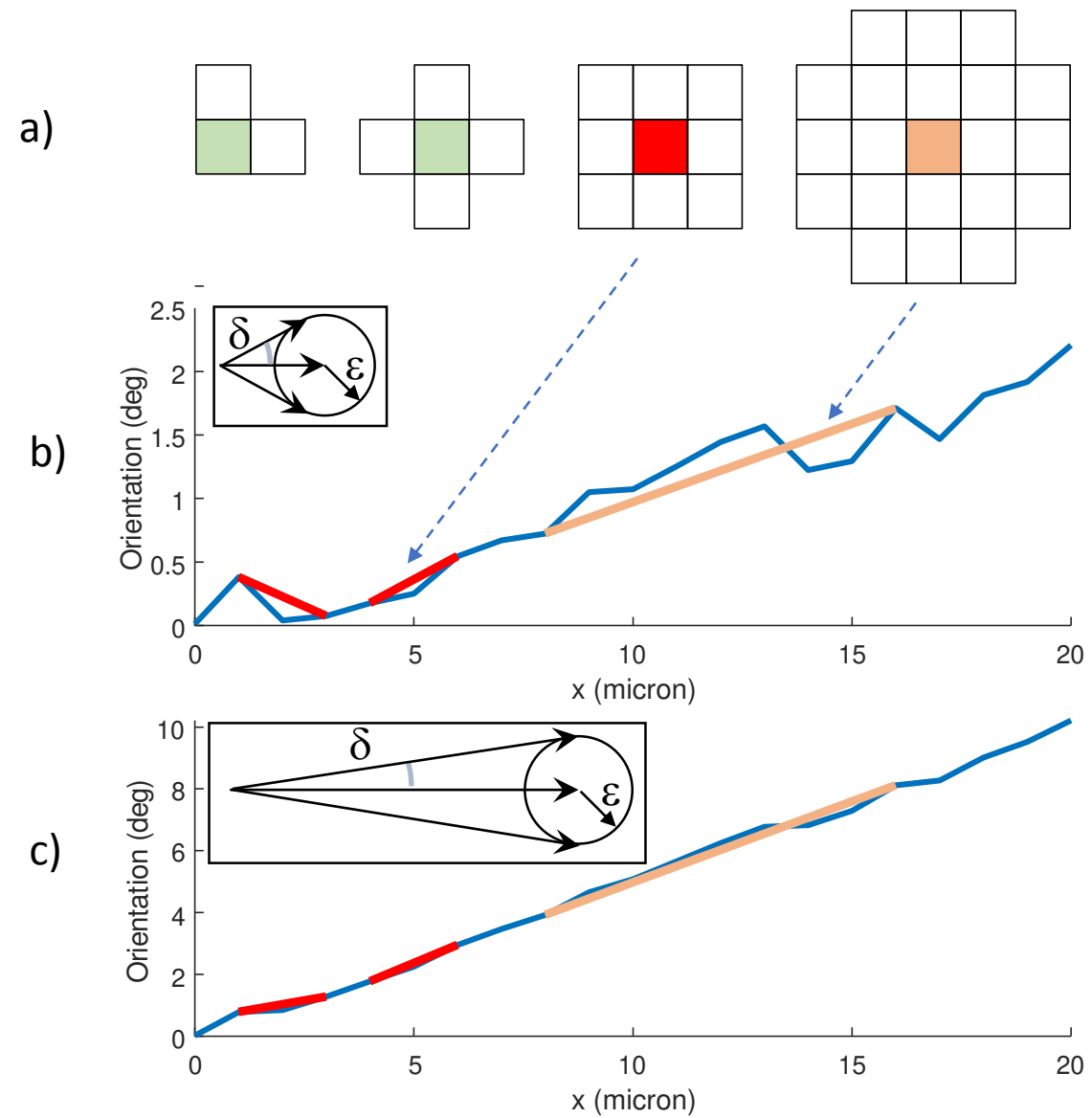
i) Dislocations 3D view

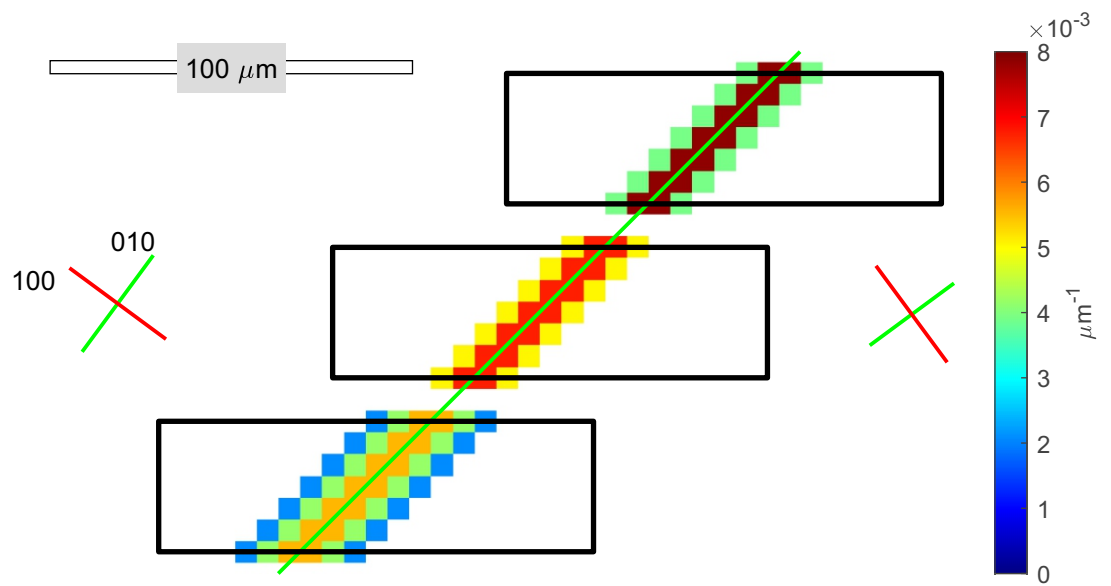


j) Dislocations 3D view









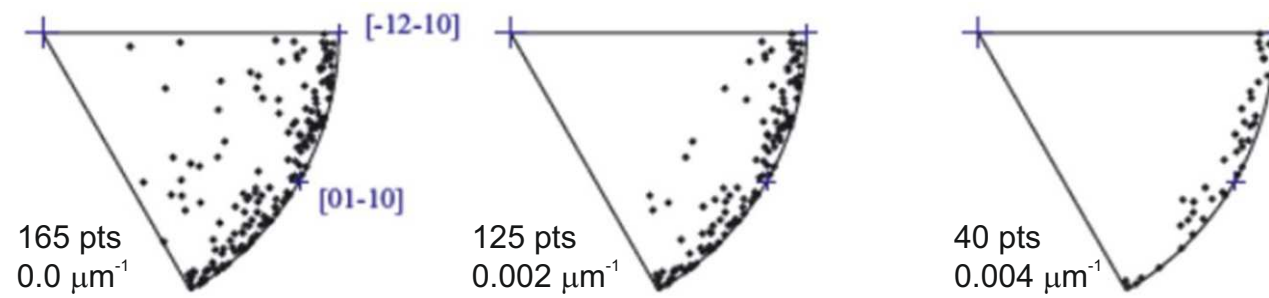
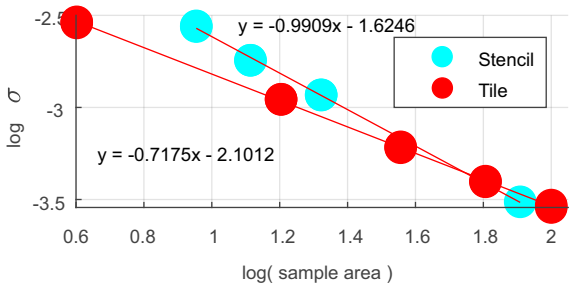
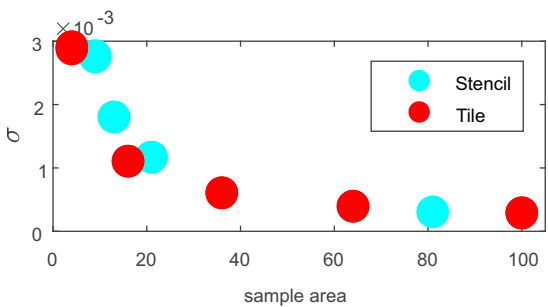
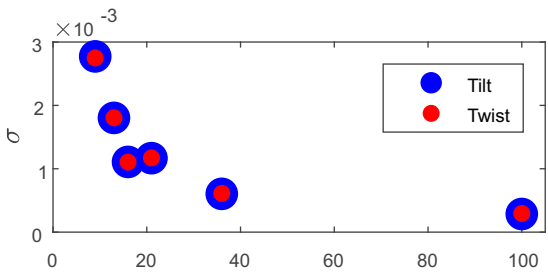
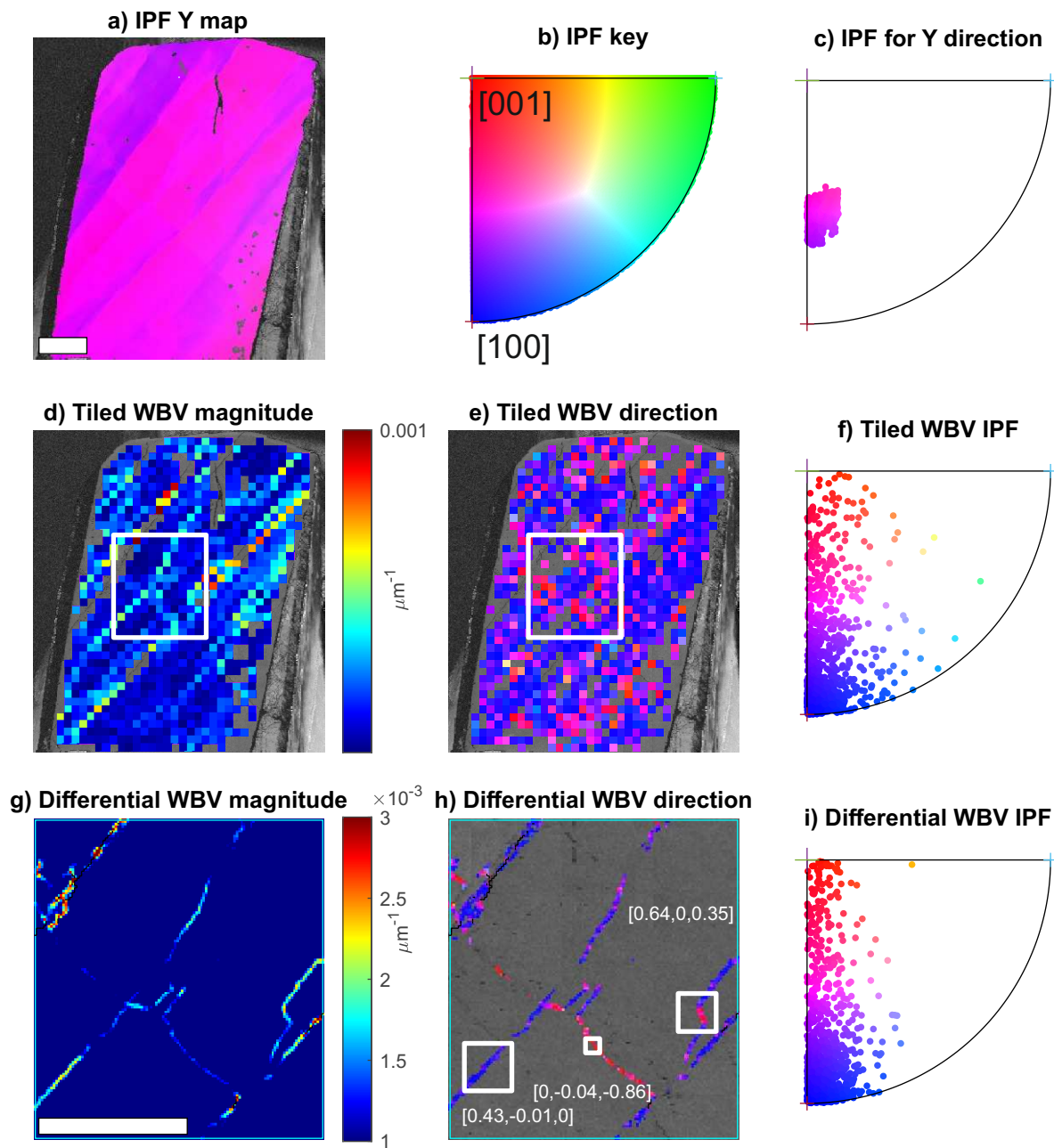


Figure 8

[Click here to access/download;Figure;Fi](#)





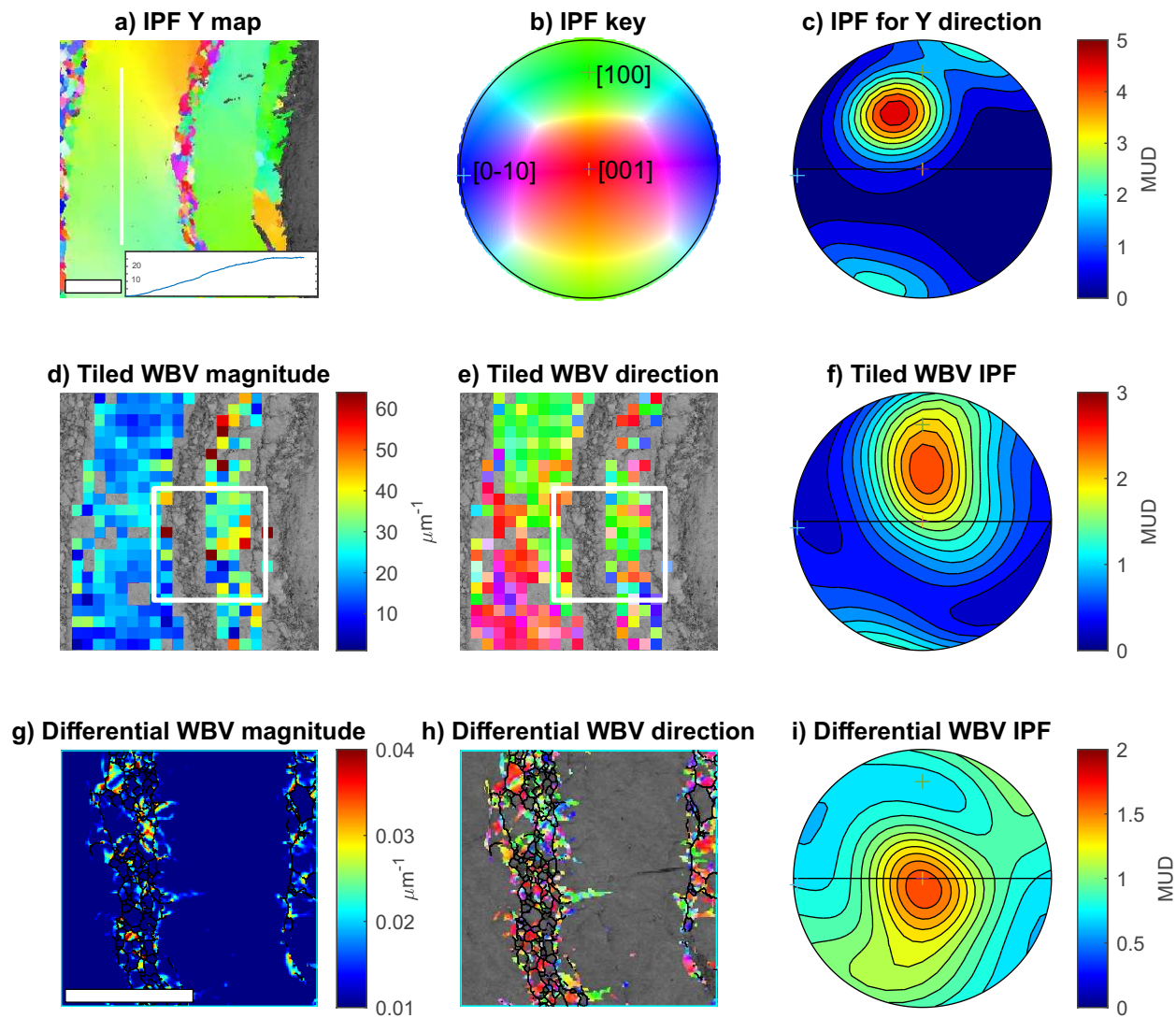
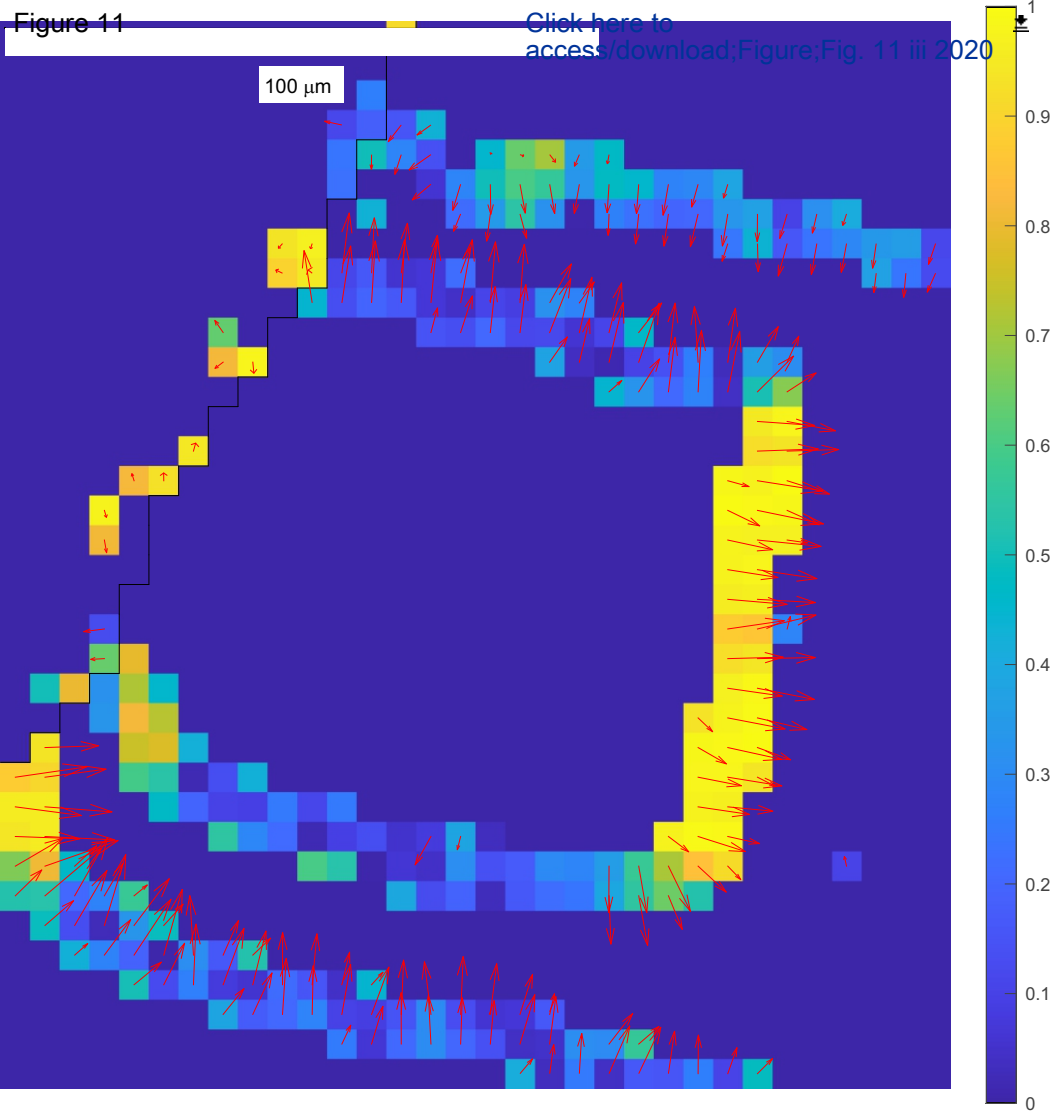
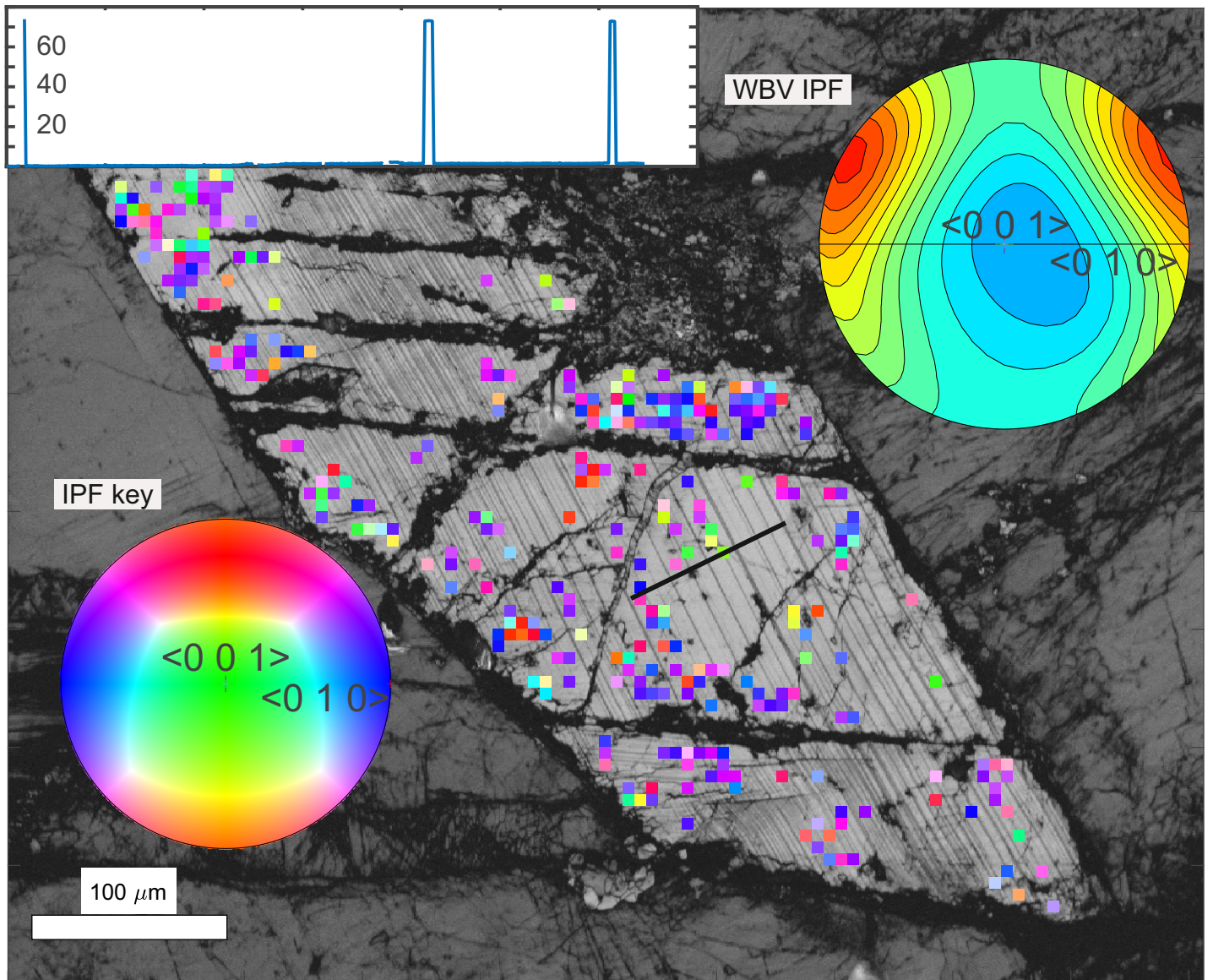


Figure 11

[Click here to access/download;Figure;Fig. 11 iii 2020](#)





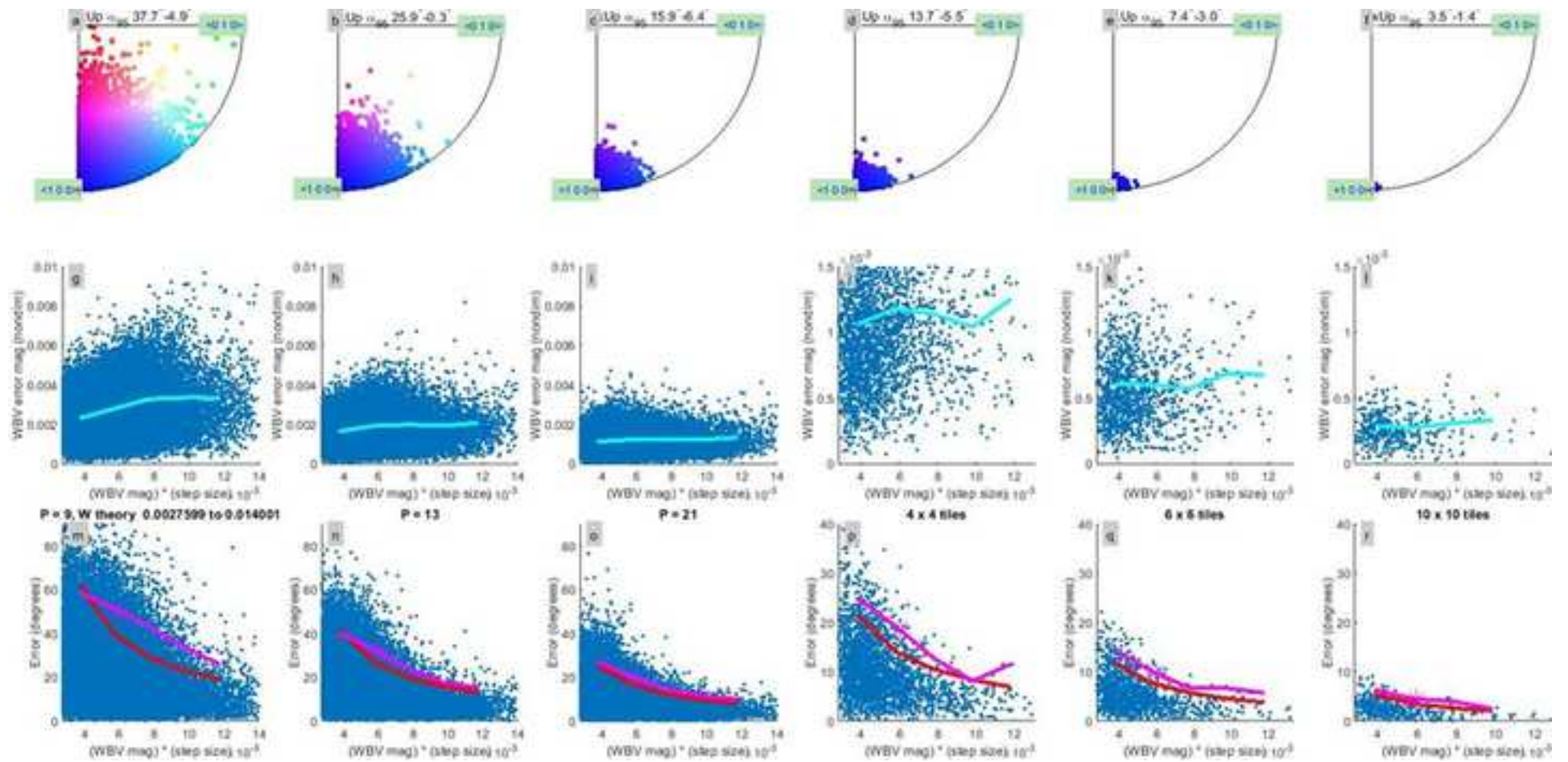
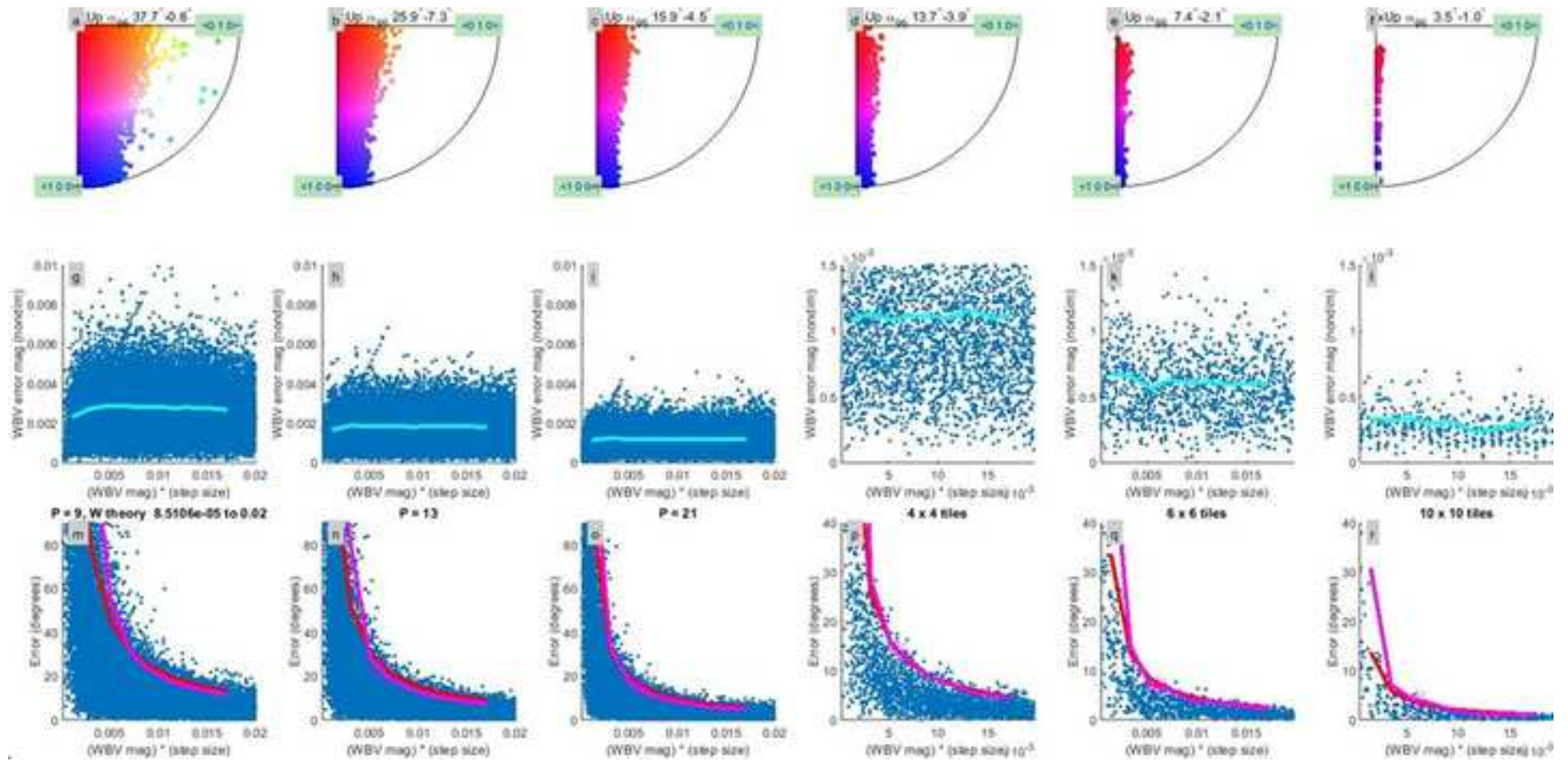


Figure S2

[Click here for access/download;Figure;Fig. S2.jpg](#)



[Click here to access/download](#)

Supplementary Material

[WBV and geology supp for JSG revised.docx](#)

